High Density Periodic Metal Nanopyramids for Surface Enhanced Raman Spectroscopy

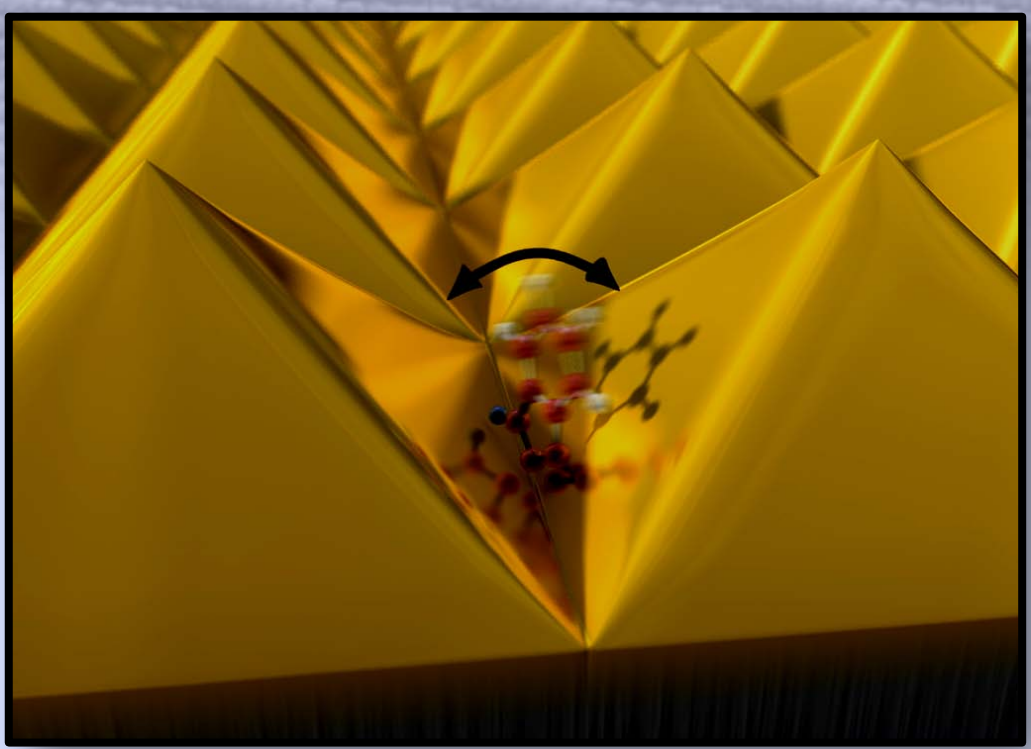

Mingliang Jin

MESA+
INSTITUTE FOR NANOTECHNOLOGY

UNIVERSITY OF TWENTE.

High Density Periodic Metal Nanopyramids for Surface Enhanced Raman Spectroscopy

Mingliang Jin

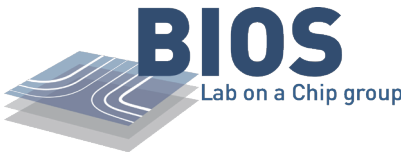

The research described within this thesis was carried in the BIOS/Lab-on-a-Chip group at the MESA+ Institute for Nanotechnology at the University of Twente, Enschede, the Netherlands. The MEMSLand project financially supported this research.

Committee members:

Chairman	
Prof. Dr. Ir. A.J. Mouthaan	University of Twente
Promoter	
Prof. Dr. Ir. A. van den Berg	University of Twente
Assistant promoter	
Dr. Edwin T. Carlen	University of Twente
Members	
Prof. Dr. M. Moskovits	The City College of New York
Prof. Dr. J. L. Herek	University of Twente
Prof. Dr. Ir. A. J. H. M. Rijnders	University of Twente
Dr. Ir. N.R. Tas	University of Twente
Dr. Cees Otto	University of Twente

Title: High Density Periodic Metal Nanopyramids for Surface Enhanced Raman Spectroscopy

Author: Mingliang Jin

ISBN: 978-90-365-3322-5

Publisher: Wohrmann Print Service, Zutphen, the Netherlands

Cover images: Three dimensional gold nanopyramid surfaces (*Front cover:* artists rendering from Nymus3D; *Back cover and background:* scanning electron microscopy images of fabricated gold surfaces) with measured Raman spectra of chemisorbed mercaptobenzene.

HIGH DENSITY PERIODIC METAL NANOPYRAMIDS FOR SURFACE ENHANCED RAMAN SPECTROSCOPY

DISSERTATION

to obtain
the degree of doctor at the University of Twente
on the authority of the rector magnificus,
prof. dr. H. Brinksma,
on account of the decision of the graduation committee,
to be publicly defended
on Thursday the 19th of January 2012 at 14:45 hrs

by

Mingliang Jin

Born on the 19th of May 1977

in Shandong, China

This dissertation is approved by:

the promoter: Prof. Dr. Ir. Albert van den Berg

the assistant promoter: Dr. Edwin T. Carlen

To My Family

Contents

Chapter 1

Introduction

1.1 Project goal

The work presented in this thesis is focused on two areas. First, a new type of nanotextured noble-metal surface has been developed. The new nanotextured surface is demonstrated to enhance inelastic (Raman) scattering, called surface enhanced Raman scattering (SERS), from molecules adsorbed on the metal surface due to large electromagnetic fields generated in nanoscale gaps by an external laser excitation source. By detecting the enhanced Raman scattered photons, the molecular bond information can be analyzed using methods from conventional Raman spectroscopy. Raman spectroscopy is very powerful analytical method in chemistry, biology and other scientific areas, since it provides molecular vibrational information, which is considered a fingerprint for a particular molecule.

Raman spectroscopy is less commonly used compared to other analytical methods, such as infrared spectroscopy, due to its extremely weak signal. For example, a typical molecule excited with ~1 mW laser excitation will scatter ~10^{-6} photons s^{-1} $molecule^{-1}$ [1], which requires a large number of molecules and long integration times. Over the past few decades, there has been a dramatic increase in

[1] The photon flux [photons s^{-1}] can be approximated as $\phi \approx 5\times10^{15} n_d \lambda P \sigma$, where n_d is the refractive index of the surrounding medium, λ_o [nm] is the excitation laser wavelength, P [W cm^{-2}] is the irradiance in the spot size area A_s [cm^2], and σ [cm^2] is scattering cross-section of the molecule. For n_d=1, λ=600 nm, P=1.3×10^4 W cm^{-2} (1 μm diameter spot size), and σ=10^{-29} cm^2 results in $\phi \approx 10^{-6}$ photons s^{-1} $molecule^{-1}$.

the use of Raman spectroscopy in part due to SERS since it can provide huge Raman scattered intensity enhancements. A *good* SERS substrate should provide large and spatially uniform average Raman signal enhancements (greater than 10^6) over large areas (greater than mm^2) in order to be useful as an analytical measurement technique. Four important aspects should be considered when developing a new SERS substrate: *i*. The first and most important is that the nanoscale gaps should be made from a noble metal (e.g. *Ag* and *Au*), which enables the use of laser sources in the visible spectrum, with gap distances less than 5 nm; *ii*. the substrate should contain a high density of nanogaps with homogeneous nanogap dimensions over large surface areas; *iii*. the geometric alignment of the nanogaps to the excitation laser polarization should be well-controlled in order to maximize the generation of the local surface plasmon; and *iv*. The nanogap should be easily accessible for molecular diffusion into the nanogap region.

Based on the description above we have developed a general technique to manufacture high density nanopyramid (NPy) and nanogroove (NG) array templates from (100) silicon. Small pitch NPy arrays form spontaneously using anisotropic wet etching silicon following lithographic patterning of an etching mask. Sharp v-shaped nanogaps are formed between two adjacent pyramids and are used to couple laser excitation into a local surface plasmon. The size and density of these nanogaps are limited by the minimum dimensional capability of the nanolithography procedure and the silicon etching time, which is self-limiting. The silicon surfaces are then coated with a thin polycrystalline *Au* layer. We have studied the behavior of the *Au* NPy surfaces using a combination of the numerical modeling, high-resolution surface imaging (scanning electron, atomic force, and transmission electron microscopy), reflection spectroscopy, and Raman spectroscopy. Reflection spectroscopy provides information about the coupling of the optical laser excitation into a local surface plasmon resonance, which includes

the resonant coupling energy, inter-band transition effects, dielectric interface dependent resonant coupling energy, and polarization alignment effects. Raman spectroscopy allows us to probe the enhancement properties of the *Au* NPy surface and extensive studies of the enhancement behavior of the NPy surfaces using surface adsorbed rhodamine-6G ($C_{28}H_{31}N_2O_3$), pyridine (C_5H_5N), pyrazine ($C_4H_4N_2$) in water and monolayers of chemisorbed benzene-thiol (C_6H_5SH) have been performed.

1.2 Thesis outline

In chapter 2, an introduction to Raman spectroscopy and surface enhanced Raman scattering is given as well as a brief comparison to infrared spectroscopy. The differences between the spectroscopic methods are described and advantages and disadvantages are highlighted. The local electromagnetic field generated by the local surface plasmon resonance at the surface of the metal nanostructure, and between closely spaced nanostructures, is commonly accepted to be the dominant enhancement mechanism of inelastically scattered photons from molecules adsorbed to the metal surface. Finally, a figure of merit is described, which highlights the important characteristics of a *good* SERS substrate.

Chapter 3 describes the basic foundations of plasmonics theory and its relationship to SERS through a localized electromagnetic field enhancement. Surface plasmon polaritons and local surface plasmons on flat metal surfaces are introduced and compared to local surface plasmons on curved surfaces, such as metal nanospheres. The frequency dependent properties of the dielectric function of *Au* are described and the ideal Drude model is compared to empirical models that include inter-band transition effects, which are important for plasmonics. The metal NPy surfaces are introduced and compared to surfaces analyzed by other research groups. A two-dimensional numerical model of the v-shaped nanogap has

been developed using cross-section profiles measured from real surfaces using high-resolution atomic force microscopy. The two-dimensional model was simulated with a commercial finite difference time domain software package and simulation results of an *Au* nanogap with the appropriate dielectric function are presented in terms on an electromagnetic field enhancement at the excitation laser wavelength used for Raman spectroscopy measurements.

In Chapter 4, the new SERS substrate fabrication technology is presented, which has been developed to realize new nanotextured surfaces with periodically self-aligned nanopyramid (NPy) and nanogroove (NG) structures with precisely defined pitch λ_g that are closely packed with 2 nm separation gaps over large areas. The simple self-aligned fabrication technique requires only a single lithography step and wet anisotropic silicon etching. Electron-beam lithography was first used to demonstrate the realization of tunable NPy surfaces with pitches in the range $150 \leq \lambda_g \leq 500$ nm. The NPy and NG surfaces are coated with a thin *Au* layer, which results in strong localized surface plasmon resonance with visible frequency excitation. The fabrication method was further improved by using laser interference lithography to uniformly pattern the two-dimensional NPy arrays over large areas (an entire 100 mm diameter silicon wafer). The NPy and NG surfaces have been characterized by high-resolution scanning electron microscopy and high-resolution atomic force microscopy. The v-shaped nanogap between two adjacent nanoscale features is characterized with high-resolution atomic force microscopy and high-resolution transmission electron microscopy.

Reflection spectroscopy is used in Chapter 5 to investigate the generation of local surface plasmon resonance in the v-shaped nanogaps between adjacent *Au* NPy and *Au* NG surfaces. Plasmonic coupling of a p-polarized white light source normally incident on the surface is investigated as a function of surface pitch ($150 \text{ nm} \leq \lambda_g \leq 500$ nm), alignment of polarization with surface structures ($0° \leq \theta \leq 180°$),

and different dielectric materials consisting of air, deionized water and calibrated refractive index liquids ($1.3000 \leq n_d \leq 1.7200$). Angle resolved reflectivity measurements were conducted on the *Au* NPy surfaces (λ_g=200 nm) coated with a thin polymer layer ($n_d \approx 1.5$) as a function of incidence angle and excitation wavelength using spectroscopic ellipsometry.

Chapter 6 describes the use of Raman spectroscopy to assess the performance of the *Au* NPy and *Au* NG surfaces developed in this thesis well known probe molecules to assess the magnitude and spatial uniformity of the non-resonant enhancement factor. First, we analyzed rhodamine-6G in aqueous solution and assessed the enhancement capability of the *Au* NPy substrates by successively reducing the solution concentration and estimating the number of molecules in single point measurements. The magnitude and spatial uniformity of the enhancement factor of the SERS substrate has been assessed using monolayers of benzene-thiol chemisorbed directly on the *Au* NPy surfaces. The enhancement factor distribution, and associated mean and standard deviation, are assessed over large surface areas using over 10,000 measured spectra.

Chapter 7 presents the most recent results of single molecule detection of non-resonant molecules on the *Au* NPy surfaces using the bi-analyte method, which is a statistical method that is used to justify single molecule SERS measurements. The difference between resonant and non-resonant single molecule measurements is presented and the importance of reducing the limit of detection of non-resonant molecules. The bi-analyte method is reviewed and compared to conventional single molecule SERS studies based on ultra-low sample concentrations of single types of molecules. Measurement results and data analysis procedures of Raman spectra of surface adsorbed pyridine and pyrazine mixtures at varying concentrations in aqueous solution are presented. Chapter 8 contains a summary of the research presented in this thesis along with future recommendations.

Chapter 2

Surface enhanced Raman scattering/spectroscopy

The basic principles of Raman spectroscopy are described and compared to infrared spectroscopy; a more commonly used spectroscopic method for chemical analysis. The remainder of the chapter is devoted to surface enhanced Raman scattering/spectroscopy (SERS), which includes a description of the electromagnetic and chemical enhancement effects as well as its application to Raman spectroscopy.

2.1 Raman spectroscopy

2.1.1 Introduction

Almost a century ago, Sir Chandrasekhara Venkata Raman and his student Kariamanickam Srinivasa Krishnan discovered Raman scattering in liquid using sunlight as a light source[1]. When monochromatic light of energy $h\nu_o$, where h is Planck's constant [6.63×10^{-34} J s^{-1}] and ν_o [s^{-1}] is the frequency of the light wave, interacts with matter, there is a small probability that it will be scattered. Scattering processes involve the instantaneous absorption of an incident photon and subsequent emission of another photon, or scattered photon. When the emitted photon is elastically scattered at the same frequency as the excitation source, called Rayleigh scattering, the incident photon and scattered photon have the same energy (frequency), as is shown schematically in the simplified Jablonski diagram in Figure 2.1. Rayleigh scattering gives us the blue color of the sky and the opalescence of large masses of ice. Molecular vibrations also perturb the electron cloud of the molecule, and there is a small finite probability that the optical and vibrational oscillations will interact, which results in inelastic scattering, or Raman scattering.

The Raman scattering transitions are shown in Figure 2.1. The inelastically scattered photons that are lower in energy by an amount equal to a vibrational transition $h(\nu_o-\nu_l)$ are called Stokes scattered photons. Inelastically scattered photons higher in energy by an amount equal to vibrational transition $h(\nu_o+\nu_l)$ are called anti-Stokes scattered. The virtual energy states shown in Figure 2.1 are not true quantum states of the molecule but can be considered as temporal distortions of the electron cloud of the molecule caused by the oscillating electric field of the excitation source. Every scattering process corresponds to absorption and subsequent instantaneous emission of a photon via a virtual energy level, which is

fundamentally different than direct photon absorption that results in an electronic transition, as in the fluorescence process. The efficiencies of these scattering processes are very low. The Raman scattering process is very weak, compared to Rayleigh scattering, where a small fraction of the incident photons (approximately 1 in 10 million) are inelastically scattered.[2] These scattered energy differences can be quantified by subtracting the measured energy of the incident light from the

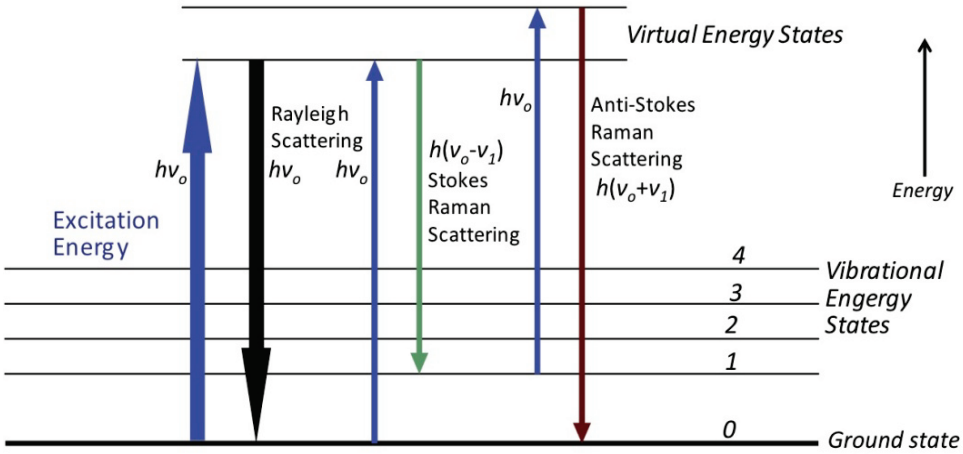

Figure 2.1 Simplified Jablonski diagram illustrating spectroscopic transitions corresponding to Rayleigh scattering ($h\nu_o$), and Stokes ($h(\nu_o-\nu_1)$) and anti-Stokes ($h(\nu_o+\nu_1)$) Raman scattering. The laser excitation frequency is ν_o.

measured energy of the scattered light. The energy differences are equal to the difference of the vibrational and rotational energy levels of the molecule. Every molecule has unique vibrational and rotational energy levels, which can be used as a molecular fingerprint of the molecule. By collecting and analyzing Raman scattered photons a molecule can be identified. The technique to analyze and study the vibrational, rotational and other low-frequency inelastic scattered modes in a system is called Raman spectroscopy. In this thesis we are interested in the Stokes Raman inelastically scattered photons. A typical Raman spectrum consists of

scattered photon intensity plotted as a function of Raman shift $\Delta\nu$, as shown in Figure 2.2, where a Raman spectrum of a monolayer of benzene-thiol (C_6H_5SH, see inset, Figure 2.2) chemisorbed on the *Au* nanopyramid (NPy) surfaces developed in this thesis.

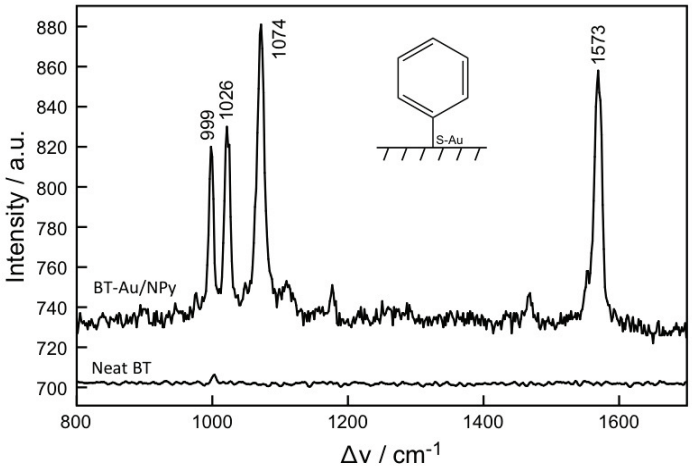

Figure 2.2 Raman spectrum of a monolayer of benzene-thiol (C_6H_5SH) chemisorbed on an *Au* NPy surface with λ_o=632.8 nm laser excitation. The lower plot shows the Raman spectrum of neat benzene-thiol using the same measurement conditions. The Rayleigh scattered photons have been removed with an edge filter. The Stokes Raman frequency shift is negative and is commonly plotted as positive values.

Each peak of the Raman spectrum corresponds to a given Raman shift relative to the incident light energy $h\nu_o$. The Raman shift is expressed as

$$\Delta\nu = 10^7\left(\frac{1}{\lambda_0} - \frac{1}{\lambda_1}\right) \tag{2.1}$$

where $\Delta\nu$ is the Raman frequency shift expressed in wavenumbers [cm^{-1}], λ_0 [nm] is the excitation wavelength, and λ_1 [nm] is the Raman shift wavelength. The

intensity I_R [W] of the Raman scattered photons is proportional to the induced dipole $\vec{p}_{ind}$ of the molecule by the excitation light source

$$I_R \propto \left|\vec{p}_{ind}\right|^2 \propto \left|\vec{\alpha}\vec{E}_o\right|^2 \tag{2.2}$$

where $\vec{\alpha}$ is the molecular polarizability tensor, which describes the responsiveness of the molecule and is dependent on the molecular confirmation, and $\vec{E}_o$ is the electric field of the excitation light source. Because the Raman spectra reveal the energy transfer between the photons and molecules during their interaction, a change in the molecular polarization potential or amount of deformation of the electron cloud with respect to the vibrational coordinate is required for a molecule to exhibit Raman scattering. In principle, almost all molecules are Raman active, which makes Raman spectroscopy a powerful spectroscopy tool for studying many types of matter.

Another well-known molecular identification method, complementary to Raman spectroscopy, is infrared (IR) spectroscopy. IR spectroscopy exploits the fact that molecules absorb specific frequencies that are characteristic of their structures. The absorbed frequencies are related to the molecular vibration and rotation energy levels. The IR spectra are also expressed in wavenumbers. However, an IR-active molecule must be associated with changes in the permanent dipole. It is well known that IR spectroscopy is severely limited for applications requiring analysis in an aqueous environment due to the strong IR absorption of water molecules, which tends to be broad and masks other vibrational information. Raman spectroscopy can be performed in an aqueous environment due to weak inelastic scattering by water outside the *OH* stretch and *HOH* bending bands of the water molecule. In general, Raman spectroscopy can be performed with aqueous samples and is currently used in biological cell applications and is expected to be an

important technique in medical diagnostics. Since the measured intensities from Raman scattering is extremely weak, compared to IR absorption for IR active molecules, IR spectroscopy is widely used in organic chemistry for identifying molecular functional groups and molecules.

2.1.2 Raman scattering

Raman scattering is described classically as the polarization induced in a molecule by the oscillating electric field of the excitation light source. This induced electrical dipole then radiates scattered light, with (Raman), and without (Rayleigh) exchanging energy with vibrations in the molecule. The induced electric dipole moment $\vec{p}_{ind}$ [C m] can be approximated as[3]

$$\vec{p}_{ind} = \vec{\alpha}\vec{E} = \alpha E_o \cos(2\pi\nu_o t) \tag{2.3}$$

If the molecule is vibrating with a frequency ν_o [s^{-1}], the nuclear displacement q [m] is composed of normal modes

$$q = q_o \cos(2\pi\nu_s t) \tag{2.4}$$

where q_o is the vibrational intensity and we assume that α is a linear function of q_o, when the molecule vibration intensity is small. For small vibrational intensities we can expand the polarizability using a Taylor expansion

$$\alpha = \alpha_0 + \left(\frac{\partial\alpha}{\partial q}\right)_0 q_0 + \ldots \tag{2.5}$$

Combining equations 2.3, 2.4 and 2.5, results in the following equation

$$\vec{p}_{ind} = \vec{\alpha}\vec{E} = \alpha_o E_0 \cos(2\pi\nu_0 t) + \frac{1}{2}\left(\frac{\partial\alpha}{\partial q}\right)_0 q_0 E_0 \left[\cos(2\pi(\nu_0+\nu_1)t) + \cos(2\pi(\nu_0-\nu_1)t)\right] \quad (2.6)$$

Assuming that the polarized electrons will radiate light at the frequency of their oscillations, equation 2.6 demonstrates that light will be scattered at three frequencies. The first term, $\alpha_o E_0 \cos(2\pi\nu_0 t)$, represents Rayleigh scattering and the second term corresponds to Raman scattering, where the frequency $\nu_0+\nu_1$ corresponds to anti-Stokes scattered photons and $\nu_0-\nu_1$ to Stokes scattered photons. The observed intensity of the Raman scattering is proportional to the scattering cross section of the molecule σ [cm^2 molecule^{-1}], where the magnitude of σ is related to $d\alpha/dq$ from equation 2.5.[3] One consequence of this theory is the variation of Raman intensity with frequency $I_R = \mu\left(\nu_0 \pm \nu_j\right)^4 \alpha_j^2 q_j^2$, where μ is a constant and j indicates a vibration mode. The ν^4 factor is derived from the classical treatment of scattering from an oscillating induced dipole. An alternative description of the measured intensity is commonly used $I_R = I_o \sigma_j D dz$, where I_o is the laser intensity, D is the number density of scatterers [molecules cm^{-3}], and dz is the path length of the laser in the sample[4]. Since most commercial spectrometers have as output a photon flux ϕ_R [photon s^{-1}], then $\phi_R = \phi_o \sigma_j^0 \nu_o (\nu_o - \nu_j)^3 D dz$, where ϕ_R scales with $\nu_o(\nu_o-\nu_j)^3$ rather than $(\nu_o-\nu_j)^4$ in the case of I_R. The Raman scattering cross-section σ includes scattering in all directions and the measurement of ϕ_R requires light collection over 4π steradians. In practice, it is more convenient

to define the differential Raman scattering cross-section $d\sigma_j/d\Omega$ [cm^2 molecule^{-1} sr^{-1}], where Ω represents the solid angle of collection[4]. In this case

$$\phi_R = \phi_o k \frac{d\sigma_j}{d\Omega} \nu_o (\nu_o - \nu_j)^3 D dz \tag{2.7}$$

where k is a constant. Table 2.1 lists some commonly reported differential cross-section values[3].

Table 2.1 Measured Raman cross-sections[4-7]

Sample	λ_o (nm)	$d\sigma_j/d\Omega$ (cm^2 molecule^{-1} sr^{-1}, $\times 10^{30}$)
Benzene liquid, 992 cm^{-1}	647 514.5	10.6 30.6
Cyclohexane liquid, 802 cm^{-1}	647 514.5	2.1 5.2
N_2 gas, 2331 cm^{-1}	514.5	0.43
H_2O liquid, 1595 cm^{-1}	514.5	0.11
Benzene, neat, 992 cm^{-1}	514.5	28.6
Rhodamine 6G, 1510 cm^{-1}	632	2400
Pyridine, 1004 cm^{-1}	514.5	11
Pyrazine, 1004 cm^{-1}	514.5	16

2.1.3 Raman selection rules

In order to determine whether the molecule is Raman active or not, selection rules must be applied to each normal vibration. For IR absorption, the molecular vibration can be detected if the dipole momentum is changed during the normal vibration. The Raman active molecule should have polarization change during the normal vibration, which means that the rate of polarizability change with the vibration must not be zero ($d\alpha/dq \neq 0$). From group theory, it is known that if a

molecule has a center of symmetry, like CO_2 or N_2, it will be IR inactive and Raman active.

2.2 Surface enhanced Raman scattering/spectroscopy

More than three decades ago the first observation of large Raman scattering enhancements, or SERS, of pyridine adsorbed from aqueous solution onto roughened silver electrodes was reported[8] and later the enhancements were attributed to strong electromagnetic fields induced by laser excitation of surface plasmon polaritons (SPP) on nanoscale noble metal (*Au*, *Ag* and *Cu*) structures at wavelengths in the visible spectrum[9]. The enhanced electromagnetic field can transfer energy to molecules located near the surface of the nanostructures, which increases the magnitude of the induced molecular dipole, and therefore, the intensity of the inelastically scattered photons increases and greatly enhances the Raman scattering efficiency[10,11]. It is commonly accepted that the electromagnetic model does not account for all of the SERS effects, such as molecular resonances and charge-transfer transitions, which can affect inelastic scattering[12], however, it is commonly accepted that the dominant effect causing the large scattering enhancement is due to an electromagnetic property of metal nanostructures[13]. Raman signal enhancements spanning several orders of magnitude, compared to normal Raman scattering, down to the single-molecule level have been reported[14-17].

2.2.1 Introduction

The discovery of SERS has resulted in an increased application of Raman spectroscopy for molecular identification and detection at low sample concentrations, which provides a unique capability for the label-free detection and identification of a variety of different analytes. Using SERS for quantitative

chemical analysis is fundamentally dependent on the ability to fabricate metallic nanostructures with nanometer-scale precision while maintaining high reproducibility at the micrometer to millimeter scales. The SPP excitation that the metal surface can support is dependent on the size and geometry of the nanostructure, and the dielectric function of the material, which all have a profound effect on the overall ability of the surface to enhance the Raman scattering cross-section of molecules adsorbed on the metal surface.

SERS-active substrates consist of metal nanostructures with geometrically controlled shape, size, and spacing that are assembled in colloidal nanoparticle suspensions, nanoparticles on solid substrates, or lithographically patterned metal nanostructures on solid substrates. New methods to create nanostructured materials and surfaces are constantly being developed and too numerous to list here. Colloidal suspensions of *Ag* nanoparticles were found to have similar properties as roughened *Ag* electrodes[18] and early work in measuring resonance Raman spectra from low concentrations of rhodamine-6G (R6G)[19] set the stage for single molecule resonance Raman measurements[14-17]. Many different nanoparticle shapes and sizes have been reported[20-25]. Since large enhancement factors have been attributed to closely spaced nanoparticle dimers, or *hot-spots*[26], molecular tethers have been designed to control spacing dimensions[27]. Although, colloidal nanoparticle suspensions are attractive SERS substrates, due to their preparation simplicity, they suffer from poor reproducibility due to a lack of control in nanoparticle dimensions, dimer spacing, and orientation with respect to the excitation polarization.

Many different types of SERS solid-support substrates have been reported over the last three decades, such as templated colloidal crystal films, deposited metal island films, and lithographically defined thin films. Electrochemically roughened metal surfaces have been reported extensively, however, have relatively low Raman enhancement factors and poor enhancement reproducibility[28]. Bottom-up

colloidal self-assembly and nanofabricated templates are inexpensive manufacturing methods. Arrays of sphere segment nanovoids used as SERS electrodes have been reported[29]. Another templating method uses nanowires to form metal nanopillar films[30]. Despite the simplicity, most of the bottom-up approaches also suffer from low reproducibility of SERS activity[31]. Lithographically patterned SERS-active substrates have been reported for more than two decades and still constitute one of the most promising manufacturing methods. Nanosphere lithography has been used to fabricate two types of SERS-active surfaces, including triangular nanoparticle arrays[32] and metal film over nanosphere surfaces[20]. Gold NPy arrays with nanoscale sharpness tips have been reported[33]. Substrates fabricated with electron beam lithography have been reported extensively[34]. Other techniques include nanoimprint lithography[35] and focused ion beam milling[36]. Lithographically patterned and etched microscale pyramidal pits in silicon coated with thin metal layers have been reported as tunable SERS-active substrates[37]; however, the number of scattering sites was limited. More recently, arrays of nanoscale metal-coated pyramidal pits in silicon were used for screening plasmonic materials[38]. Despite the impressive progress that has been made over the last three decades there is still strong demand for SERS substrates with large numbers of scattering sites with large Raman enhancements accompanied by high reproducibility and stability.

2.2.2 Surface enhanced Raman scattering

It is generally accepted that two different types of enhancement mechanisms dominate the SERS phenomena: an electromagnetic effect and a chemical effect[13]. The relative importance of the two effects is still being scrutinized, but it is commonly accepted that the electromagnetic enhancement effect is the dominant

factor. Assuming that the two enhancement factors are independent then the integrated photon flux from a SERS experiment can been estimated as[39]

$$\phi_{SERS} = \frac{I_o}{\hbar\omega_o}\sigma\sum_{i=1}^{N} G_i^{EM} G_i^{Ch} \tag{2.8}$$

where I_o and $\hbar\omega_o$ are the laser intensity, G_i^{EM} and G_i^{Ch} are the electromagnetic and chemical parts of the overall enhancement factor, respectively, and N is the number of scatterers in the probe volume[39]. We will concentrate on the electromagnetic enhancement effect for the remainder of the thesis. The electromagnetic enhancement is due to the amplification of the incident electric field E_o on the nanotextured metal surface. The electromagnetic SERS effect has been described as a consequence of the enhancement of both the incident electric field and the scattered electric field. Assuming the enhancement is independent of the absolute photon fluxes and polarizations, then the electromagnetic enhancement factor for a Stokes scattering process can be expressed as[40]

$$G^{EM}(\vec{r},\omega) = \left[\frac{E_{Loc}(\vec{r},\omega_o)}{E_o(\vec{r},\omega_o)}\right]^2 \cdot \left[\frac{E_{Loc}(\vec{r},\omega_o-\omega_1)}{E_o(\vec{r},\omega_o-\omega_1)}\right]^2 \tag{2.9}$$

where E_o and E_{Loc} are the magnitude of the incident electric field an the total local electric field, respectively, that is generated in the metal nanostructure. The incident radiation has frequency ω_o and the scattered radiation has vibrational frequency ω_1. Equation 2.9 can be approximated as

$$G^{EM}(\vec{r},\omega) = \left[\frac{E_{Loc}(\vec{r},\omega_o)}{E_o(\vec{r},\omega_o)}\right]^4 \tag{2.10}$$

which indicates that the most important factor in the electromagnetic enhancement factor is the local electromagnetic field $E_{Loc}(\vec{r},\omega_o)$ near the metal nanostructure[39]. The local field can be expressed as the sum of the incident field and the induced field, which is generated by the electrodynamic response of the metal nanostructure and dielectric interface

$$E_{Loc}(\vec{r},\omega) = E_o(\vec{r},\omega) + E_{Ind}(\vec{r},\omega) \tag{2.11}$$

There are many techniques to estimate the electrodynamically induced field $E_{Ind}(\vec{r},\omega_o)$ and Chapter 3 describes the use of a two-dimensional numerical using a commercially available finite difference time domain simulation code to determine the enhancement factors as a function of the nanostructure shape and dimensions and the frequency of the incident excitation frequency.

2.2.3 SERS substrate requirements

From the previous discussion, we can summarize some figures of merit that can be used to assess the quality of a SERS substrate:

1. Small metal features, such as nanogaps, with nanoscale separation.
2. Large surface area with high density and uniform nanogaps.
3. Easily aligned with the incident light polarization. It will be more convenient that the substrate is polarization independent.
4. The substrate can be easily cleaned and reused without strong interference from the previous measurement.

It is well known that a metal (typically *Au* or *Ag*) single nanoparticle can enhance the Raman signal by G^{EM}~10^4×. A pair of nanoparticles (dimer pair) with a nanogap separation less than 5 nm can produce extremely large enhancements to the Raman signal G^{EM}~10^{10}×. Most of the nanoparticle aggregates can be considered as nanogaps. However, it is very difficult to control the separation distance between the dimer pair. Another drawback for the nanoparticle dimers is that they are highly dependent on the excitation light polarization, and therefore are not very convenient to find the optical working condition with fixed light polarization. Both of these systems cannot be cleaned and reused for the next sample. The third type of SERS substrate consists of nanogaps, which can enhance the Raman signal G^{EM}~10^9×. Although the enhancement factor is not as large as in the nanoparticle dimer case, it is well characterized and the enhancement is strong enough to even perform single molecule SERS for certain molecules.

2.3 SERS applications

Raman spectroscopy is a technique that can be used for molecular and chemical identification, and surface spectroscopy. However, the weak signal from normal Raman spectroscopy has limited its broad application. SERS really boosted the field because the Raman signal can be enhanced by several orders of magnitude. In the past few decades, SERS has been applied to chemical and biological molecular identification, new drugs innovation and cell research. Based on this, numerous Raman spectra were recorded based on different molecules under different environment[41-47]. Highly related to the chemical identification, pharmacists are also interested to know the chemical structure and identify the molecules[48, 49]. SERS is widely applied in the field of biology, such as the

identification of DNA[50-52], protein[53-55], and bacteria[56, 57]. All these applications have been reported for in vitro measurement as well as in vivo measurement[58].

2.4 Conclusion

Based on the properties of Raman spectroscopy, the development of SERS substrate and the broad applications in SERS, we can conclude that a good SERS substrate can help, not only in conventional chemistry, but also it shows great potential in other fields, such as biology and medical diagnostics. It is necessary to design and fabricate new type of SERS substrate that can provide Raman signal with better enhancement, high uniformity with convenient light polarization alignment. In order to achieve this goal, we have designed and fabricated high density gold coated silicon NPy surfaces, which can enhance Raman scattered signal more than million times with high surface uniformity. All of this properties indicated that the high-density NPy arrays could be broadly applied for molecular identification, biological detection or drug screening.

References

1. Raman, C.K.; Krishnan, K.S. *Indian J. Phys.* 1928, 2, 387.
2. Turrell, G.; Corset J. *Raman Microscopy, Developments and Applications*, Elsevier Academic Press, 1996.
3. Long, D. *The Raman Effect: A Unified Treatment of the Theory of Raman Scattering by molecules*. John Wiley & Sons Ltd.: 2002.
4. McCreery, R.L. *Raman Spectroscopy for Chemical Analysis*. Wiley Interscience: 2000.
5. Blackie, E.; Le Ru, E.C.; Meyer, M.; Timmer, M.; Burkett, B.; Northcote, P.; Etchegoin, P.G. *Phys. Chem. Chem. Phys.* 2008, 10, 4147.
6. Wu, D.Y.; Hayashi, M.; Lin, S.H.; Tian. Z.Q. *Spectrochim. Acta A* 2004, 60, 137.
7. Weaver, M.J.; Farquharson, S.; Tadayyoni, M.A. *J. Chem. Phys.* 1985,82,4867.
8. Fleischmann, M.; Hendra, P.J.; Mcquillan, A.J. *Chem. Phys. Lett.* 1974, 26,163.
9. Moskovits, M. *J. Chem. Phys.* 1978, 69, 4159.
10. Jeanmaire, D.L.; VanDuyne, R.P. *J. Electroanal. Chem.* 1977, 84, 1.

11. Albrecht, M.G.; Creighton, J.A. *J. Am. Chem. Soc.* 1977, 99, 5215.
12. Otto, A. *Top. Appl. Phys.* 1984, 54, 289.
13. Moskovits, M. *J. Raman Spectrosc.* 2005, 36, 485.
14. Kneipp, K.; Wang, Y.; Kneipp, H.; Perelman, L.T.; Itzkan, I.; Dasari, R.; Feld, M.S. *Phys. Rev. Lett.* 1997, 78, 1667.
15. Nie, S.M.; Emory, S.R. *Science* 1997, 275, 1102.
16. Michaels, A.M.; Nirmal, M.; Brus, L.E. *J. Am. Chem. Soc.* 1999, 121, 9932.
17. Dieringer, J.A.; Wustholz, K.L.; Masiello, D.J.; Camden, J.P.; Kleinman, S.L.; Schatz, G.C.; VanDuyne, R.P. *J. Am. Chem. Soc.* 2009, 131, 849.
18. Creighton, J.A.; Blatchford, C.G.; Albrecht, M.G. *J. Chem. Soc. Farad. T2.* 1979, 75, 790.
19. Hildebrandt, P.; Stockburger, M. *J. Phys. Chem.* 1984, 88, 5935.
20. Alvarez-Puebla, R.A.; Rodriguez-Lorenzo, L.; Pastoriza-Santos, I.; Mazzucco, S.; Stephan, O.; Kociak, M.; Liz-Marzan, L.M.; de Abajo, F.J.G. *J. Am. Chem. Soc.* 2009, 131, 4616.
21. McLellan, J.M.; Li, Z.Y.; Siekkinen, A.R.; Xia, Y.N. *Nano Lett.* 2007, 7, 1013.
22. Wang, H.; Halas, N.J. *Nano Lett.* 2006, 6, 2945.
23. Lu, Y.; Liu, G.L.; Kim, J.; Mejia, Y.X.; Lee, L.P. *Nano Lett.* 2005, 5, 119.
24. Jackson, J.B.; Halas, N.J. *P. Natl. Acad. Sci. USA* 2004, 101, 17930.
25. Link, S.; El-Sayed, M.A. *J. Phys. Chem. B* 1999, 103, 4212.
26. Inoue, M.; Ohtaka, K. *J. Phys. Soc. Jpn.* 1983, 52, 1457.
27. Anderson, D.J.; Moskovits, M. *J. Phys. Chem. B* 2006, 110, 13722.
28. Moskovits, M. *Rev. Mod. Phys.* 1985, 57, 783.
29. Coyle, S.; Netti, M.C.; Baumberg, J.J.; Ghanem, M.A.; Birkin, P.R.; Bartlett, P.N.; Whittaker, D.M. *Phys. Rev. Lett.* 2001, 87, 176801.
30. Shanmukh, S.; Jones, L.; Driskell, J.; Zhao, Y.P.; Dluhy, R.; Tripp, R.A. *Nano Lett.* 2006, 6, 2630.
31. He, L.; Natan, M.J.; Keating, C.D. *Anal. Chem.* 2000, 72, 5348.
32. Hulteen, J.C.; VanDuyne, R.P. *J. Vacu. Sci. Technol. A* 1995, 13, 1553.
33. Lin, T.H.; Linn, N.C.; Tarajano, L.; Jiang, B.; Jiang, P. *J. Phys. Chem. C* 2009, 113, 1367.
34. Gunnarsson, L.; Bjerneld, E. J.; Xu, H.; Petronis, S.; Kasemo, B.; Kall, M. *Appl. Phys. Lett.* 2001, 78, 802.
35. Li, Z.Y.; Tong, W.M.; Stickle, W.F.; Neiman, D.L.; Williams, R.S.; Hunter, L.L.;Talin, A.A.;Li, D.;Brueck, S.R.J. *Langmuir* 2007, 23, 5135.
36. Brolo, A.G.; Arctander, E.; Gordon, R.; Leathem, B.; Kavanagh, K.L. *Nano Lett.* 2004, 4, 2015.
37. Perney, N.M. B.; Baumberg, J.J.;Zoorob, M.E.; Charlton, M.D.B.; Mahnkopf, S.; Netti, C.M. *Opt. Express* 2006, 14, 847.
38. Gao, H.W.; Henzie, J.; Lee, M.H.; Odom, T.W. *P. Natl. Acad. Sci. USA* 2008, 105, 20146.

39. Xu, H.; Baus, M. *Phys. Rev. E.* 2000, 61, 3249.
40. Otto, A. *Surface-Enhanced Raman Scattering: "Classical" and "Chemical" Origins, in Light Scattering in Solids IV, Eds. M. Cardona and G. Güntherodt, Topics in Applied Physics*. Springer-Verlag: 1984.
41. Michota, A.; Kudelski,; A. Bukowska, J. *J. Raman Spectrosc.* 2001, 32, 345.
42. Kudelski, A.; Michota, A.; Bukowska, J. *J. Raman Spectrosc.* 2005, 36, 709.
43. Wrzosek, B.; Bukowska, J.; Kudelski, A. *J. Raman Spectrosc.* 2005, 36, 1040.
44. Lee, H.M.; Kim, K.; Kim, M.S. *J. Raman Spectrosc.* 1993, 24, 661.
45. Lee, T.G.; Kim, K.; Kim, M.S. *J. Raman Spectrosc.* 1991, 22, 339.
46. Leopold, N.; Cinta-Pinzaru, S.; Szabo, L.; Ilesan, D.; Chis, V.; Cozar, O.; Kiefer, W. *J. Raman Spectrosc.* 2010, 41, 248.
47. Feng, Z.C.; Liang, C.H.; Li, M.J.; Chen, J.; Li, C. *J. Raman Spectrosc.* 2001, 32, 1004.
48. Corrigan, D.K.; Salton, N.A.; Preston, C.; Piletsky, S. *J. Pharm. Pharmacol.* 2010, 62, 1195.
49. Kneipp, K.; Kneipp, H.; Itzkan, I.; Dasari, R.R.; Feld, M.S. *Curr. Sci.* 1999, 77, 915.
50. Murphy, C.J.; Mahtab, R.; Caswell, K.; Gearheart, L.; Jana, N.R.; Hammami, S.; Best, D.D. *Nanoparticles and Nanostructured Surfaces: Novel Reporters with Biological Applications,* SPIE--The International Society for Optical Engineering, 2001.
51. Lee, S.J.; Baik, J.M.; Moskovits, M. *Nano Lett.* 2008, 8, 3244.
52. Kim, N.H.; Lee, S.J.; Moskovits, M. *Nano Lett.* 2010, 10, 4181.
53. Sengupta, A.; Thai, C.K.; Sastry, M.S.R.; Matthaei, J.F.; Schwarz, D.T.; Davis, E.J.; Baneyx, F. *Langmuir* 2008, 24, 2000.
54. Pieczonka, N.P.W.; Moula, G.; Aroca, R.F. *Langmuir* 2009, 25, 11261.
55. Ahern, A.M.; Garrell, R.L. *Langmuir* 1991, 7, 254.
56. Driskell, J.D.; Shanmukh, S.; Liu, Y.; Chaney, S.; Hennigan, S.; Jones, L.; Krause, D.; Tripp, R.A.; Zhao, Y.P.; Dluhy, R.A. *Appl. Spectrosc.* 2009, 63, 1107.
57. Tripp, R.A.; Dluhy, R.A.; Zhao, Y.P. *Nano Today* 2008, 3, 31.
58. Qian, X.M.; Peng, X.H.; Ansari, D.O.; Yin-Goen, Q.; Chen, G.Z.; Shin, D.M.; Yang, L.; Young, A.N.; Wang, M.D.; Nie, S.M. *Nat. Biotechnol.* 2008, 26, 83.

Chapter 3

Plasmons and surface plasmon polaritons

The basic physical phenomena behind the field of plasmonics, which is concerned with devices that exploit the unique optical properties of metallic nanostructures thus enabling the nanoscale manipulation of light, is described and its relationship to surface enhanced Raman scattering/spectroscopy (SERS). The ability of metal nanostructures to couple electromagnetic radiation into electromagnetic surface modes, which are called surface plasmon polaritons (SPP) that consist of propagating modes, and most importantly, localized surface plasmon polaritons (LSP). The relationship behind LSP and SERS is described, and finally the nanotextured surfaces developed in this thesis are analyzed with a two-dimensional numerical simulation model.

3.1 Introduction

The term *plasmonics* was first used to describe devices that exploit the unique optical properties of metallic nanostructures that enable the nanoscale manipulation of light[1]. Although there has been a renewed interest in the optical properties of metal nanostructures, their unique properties have been observed and studied over 100 years ago with reports from Wood[2] describing reflection anomalies from patterned metallic surfaces and the analytical solution to Maxwell's electromagnetic field equations revealing the optical absorption spectrum of small ($D<<\lambda_o$, where D is the diameter of the spherical nanoparticles and λ_o is the excitation wavelength) *Au* nanoparticles by Mie[3]. Further back in time, one prominent use of metal nanoparticles has been the staining of glass windows and ceramic pottery as seen the Lycurgus cup from the Byzantine empire, 4th century A.D.[4]. Plasmonics has enabled a wide array of potential applications, which includes thermally assisted magnetic recording[5], thermal cancer treatment[6], catalysis and nanostructure growth[7], electro-optic modulators[8], biosensing[9], and most importantly, with respect to this thesis, surface enhanced Raman spectroscopy[10-12]. It has been established that the unique optical properties are derived from the metals ability to support collective light-induced electronic excitations, known as surface plasmons, on metallic nanostructures and act as optical antennas that capture and concentrate light waves by squeezing the light into nanoscale volumes. Further advancements in plasmonics rely on the ability to engineer metallic nanostructures with well-defined dimensions and separation distances.

3.1.1 Plasmons

In 1956, Pines[13] first introduced the term plasmon to describe the quantum of elementary excitation associated with the high-frequency collective motion of the valence electrons in a solid due to Coulomb interactions between the valence electrons. The plasmon energy is

$$\hbar\omega_p = \hbar\left(\frac{Nq^2}{\varepsilon_0 m_0}\right)^{1/2} \tag{3.1}$$

where ω_p is the plasma frequency, N is the number of valence electrons per unit volume, ε_0 is the permittivity of free space, and m_0 is the free electron mass. Pines studied the characteristic collective energy losses observed when fast electrons were scattered by thin solid films, which was linked to the plasmon excitation in solid materials. Plasmons are rapid oscillations of electron density in conductive media, such as metals, semiconductors, and plasmas. In noble metals, such as *Ag*, *Au* and *Cu*, the plasmons are described as a free electron density that oscillates around the fixed positive ions at a plasma frequency ω_p, which ensure the neutrality of the metal atom. Electrons in metals at the top of the energy distribution (near the Fermi level) can be excited into different energy and momentum states by photons from an external electromagnetic field, and therefore, the optical response of a metal in the visible and infrared energy regime is dominated by the interaction photons and the free-electron plasmons and the subsequent electromagnetic waves in a metal are then called plasmon polaritons, which are mixed photon–plasmon modes. The optical response of the collection of free electrons can be obtained from a simplified Lorentz harmonic oscillator model (ω_p=0) giving a dielectric function for the free electrons in the metal[14]

$$\varepsilon(\omega) = 1 - \frac{\omega_p^2}{\omega^2 + i\gamma\omega} \tag{3.2}$$

where γ is a damping constant resulting from electron-electron and electron-phonon scattering in the metal. The corresponding real and imaginary parts of the dielectric function are

$$\varepsilon_1(\omega) = 1 - \frac{\omega_p^2}{\omega^2 + \gamma^2}$$
$$\varepsilon_2(\omega) = \frac{\omega_p^2 \gamma}{\omega\left(\omega^2 + \gamma^2\right)} \tag{3.3}$$

The plasmon plays a very important role in the optical properties of metal. For metals, there is strong reflection for all frequencies below the characteristic cut-off frequency ω_p. If the light frequency is lower than the plasmon frequency $\omega<\omega_p$, the light will be reflected since the electron screens the light out. For light frequencies above the plasmon frequency $\omega>\omega_p$, the light will transmit through the metal because the electrons cannot react fast enough to screen it. In most metals, the plasmon frequency is ultraviolet, lending to their shiny surfaces. For example, *Au* has $N\approx 5.9\times10^{29}$ m^{-3}, which gives $\omega_p\approx1.4\times10^{16}$ rad s^{-1} and $\lambda_p = 2\pi c/\omega_p\approx138$ nm. Some metals, such as *Ag*, *Au* and *Cu*, have electronic inter-band transitions in the ultraviolet-visible (UV-Vis) range, whereby specific energies are absorbed, which yield their characteristic colors. The inter-band transitions in real metal materials can affect the optical response. For example, the inter-band absorption of *Au* has a strong effect on the optical properties due to the bandgap between the d-band and the Fermi level, which results in two inter-band transitions, $\lambda_{IB1}\approx470$ nm and $\lambda_{IB2}\approx320$ nm, which need to be included in the dielectric function. The optical

properties of *Au* have been modeled with a partially empirical dielectric function ($\lambda=2\pi c/\omega$)[15]

$$\varepsilon(\lambda)=\varepsilon_{\infty}-\frac{1}{\lambda_p^2\left(\lambda^{-2}+i\mu_p^{-1}\lambda^{-1}\right)}+\sum_{n=1,2}\frac{A_n}{\lambda_n}\left[e^{i\phi_n}\left(\lambda_n^{-1}-\lambda^{-1}-i\mu_n^{-1}\right)^{-1}+e^{-i\phi_n}\left(\lambda_n^{-1}+\lambda^{-1}+i\mu_n^{-1}\right)^{-1}\right] \quad (3.4)$$

where ε_{∞}=1.54, λ_p=177.5 nm, μ_p=14500 nm, A_1=1.27, ϕ_1=-π/4, λ_1=470 nm, μ_1=1900 nm, A_2=1.10, ϕ_2=-π/4, λ_2=325 nm, μ_2=1060 nm. In this case λ_p no longer has a direct physical meaning since plasma oscillations are affected by inter-band transitions. Since the dielectric function is complex then it can be expressed as $\varepsilon(\lambda)=\varepsilon_1+i\varepsilon_2$, where ε_1 is the real part (Re[$\varepsilon(\lambda)$]) and ε_2 is the imaginary part (Im[$\varepsilon(\lambda)$]). Chapter 5 describes the comparison of the real and imaginary parts of $\varepsilon(\lambda)$ plotted over the visible spectrum, using equation 3.4 and the experimental data from Johnson[16].

3.1.2 Surface plasmon polaritons

In 1957, Ritchie[17] described the existence of quantized surface waves of the degenerate electron gas in thin films, corresponding to longitudinal surface plasma oscillations propagating at a metal-dielectric interface. The quanta of the surface plasma oscillations was later termed surface plasmons, which propagate at the interface between the plasma and vacuum with a frequency $\omega_{spp}=\omega_p/\sqrt{2}$.[18] Surface plasmons are optically excited, and light can be coupled into standing wave or propagating surface plasmon modes through a grating or *rough* metal surface and are confined to the surface and interact strongly with external electromagnetic radiation and it is appropriate to describe the surface modes as SPP. The SPP charge density waves can only be excited with transverse electromagnetic

radiation (TM, or p-polarized) and the resulting SPP electromagnetic waves are confined to the interface between a metal-dielectric interface since the SPP propagation constant k_{spp} is greater than the wave vector in the dielectric. Figure 3.1 shows an example of the charge and electromagnetic field distribution of a planar SPP at the interface of a dielectric/metal layer stack.

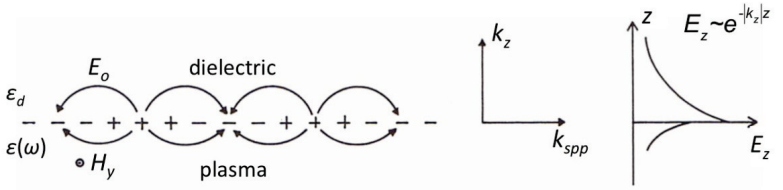

Figure 3.1 The charges and electromagnetic fields of planar SPP in the top dielectric layer and metal plasma layer with associated wave vectors. The electrical field distribution normal to the surface into the dielectric layer ε_d and metal $\varepsilon(\omega)$. The p-polarized magnetic field H_y is shown [19].

Figure 3.1 shows a schematic of the p-polarized excitation electromagnetic field (electric field E_o and magnetic field H_y). The SPP electric field (E_z) normal to the interface exponentially decreases away from the surface. The condition for existence of a SPP surface mode is $k_{spp}^2 = k_o^2(\varepsilon(\omega)\varepsilon_d / \varepsilon(\omega) + \varepsilon_d)$, which results in the dispersion relationship

$$k_{spp} = k_0 \left(\frac{\varepsilon(\omega)\varepsilon_d}{\varepsilon(\omega) + \varepsilon_d} \right)^{1/2} \tag{3.5}$$

where $\varepsilon(\omega)$ is the dielectric function of the metal, and ε_d is the dielectric constant of the upper dielectric material. Figure 3.2 shows the dispersion relation of the SPP traveling waves at a flat interface between a metal and a dielectric from equation 3.5 using the Drude lossless (γ=0) metal dielectric function (equation 3.2). The

gray region to the left of the light-line represents the dispersion of the photons for $k_o > k_{spp}$. From Figure 3.2, since the SPP dispersion curve (red solid line) lies to the right of the light line (white region) of the dielectric ($\omega = ck_o$, where c is the speed of light), and excitation of the SPP is not possible without providing phase-matching of the in-plane wave vector in the dielectric and the SPP wave vector k_{spp}.

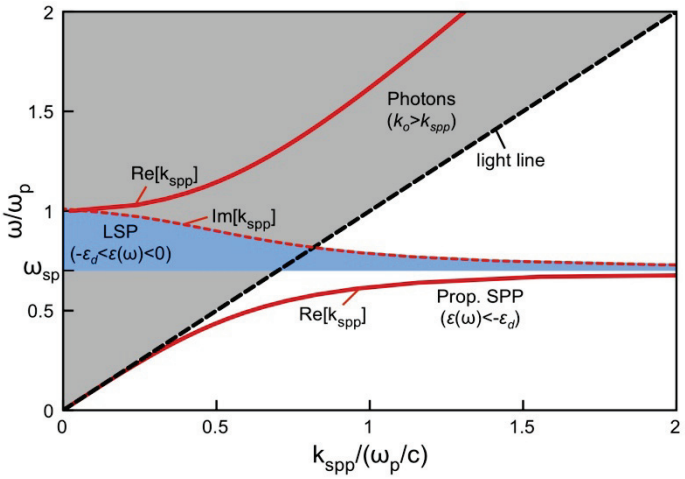

Figure 3.2 SPP Dispersion relation of a lossless Drude *Au* (equations 3.2 and 3.5) metal-air interface.

We are interested in two types of SPP modes: localized and propagating SPP modes, which are both represented in Figure 3.2. The localized SPP (LSP) correspond to non-propagating SPP modes where $-\varepsilon_d < \varepsilon(\omega) < 0$, which will be described in the next section. The energy of the evanescent surface wave is dissipated into the two waves propagating away from the surface. These modes are radiative. The propagating SPP modes correspond to propagating surfaces modes where $\varepsilon(\omega) < -\varepsilon_d$. These are non-radiative surface modes that are fully trapped at the surface that propagate along the interface, which correspond to a surface charge density wave at the surface. Figure 3.2 shows the location of both modes in the

dispersion relation. For *Au*, the dispersion relation is strongly modified from that of an ideal material due to inter-band transitions for excitation wavelengths λ_o<600 nm where the large absorption significantly affects and broadens the dispersion relation as is shown in the dispersion relation of *Au* using the dielectric function in equation 3.4. Figure 3.3 shows that wave vector k_{spp} does not diverge to ω_{sp}, as in the case of a lossless metal (Figure 3.2), but is limited by absorption (Im[k_{spp}]) in the metal, which causes the *s-shaped* dispersion curve that is known for polaritons.

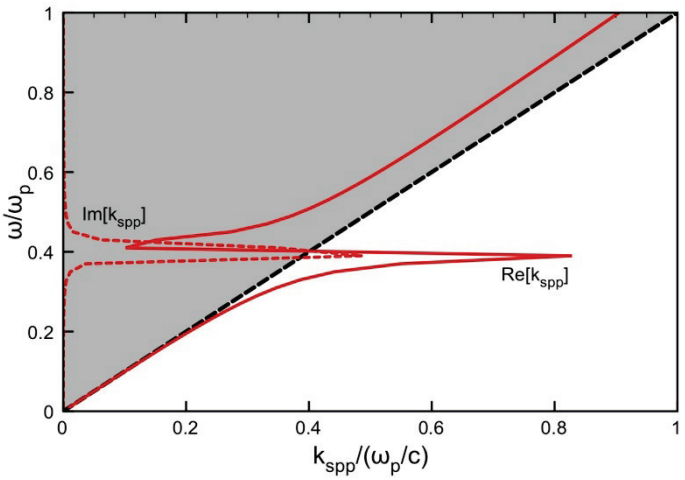

Figure 3.3 SPP Dispersion relation of a lossless Drude *Au* metal and air interface.

Since real metals have losses then the SPP wave vector will be a complex valued function and the SPPs are damped with a propagation length defined as $L_x = \left(2\,\mathrm{Im}[k_{spp}]\right)^{-1}$. The exponential decay length of the SPP in the dielectric is $L_z = k_z^{-1} = \left(k_{spp}^2 - \varepsilon_d\left(2\pi/\lambda\right)\right)$. For example, for an ideal *Au*/air interface L_x≈1000 nm and L_z≈100 nm (with λ_o=632.8 nm).

3.1.3 Localized surface plasmons

The propagating SPP behavior was described in the previous section and the dispersion relation was described for a flat metal/dielectric interface. The propagating SPP is widely used in surface plasmon resonance (SPR) and total internal reflection fluorescent (TIRF) microscopy. The propagating SPP are not the emphasis of this thesis. We are most interested in LSP that occur on nanoparticles and in gaps between closely spaced nanostructures. When the SPP occurs on metal nanostructures with dimensions comparable or smaller than the incident light wavelength, then the nature of electromagnetic surface modes of the system are highly modified and exist for a discrete values of ω [24]. When the surface plasmon is confined to a spherical nanoparticle with $D<\lambda_o$, the nanostructures free electrons participate in a collective oscillation, which is called a LSP. Figure 3.4 schematically shows the dipolar local surface plasmon optical response of metal spherical nanoparticles to polarized excitation[20].

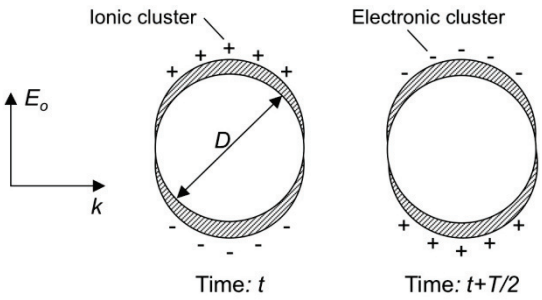

Figure 3.4 Excitation of a dipolar LSP by polarized electric field E_o with frequency $f=T^{-1}$ [20].

The positive ionic charges in the nanoparticles are assumed to be immobile and the negative conduction electrons oscillate under the influence of the external field, which results in a displacement of the negative charges from the positive ions. In

order to show how the electromagnetic surface fields at the metallic surface can be affected by the LSP, a single spherical nanoparticle model is typically analyzed due to its simplicity. Using the electrostatic approximation (quasi-static regime) and a uniform plane-wave excitation electric field, the electric field inside the metal E_{in} is given as[3]

$$E_{in} = \frac{3\varepsilon_d}{\varepsilon(\omega) + 2\varepsilon_d} E_0 \tag{3.6}$$

where E_0 is the incident electric field. In order to obtain a maximum E_{in}, $\varepsilon(\omega) \approx -2\varepsilon_d$, which, in general, is not possible for most dielectric materials since the dielectric constant is positive. Compared to the flat metal surface the local surface plasmon resonance frequency is $\omega_{lsp} = \omega_p / \sqrt{3}$. It should be noted that the displacement of the conduction electrons due to excitation field results in polarization charges at the nanoparticle surface and hence to a linear restoring force which determines the resonance frequency of the system. Thus, the conduction electrons in a spherical nanoparticle act like an oscillator system, whereas in bulk material they behave like a relaxator system where the Drude plasmon frequency ω_p is not excited by light in the bulk[20]. Some metals have negative Re[$\varepsilon(\omega)$] over a certain frequency (wavelength) range. If the absorption (Im[$\varepsilon(\omega)$]) is small at a particular wavelength where the real part of $\varepsilon(\omega) \approx -2\varepsilon_m$ then a plasmon resonance established. Therefore, the dielectric function $\varepsilon(\omega)$ plays a very important role in surface plasmon resonance effects. The real part Re[$\varepsilon(\omega)$] is responsible for the resonance of the plasmon and imaginary part Im[$\varepsilon(\omega)$] is responsible for absorption in the metal. From equation 3.6, we know that Re[$\varepsilon(\omega)$] should be negative in order to have large E_{in}, and Im[$\varepsilon(\omega)$] small at the same wavelength to minimize losses in the

metal. Among the noble metals, *Ag* and *Au* are the most commonly used for plasmonics applications. The excitation wavelength for *Au* is limited to λ_o>600 nm, due to the strong absorption near the first inter-band transition. At near infrared wavelengths the optical response of *Au* is comparable to that of *Ag*. However, with respect to SERS, there are other very important issues for SERS, which are availability, ease of manipulation, toxicity, durability, etc., and *Au* is the most promising using these considerations. Therefore, *Au* is the best choice for applications where λ_o>600 nm and *Ag* is the best for the applications requiring λ_o<600 nm.

When two spherical nanoparticles (dimers) are in close proximity at distances less than *d*~5 nm, where a nanogap is formed and the excitation radiation polarization is aligned along the inter-particle axis (Figure 3.5), the electromagnetic field magnitude in the nanogap is dramatically increased. As the distance between the metal nanoparticles *d* is reduced, their transition dipoles composed of oscillation conduction electrons couple and classical electromagnetism predicts that the enhanced fields around each particle coherently interfere[21].

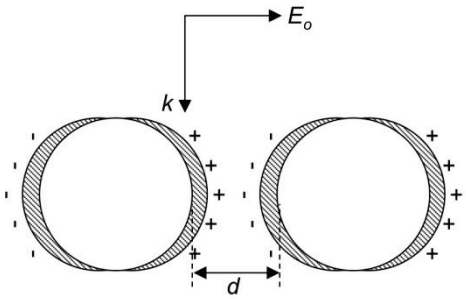

Figure 3.5 Closely spaced spherical metal nanoparticles excited electromagnetic radiation polarized along the inter-particle axis and the resulting plasmonic response.

As *d* further decreases, the coupled plasmon resonance wavelength red-shifts and the electromagnetic field enhancement further increases. The LSP modes of each nanosphere form hybridized modes and it is believed that all single-molecule SERS reports are the result of enhancements at the nanogaps and provide the largest known enhancements at surfaces[22,23].

The electromagnetic field enhancement from chapter 2 can be defined as $g(x,y,z,\omega) = |E_{Loc}(x,y,z,\omega)| / |E_0(x,y,z,\omega)|$, where $E_{Loc}(x,y,z,\omega)$ is electromagnetic field near the metal surface and $E_o(x,y,z,\omega)$ is the excitation electromagnetic field. The field enhancement is an important parameter used to assess the performance of a SERS substrate. The electromagnetic field enhancement can be huge at certain specific locations between closely spaced nanostructures, called hot-spots. The increased local field can induce a Raman dipole change dramatically and strongly enhance the Raman scattering subsequently.

3.2 Nanotextured surfaces

Although SERS was discovered more than 30 years ago[10-12], a complete explanation of the mechanism of this exciting effect is still not fully understood. However, the two mechanisms that are currently accepted to explain the effect are electromagnetic field enhancement and chemical charge transfer. The most important contribution to SERS is the electromagnetic field enhancement near the metallic nanostructure's surface and accounts for the majority of the enhancement[24]. The enhancement due to chemical charge transfer when the molecule is attached on the nanostructure's surface contributes a much smaller enhancement effect.

Currently, SERS research has been focused on making different shapes, sizes and nanostructure arrangement in order to achieve better SERS substrates. Almost all of the SERS substrates can be classified in two categories: *i.* metallic

nanoparticle based substrates, which includes nanoparticle-based suspension and nanoparticles immobilized on solid substrate; and *ii.* nanostructures fabricated directly on solid substrates. Several synthesis methods have been well studied for controlling the metallic nanoparticles shapes and sizes[25-29]. The strong SERS effect has been observed by many different types of metallic nanoparticles in suspension, such as nanostar[27], nanoshell particles[30], nanodimers and general nanoparticle aggregations[22]. The nanoparticles suspension makes the SERS measurement simple and fast. However, in order to achieve the strongest SERS effect, the nanoparticles should either form aggregations or have extremely sharp edges uniformly distributed throughout the suspension, and therefore, measurements are not reproducible, which is a major drawback of nanoparticle suspensions. Additionally, another major drawback is that the distance between particles is too difficult to control as well as alignment with the excitation light polarization in order to achieve the largest enhancements.

In order to overcome the problems associated with nanoparticle suspensions, researchers have generated SERS substrates by immobilizing metallic nanoparticles on flat solid substrates. The most popular planar substrates are glass and silicon substrates. However, adhesion of the metallic nanoparticles and the planar substrates is typically very poor. Some specific methods have been developed to immobilize nanoparticles to solid substrates. The main method has been the self-assembly method. Different self-assembly methods have been developed and the major difference among the different self-assembly methods is the attachment force that is applied to immobilize the nanoparticles. Several natural forces, such as capillary force[31, 32], chemical force[33], and electrostatic force[34,35], have all been reported as immobilization procedures. The direct transfer of pre-assembled nanoparticle film to a solid substrate has been reported[36-38]. Other

methods like growing nanoparticles directly on solid substrate using chemical or photochemical induced reaction are also reported[39].

The second category of SERS substrates involves the direct fabrication of metallic nanostructures on solid substrates. The most commonly used nanolithography method is electron beam lithography (EBL). Nanostructures can be directly written on electron sensitive photoresist and subsequently the substrate can be coated with a metal layer resulting in a nanopatterned metallic SERS surface[40]. Nanostructures fabricated using EBL on different solid substrates, and subsequent etching, have been reported[41-43]. Focused ion beam milling has been reported to pattern a nanotextured surface has been reported[44]. These nanolithography methods have helped to improve the irreproducibility common among different SERS surfaces, however, neither method is an ideal technique for making large and uniform SERS substrates with large enhancement factors.

Another technique to make nanostructures on a solid substrate is called a template technique, which begins by fabricating the template on a solid substrate. The nanotextured surface is then coated with a thin metal layer. This template technique is quite effective for making large and uniform SERS substrates and the fabrication method presented in Chapter 6 describes two types of large area subwavelength surfaces: nanogroove (NG) and nanopyramid (NPy) arrays that are fabricated with a new self-aligned silicon template method that results in ultraprecise nanoscale pitch λ_g, and most importantly, highly uniform and sharp nanoscale v-groove crevices consisting of gaps with controlled 2 nm spacing. The advantage of this approach is that the gap spacing between closely packed nanopyramid neighbors is not constrained by lithographic patterning limitations, but rather realized with the extremely precise etching of certain crystalline planes of silicon, and therefore, results in high density arrays of closely packed NPy and NG forming uniform SERS hot-spots.

3.2.1 Subwavelength pitch surfaces

Since the report of Wood[2], describing reflection anomalies from patterned metallic surfaces, a significant amount of insight has been gained about the optical properties of metals and the excitation of SPP modes[19]. Periodically roughened metal surfaces facilitate the generation of SPP excitation such that the momentum of photons in the top dielectric layer is increased by the in-plane periodicity to phase-match to the SPP. When the nanostructure periodicity is smaller than the excitation wavelength, the diffraction is zero-mode, however, an evanescent field is generated with a decay length proportional to the period of the grating that results in localized electromagnetic field enhancements near the metal surface[45]. On a metallic grating, the SPP dispersion curve splits into bands making direct coupling between the SPP and external electromagnetic radiation. For shallow (small pitch to depth ratio) gratings, it is reported that the SPP can be excited in a limited region of the dispersion curve in the zero-order diffraction region[46]. For high aspect ratio metal nanogratings the SPP dispersion curve is severely modified and resonant absorption can occur in the zero-order region. Sobnack *et al.*[47] described a model that predicted a set of reflection minima that originated from the excitation of standing wave coupled SPP. Tan *et al*.[48] and Hooper[49] reported calculated very flat SPP dispersions for short-pitch and deep metal gratings and described the stand wave resonances as hybrid waveguide-SPP resonances. Calculated electromagnetic field enhancements g~80 in nanogaps between closely spaced 30 nm diameter *Ag* half-cylinders in contact with a vacuum dielectric have been reported[50]. Subwavelength periodic patterned surfaces with Gaussian profiles have been shown to form standing wave SPP in narrow gaps with large localized electromagnetic field enhancements near the base of the nanogap[19,47]. More recently, Xuegong et al.[51] reported subwavelength gratings where the nanogap is formed by refilling the grating trench. In all reported subwavelength grating or

patterned surfaces, large localized electromagnetic field enhancements were reported near the base of the nanogap due to strong coupling between surface charges from the opposing sides of the nearest-neighbor structures. The electromagnetic field enhancement results in a Raman scattering enhancement that can be approximated as $G^{EM} \approx g^4$.[52]

3.2.2 2D numerical simulations

Nanopyramid surface cross-sections with smooth *Au* layers have been modeled using two-dimensional finite difference time domain (FDTD) calculations to determine the total electric $\vec{E}_{tot}(x,z)$, and magnetic $\vec{H}_y(x,z)$ field distributions near the metal surface of the fabricated structures. In this case $\vec{E}_{tot}(x,z) \equiv \vec{E}_{Loc}(x,z)$, as previously described. The excitation source is a normally incident plane wave with transverse-magnetic polarization where the magnetic field intensity $\vec{H}_y$ points along the length of the cavity (Figure 3.6).

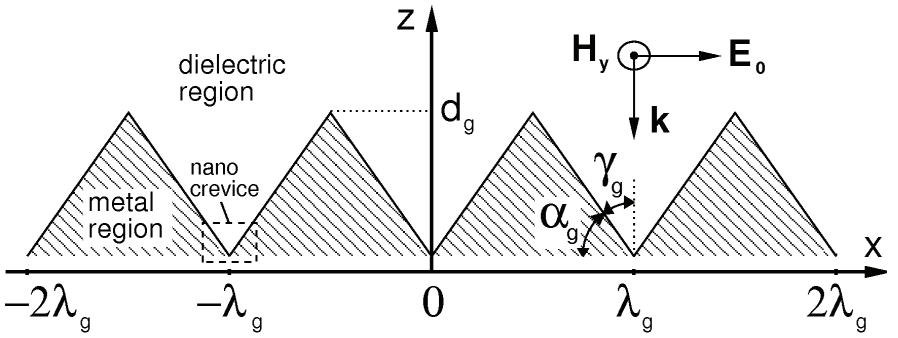

Figure 3.6 Ideal 2D NPy and NG cross-section and polarization assignment used for the steady-state FDTD simulation with λ_g=200 nm, α_g=54.7°, and γ_g=35.3°.

The 2D FDTD calculations have been performed with a commercial software package, Fullwave (RSoft, Inc.). Perfectly matched layer boundary conditions have been used at the grid edges, to eliminate reflections with 0.3 nm grid spacing. The complex frequency-dependent dielectric function $\varepsilon(\omega)$ of *Au* is represented by the Brendel-Borman model that is included in the simulation code[54]. All simulations were checked for convergence. The dielectric region is air with a relative permittivity ε_d=1.0. It should be noted that the electromagnetic field enhancement is dependent on the excitation polarization due to the rectangular geometry involved, similar to the polarization dependent enhancement nanoparticles dimers[55].

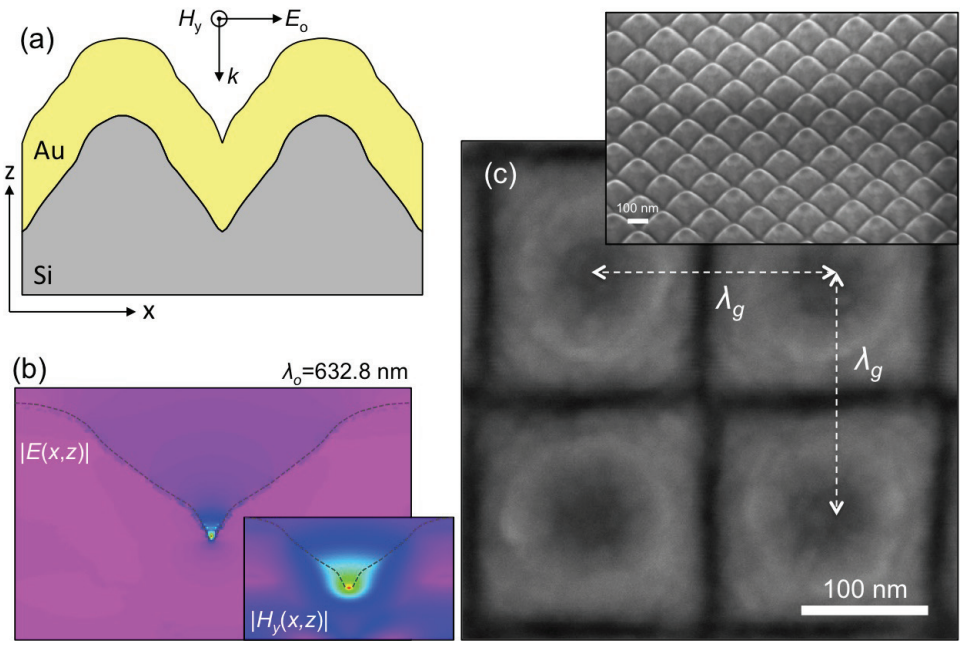

Figure 3.7 Nanogroove gap-plasmon resonators. (a) High-resolution atomic force microscopy NPy cross-section profile converted to 2D simulation model, (b) 2D FDTD simulation results showing the spatial dependence of the total electric field $\left|\vec{E}_{tot}(x,z)\right|$ and magnetic field $\vec{H}_y(x,z)$ at the base of the nanogroove region, (c) High-resolution scanning electron microscopy image of a section of a NPy surface with λ_g=200 nm.

Figure 3.7 shows the three images related to the numerical simulation of the 2D cross-section of the *Au* NPy surface. Figure 3.7a shows the 2D *Au* NPy cross-section imaged with tapping model atomic force microscopy (Dimension V SPM System, Veeco, USA) and ultra-sharp silicon tips with 2 nm average tip diameters (SSH, Nanoandmore, GmbH). The AFM imaged cross-section was translated and input into the simulator. Figure 3.7c shows a representative scanning electron microscopy image of a large area *Au* NPy surface. Figure 3.7b shows simulation results showing the spatial dependence of the total electric field $\left|\vec{E}_{tot}(x,z)\right|$ and magnetic field $\vec{H}_y(x,z)$, where $g \approx 32$. Similar to previous reports[50,55], the largest electromagnetic enhancement is localized near the base of the nanogap due to strong charge coupling between adjacent surfaces of nearest neighbor nanostructures with small separation distances. Although the calculated enhancements are large, they are smaller than previously reported[50] due to the larger entry angle $2\gamma_g$. From a surface accessibility perspective, a large entry angle is preferred, which makes the hot-spots more accessible for molecular adsorption compared to narrow and deep cavity structures. It is interesting to note that the enhancement region of the subwavelength nanopyramid and nanogroove structures are shallow v-groove structures that are very different than the Klarite[2] inverted nanopyramid enhancement region, which has four walls leading the base of the inverted structure and results in a very different enhancement mechanism and electromagnetic field distribution[56].

[2] Commercially available SERS substrates Klarite 302, Renishaw Diagnostics, Ltd.

3.3 Conclusion

The LSP greatly enhances the electromagnetic field near the metallic nanostructures, which greatly enhances the inelastically scattered photons (Raman signal) from molecules near the surface of the metallic nanostructures. The noble metals *Ag*, *Au*, and *Cu* are good materials for coupling electromagnetic radiation in the visible spectrum into LSP modes. Two-dimensional FDTD simulations show an enhancement factor of G^{EM}~10^6 for surfaces measured with high-resolution atomic force microscopy.

References

1. Brongersmaa, M.L.; Hartmana, J.W.; Atwatera, H.H. *Mater. Res. Soc. Symp. Proc.* 1999, 582, H10.5
2. Wood, R.W. *Philos. Mag.* 1902, 4, 396.
3. Mie, G. *Annalen. Der. Physik.* 1908, 330,
4. Maier, S.A.; Atwater, H.A. *J. Appl. Phys.* 2005, 98, 011101-1.
5. Challener, W.A.; Peng, C.B.; Itagi, A.V.; Karns, D.;Peng, W.; Peng, Y.Y.; Yang, X.M.; Zhu, X.B.; Gokemeijer, N.J.; Hsia, Y.T.;Ju, G.; Rottmayer, R.E.; Seigler, M.A.; Gage, E.C. *Nat. Photonics* 2009, 3, 220.
6. Hirsch, L.R.; Stafford, R.J.; Bankson, J.A.; Sershen, S.R.; Rivera, B.; Price, R.E.; Hazle, J.D.; Halas, N.J.; West, J.L. *P. Natl. Acad. Sci. USA* 2003, 100, 13549.
7. Cao, L.Y.; Barsic, D.N.; Guichard, A.R.; Brongersma, M.L. *Nano Lett.* 2007, 7, 3523.
8. Tang, L.; Kocabas, S.E.; Latif, S.; Okyay, A.K.; Ly-Gagnon, D.S.; Saraswat, K.C.; Miller, D.A.B. *Nat. Photonics* 2008, 2, 226.
9. Raschke, G.; Kowarik, S.; Franzl, T.; Sonnichsen, C.; Klar, T.A.; Feldmann, J. *Nano Lett.* 2003, 3, 935.
10. Fleischmann,M.; Hendra, P.J.; Mcquillan,A.J. *Chem. Phys. Lett.* 1974, 26, 163.
11. Jeanmaire, D.L.; Vanduyne, R.P. *J. Electroanal. Chem.* 1977, 84, 1.
12. Moskovits, M. *J. Chem. Phys.* 1978, 69, 4159.
13. Pines, D. *Rev. Mod. Phys.* 1956, 28, 184.
14. Bohren, C.F.; Huffman, D.R., *Absorption and Scattering of Light by Small Particles*. John Wiley & Sons.: 1983.
15. Etchegoin, P.G.; Le Ru, E.C.; Meyer, M. *J. Chem. Phys.* 2006, 125, 164705.
16. Johnson, P.B.; Christy, R.W. *Phys. Rev. B* 1972, 6, 4370.

17. Ritchie, R.H. *Phys. Rev.* 1957, 106, 874.
18. Stern, E.A.; Ferrell, R.A. *Phys. Rev.* 1960, 120, 130.
19. Raether, H. *Surface Plasmons on Smooth and Rough Surfaces and on Gratings*, Springer-Verlag, 1986
20. Kreibig, U.; Vollmer, M. *Optical Properties of Metal Clusters*. Springer-Verlag: 1995.
21. Michaels, A.M.; Jiang, J.; Brus, L. *J. Phys. Chem. B* 2000, 104, 11965.
22. Li, W.Y.; Camargo, P.H.C.; Lu, X.M.; Xia, Y.N. *Nano Lett.* 2009, 9, 485.
23. Nie, S.M.; Emory, S.R. *Science* 1997, 275, 1102.
24. Moskovits, M. *J. Raman Spectrosc.* 2005, 36, 485.
25. Costa, J.C.S.; Ando, R.A.; Sant'Ana, A.C.;Rossi, L.M.; Santos, P.S.; Temperini, M.L.A.; Corio, P. *Phys. Chem. Chem. Phys.* 2009, 11, 7491.
26. Giannini, V.; Rodriguez-Oliveros, R.; Sanchez-Gil, J.A. *Plasmonics* 2010, 5, 99.
27. Nehl, C.L.; Liao, H.W.; Hafner, J.H. *Nano Lett*. 2006, 6, 683
28. Zhang, T.W.; Zhang, L.; Yang, S.H.; Yang, Z.T.; Ding, B.J. *Rare. Metal. Mat. Eng.* 2007, 36, 1844.
29. Zhou, H.H.; Wu, D.Y.; Hu, J.Q.; Tian, Z.Q. *Spectrosc. Spect. Anal.* 2005, 25, 1068.
30. Le, F.; Brandl, D.W.; Urzhumov, Y.A.; Wang, H.; Kundu, J.; Halas, N.J.; Aizpurua, J.; Nordlander, P. *ACS Nano* 2008, 2, 707.
31. Abdelsalam, M.E. *Cent. Eur. J. Chem.* 2009, 7, 446.
32. Ou, F.S.; Hu, M.; Naumov, I.; Kim, A.; Wu, W.; Bratkovsky, A. M.; Li, X. M.; Williams, R.S.; Li, Z.Y. *Nano Lett.* 2011, 11, 2538.
33. Stewart, M.E.; Anderton, C.R.; Thompson, L.B.; Maria, J.; Gray, S.K.; Rogers, J.A.; Nuzzo, R.G. *Chem. Rev.* 2008, 108, 494.
34. Abalde-Cela, S.; Ho, S.; Rodriguez-Gonzalez, B.; Correa-Duarte, M.A.; Alvarez-Puebla, R.A.; Liz-Marzan, L.M.; Kotov, N.A. *Angew. Chem. Int. Edit.* 2009, 48, 5326.
35. Jang, S.G.; Choi, D.G.; Heo, C.J.; Lee, S.Y.; Yang, S.M. *Adv. Mater.* 2008, 20, 4862.
36. Alloisio, M.; Demartini, A.; Cuniberti, C.; Petrillo, G.; Thea, S.; Giorgetti, E.; Giusti, A.; Dellepiane, G. *J. Phys. Chem. C* 2007, 111, 345.
37. Anderson, D.J.; Moskovits, M. *J. Phys. Chem. B* 2006, 110, 13722.
38. Yliniemi, K.;Vahvaselka, M.;Van Ingelgem, Y.;Baert, K.;Wilson, B.P.;Terryn, H.;Kontturi, K. *J. Mater. Chem.* 2008, 18, 199.
39. Becker, M.; Sivakov, V.; Goesele, U.; Stelzner, T.; Andra, G.; Reich, H.J.; Hoffmann, S.; Michler, J.; Christiansen, S.H. *Small* 2008, 4, 398.
40. Yu, Q.M.; Guan, P.; Qin, D.; Golden, G.; Wallace, P.M. *Nano Lett.* 2008, 8, 1923.

41. Huebner, U.; Boucher, R.; Schneidewind, H.; Cialla, D.; Popp, J. *Microelectron. Eng.* 2008, 85, 1792.
42. Li, K.B.; Clime, L.V.; Cui, B.; Veres, T. *Nanotechnology* 2008, 19, 145305.
43. Oh, S.H.; Kim, J.G.; Kim, C.S.; Chang, S.; Lee, S.; Jeong, M.Y. *Microelectron. Eng.* 2011, 88, 914.
44. Masson, J.F.; Murray-Methot, M.P.; Live, L.S. *Analyst* 2010, 135, 1483.
45. Barnes, W.L.; Dereux, A.; Ebbesen, T.W. *Nature* 2003, 424, 824.
46. Chen, Z.; Hooper, I.R.; Sambles, J.R. *J. Mod. Optics* 2006, 53, 1569.
47. Sobnack, M.B.; Tan, W.C.; Wanstall, N.P.; Preist, T.W.; Sambles, J.R. *Phys. Rev. Lett.* 1998, 80, 5667.
48. Tan, W.C.; Preist, T.W.; Sambles, J.R.; Wanstall, N. P. *Phys. Rev. B* 1999, 59, 12661.
49. Hooper, I.R.; Sambles, J.R. *Phys. Rev. B* 2002, 65, 165432.
50. Garcia-Vidal, F.J.; Pendry, J.B. *Phys. Re*v. *Lett.* 1996, *77*, 1163.
51. Deng, X.G.; Braun, G.B.; Liu, S.; Sciortino, P.F.; Koefer, B.; Tombler, T.; Moskovits, M. *Nano Lett.* 2010, 10, 1780.
52. Fromm, D.P.; Sundaramurthy, A.; Schuck, P.J.; Kino, G.; Moerner, W.E. *Nano Lett.* 2004, 4, 957.
53. Ding, L.; Guo, H.; Zhang, J.Q.; Zhang, Y.K.; He, T.C.; Mo, Y. *J. Spectrosc. Spect. Anal.* 2008, 28, 2053.
54. Rakic, A.D.; Djurisic, A.B.; Elazar, J.M.; Majewski, M.L. *Appl. Optics* 1998, 37, 5271.
55. Inoue, M.; Ohtaka, K. *J. Phys. Soc. Jpn.* 1983, 52, 1457.
56. Vernon, K.C.; Davis, T.J.; Scholes, F.H.; Gomez, D.E.;Lau, D. *J. Raman Spectrosc.* 2010, 41, 1106.

Chapter 4

SERS substrate fabrication

A fabrication technology has been developed to realize nanotextured surfaces with periodically self-aligned nanopyramid (NPy) and nanogroove (NG) structures with precisely defined pitch λ_g that are closely packed with 2 nm separation gaps over large areas. The simple self-aligned fabrication technique requires only a single lithography step and wet anisotropic silicon etching. Electron-beam lithography (EBL) was first used to demonstrate the realization of tunable NPy pitch from $150 \leq \lambda_g \leq 500$ nm. The NPy and NG surfaces are coated with a thin *Au* layer, which results in strong localized surface plasmon resonance with visible frequency excitation. The fabrication method was further improved by using laser interference lithography (LIL) to uniformly pattern the two-dimensional NPy arrays over large areas (an entire 100 mm diameter silicon wafer).[3]

[3] Modified from: M. Jin, V.V. Pully, C. Otto, A. van den Berg, E.T. Carlen, High-Density Periodic Arrays of Self-Aligned Subwavelength Nanopyramids for Surface Enhanced Raman Spectroscopy, *J. Phys. Chem. C* 114, 21953, 2010.

4.1 Introduction

Despite the steady progress achieved over the last three decades, SERS substrates still have figure of merit limitations, which fundamentally depend on the ability to manufacture large area nanostructure arrays with well-controlled dimensions, geometry and polarization alignment, and most importantly hot-spot dimensions less than ~5 nm; all contribute to the enhancement of the Raman scattering cross-section of molecules adsorbed on the metal surface. Many different techniques have been reported to fabricate functional metallic SERS-active substrates. Colloidal suspensions of metal nanoparticles of various shapes and sizes have been reported[1-7] and were used to realize single molecule Raman spectra[8-11] where large enhancements were attributed to nanoparticle dimers with ~1-2 nm separations.[12] Colloidal nanoparticle suspensions are attractive due to their preparation simplicity, however, typically have poor enhancement reproducibility, which is attributed to many factors including their random composition and the lack of precise control of dimensions, dimer separation spacing, and excitation polarization alignment.

SERS-active solid-support substrates have been reported extensively over the last three decades. Low-cost non-lithographic methods have been reported, such as electrochemically-roughened surfaces, self-assembled templated colloidal films,[13,14] nanoporous templated surfaces,[15,16] shadow masked deposited metal (nanosphere lithography) island films,[17] and voids,[18] and nanocasted spherical void surfaces;[19] however, forming small and uniform separation gaps is difficult. Lithographically patterned SERS substrates still constitute one of the most promising manufacturing methods to form large arrays of reproducible hot-spots due to their commercial availability, and highly advanced patterning techniques. Patterning thin metal layers using a variety of different nanolithography techniques, such as electron-beam patterning, focused ion beam milling, holography, and nanoimprinting have been reported to realize SERS-active surfaces in a large

variety configurations, including metal discs of many shapes, sizes and gap-separations,[20-23] nanohole arrays,[24] bowtie antenna nanostructures,[25] arrays of nanoslits,[26] and gratings. Surface templates fabricated by the anisotropic etching of crystalline silicon to form nanostructured surfaces with well-controlled dimensions and sharp edges have been reported, such as the commercially available inverted pyramidal pit arrays (Klarite 302, Renishaw Diagnostics, Ltd.),[27] inverted NPy pits,[28] and sharp NPy tips.[29] Grating structures are an important class of SERS-active substrate and have been reported for over three decades,[29-40] due to well-established manufacturing and analysis methods. Early research on the optical properties of metallic gratings typically reported grating pitches near the excitation wavelength[30-35] and later reports, experimental and theoretical, developed the basic understanding of the geometry dependent optical properties of zero-mode subwavelength nanogratings;[36-40] all subwavelength nanograting structures exhibit large electromagnetic field enhancements near the base of the nanograting structure, which increases as the pitch decreases.

There remains strong demand for SERS-active substrates having a large density of uniform hot-spot scattering sites that possess large Raman enhancements with high reproducibility and stability. We present two types of subwavelength surfaces: NPy and NG arrays that are fabricated with a new self-aligned silicon template method that results in ultra-precise nanoscale pitch λ_g, and most importantly, highly uniform and sharp nanoscale v-groove crevices consisting of gaps with controlled 2 nm spacing. The advantage of this approach is that the gap spacing between closely packed NPy (pentahedrons or square pyramids) neighbors is not constrained by lithographic patterning limitations, but rather realized with the extremely precise etching of certain crystalline planes of silicon, and therefore, results in high density arrays of closely packed NPy and NG forming uniform SERS hot-spots. The drawings shown in Figure 4.1 depict arrays of NPy and NG patterns over two-

dimensional surfaces. The surface can be realized if we use single crystal silicon with (100) surface orientation as the base substrate.

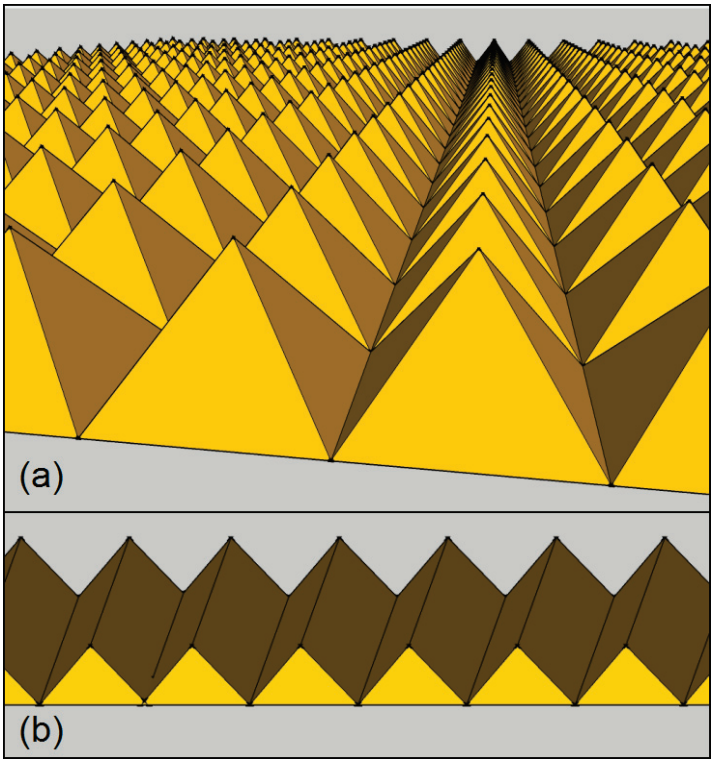

Figure 4.1 Conceptual rendering of the nanotextured silicon surfaces. (a) two-dimensional NPy (b) one-dimensional NG surface.

We use the well-established knowledge that different crystal planes have different etch rates due to the anisotropic etch rate by hydroxide ions in alkaline solutions where (111) planes have the lowest etch rate and the (100) and (110) planes have higher etch rate. Precise alignment of the nanohole array is not required due to the regularity of the single crystal silicon, which facilitates the precise formation of the

surface patterns with ultra-sharp nanogap regions. However, large misalignments will result in staggered NPy surfaces.

4.2 Nanotexturing silicon surfaces

The NPy arrays have been fabricated with a new self-aligned silicon template method based on conventional top-down microfabrication technology, including a single lithography step, wet anisotropic silicon etching, and metal deposition (Figure 4.2a). An important aspect of this approach is that the nanogap hot-spots are not formed by the lithography step, but rather the self-stopping silicon etching step. Furthermore, precise alignment of the nanohole array is not required due to the regularity of the single crystal silicon, which facilitates the self-aligned formation of the two-dimensional NPy arrays that are spontaneously formed with precisely controlled λ_g and self-aligned into uniform NPy arrays. However, large misalignments will result in staggered NPy surfaces. The surface pitch can be tuned to different dimensions by changing the mask d_{m} and hole d_{h} dimensions (Figure 4.2a).

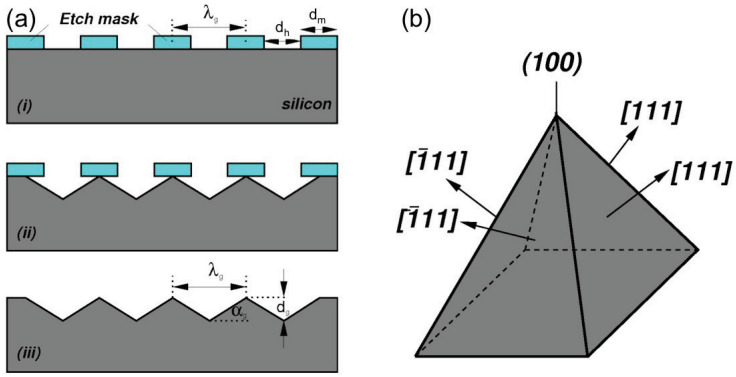

Figure 4.2 (a) basic fabrication process to realize silicon NPy surface template with $\lambda_g \approx 2d_g/\tan(\alpha_g)$ and $\alpha_g = 54.7°$ (b) crystal faces of single NPy.

The surface pattern pitch and depth are ideally linked by the silicon crystal arrangement with $d_g \approx (\lambda_g/2) \tan\alpha_g$, where $\alpha_g \approx 54.7^o$ for (100) silicon. Figures 4.2a and 4.2b show the surface cross-section and silicon crystal orientation of a single NPy, respectively. Other materials and orientations can also be considered using this general technique. We have used two methods to pattern submicron features. First, EBL is used to pattern submicron feature sizes in order to demonstrate the concept on a small area scale. We then combined the established fabrication process with LIL to realize large area (~7800 mm^2) and uniform nanotextured surfaces. Other well-established and cost-effective nanolithography methods, such as deep-UV lithography, can be used as well. Other materials and orientations can also be considered using this general technique.

4.3 EBL patterned surfaces

For the last 40 years, EBL, which uses electrons to direct write on electron sensitive materials, has been used for nanoscale photolithography. The primary advantage of EBL is that it is a convenient way to overcome the diffraction limit of light (compared to conventional optical photolithography) in realizing features with nanometer dimensions. However, the main problem with EBL is that extremely long processing times are required to pattern large areas. The EBL writing (exposure) time t can be estimated as $t=D\times A/I$, where D is the exposure dose (C/cm^2), A is the exposure area (cm^2), and I is the beam current (C/sec). For example, if we want to write an area of A=1 cm^2 with a beam current of I=1 nA and normal dose $D=10^{-3}$ C/cm^2, then the required time is $t\approx 10^6$ seconds, or about 12 days. However, if EBL is used to write an area of 10^4 μm^2, the writing time is 100 seconds, which is a quite reasonable time for research purposes and an ideal

method to demonstrate the realization of NPy and NG surfaces for the SERS application.

Since most of the structures shown in this chapter have subwavelength (optical) dimensions (λ_g< 200 nm), it is difficult to accurately characterize the structure dimensions by using conventional optical microscopy. All structures have been imaged with high-resolution scanning electron microscopy (HR-SEM, Zeiss 1550). The topography of the surface is measured using tapping mode atomic force microcopy (AFM) using ultra sharp AFM tips (average diameter: 2nm; SSH-NCH-10, NanoandMore, GmbH). The nanogap has been imaged with high-resolution transmission microcopy (HR-TEM) where a 16 mm^2 NG sample was used to make a 100 nm thick nanogap cross-section sample using a dual beam focused-ion-beam (FEI Tecnai G2 F20 X-Twin FEGTEM). The sample was transferred to a TEM grid and imaged (FEI 3D Strata DB-FIB FEG) at an acceleration voltage of 200 kV.

Figure 4.3 shows the fabrication overview in steps (a), (b), and (c). First, a periodic array (40×40 μm^2) of nanoholes was patterned in a spin-coated photoresist layer on a conventional silicon (100) wafer using EBL (FEI Sirion UHR-SEM and Raith 150 EBL system). The beam current is 100 pA, area dose is 80 $\mu C\ cm^{-2}$, line dose is 199 $pC\ cm^{-2}$, and beam writing speed is 6.46 $mm\ s^{-1}$. The maximum writing field we use is 100 μm^2. We use *lift-off* technology to transfer the *Cr* etch mask pattern onto the silicon substrate. Lift-off consists of forming an inverse image of the desired pattern onto the silicon wafer using a stencil photoresist layer, which covers certain areas on the wafer, followed by the deposition of the layer that is to be remain in the unprotected regions of the stencil layer. In the open regions of the stencil, the layer material is deposited directly on the wafer substrate, while in the covered regions the material gets deposited on top of the stencil film. After the layer material has been deposited, the wafer is immersed in a solution that can selectively dissolve the stencil layer. Once the stencil is dissolved, the layer

material is removed from the surface using lift-off, thus leaving behind the layer material that is remaining on the wafer substrate. The lift-off method offers the following advantages: *i.* composite layers consisting of several different materials may be deposited and then patterned with a single lift-off process, *ii.* etching residue that is difficult to remove is reduced, *iii.* sloped sidewalls become possible, resulting in good step coverage.

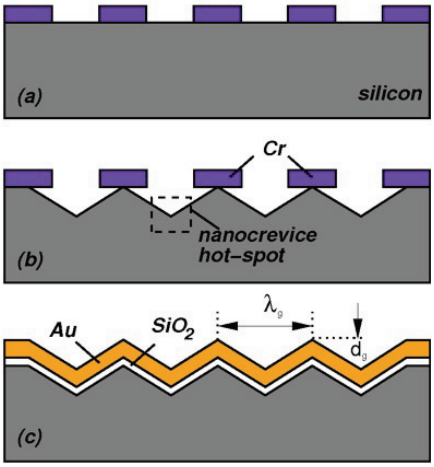

Figure 4.3 Nanotextured surfaces fabrication overview. (a) nanolithographic patterning *Cr* etch mask (b) self-stopping wet etching of NPy surfaces (c) removal of *Cr* etch mask, oxidation and deposition of the *Au* plasmonic layer with thicknesses $t_{SiO2}\approx$10 nm and $t_{Au}\approx$70 nm.

On the other hand, there are also disadvantages associated with the lift-off approach. Layer retention is the worst problem for lift-off, which can lead to unwanted parts of the metal layer remaining on the wafer surface. Redeposition will also make the sample randomly covered by the material at random locations and are typically very difficult to remove after the wafer is dried. Another disadvantage comes from sloped sidewalls where it is possible that material will collapse onto the surface during further processing. Figure 4.4 shows HR-SEM

images of typical patterned surfaces using EBL. The width and pitch of the nanoholes in the photoresist layer are 80 nm and 200 nm, respectively. After lift-off, *Cr* nanodisks with the same width and pitch are formed on the silicon substrate (Figure 4.4b). Following the formation of the *Cr* etch mask, wet anisotropic silicon etching is used to form the two-dimensional NPy silicon template. Some wet etchants etch crystalline materials at very different rates depending upon which crystal face is exposed.

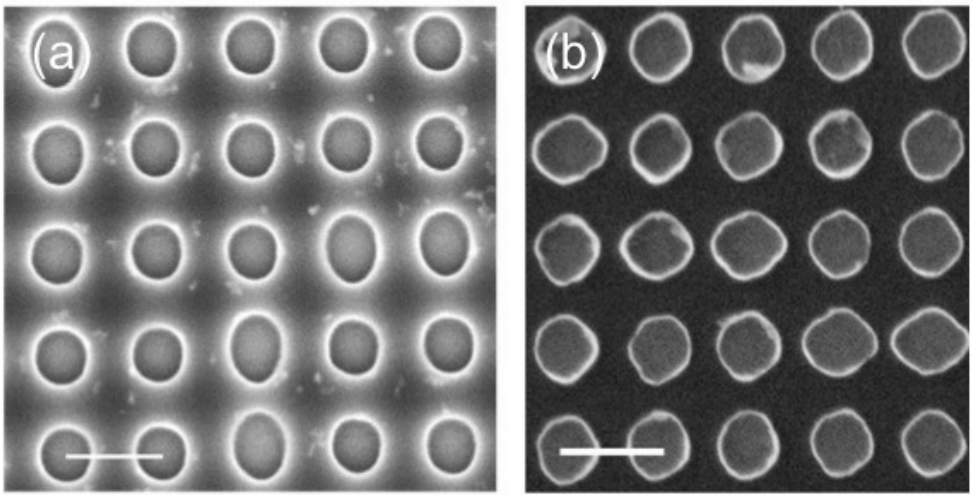

Figure 4.4 EBL patterned surfaces. (a) exposed and developed photoresist. (b) patterned *Cr* (8 nm thick) nanodisks following lift-off directly on the silicon substrate. Scale bars: 200 nm.

There are several wet etchants available for anisotropic silicon etching, such as potassium hydroxide (*KOH*). The etch rates of the different silicon surface orientations, such as (100), (110), and (111), depend on the concentration of *KOH*, temperature, and substrate impurity doping. In this work, 1% KOH at 50^{o}C was used for etching with typical etch times of 30 seconds to achieve NPy surfaces with 150 nm$\leq\lambda_g\leq$500nm. The two-dimensional NPy surfaces are spontaneously formed

during the anisotropic silicon-etching step with precisely controlled heights d_g and widths λ_g (Figure 4.3, step b). After wet etching, the substrate is gently rinsed with deionized (DI) water for 1 minute and transferred to a piranha solution (H_2O_2:H_2SO_4;1:3) for 20 minutes in order to remove all residues on the surface. After piranha cleaning, the substrate is again rinsed with DI water for 1 minute and gently blow dried by N_2 gas. The substrate is then sputtered coated with a 70 nm thick *Au* layer. Figures 4.5a-d show HR-SEM images of two-dimensional NPy surfaces at increasingly higher zoom, which demonstrates the effectiveness of this simple method to produce highly regular and repeatable nanotextured surfaces.

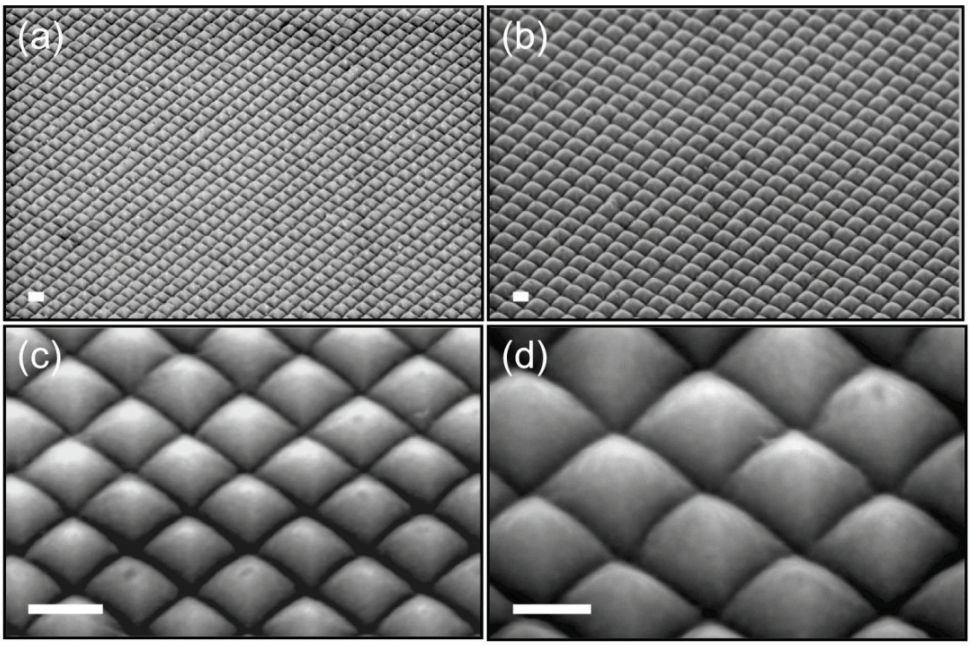

Figure 4.5 HR-SEM images of nanotextured silicon surfaces. (a)-(d) two-dimensional NPy surfaces. All scale bars: 200 nm.

The high precision and repeatability over large areas is evident. Currently, we have achieved minimum lateral dimensions λ_g~150 nm over areas of ~100×100 μm^2.

Our electron-beam patterning system that is capable of resolving a minimum d_m and d_h of around 80 nm, where $\lambda_g \approx d_m + d_h$ (Figure 4.2a), respectively.

Figures 4.6-4.8 shows examples of fabricated NPy surfaces with pitches in the range 150 nm$\leq\lambda_g\leq$500 nm, which is the practical pattern definition limit of our electron-beam patterning system.

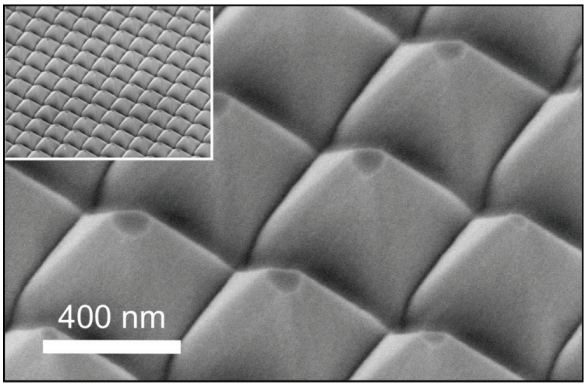

Figure 4.6 HR-SEM of NPy surfaces with λ_g= 500 nm.

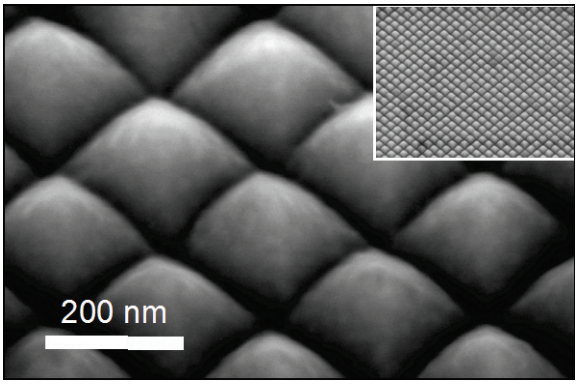

Figure 4.7 HR-SEM of NPy surfaces with λ_g= 200 nm.

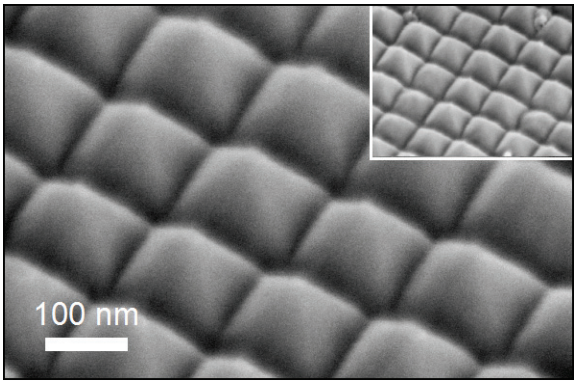

Figure 4.8 HR-SEM of NPy surfaces with λ_g= 150 nm.

An important distinction between the subwavelength surfaces presented here and inverted pyramid structures is that our new surfaces can be scaled to much smaller lateral dimensions, which results in increased Raman enhancements as well as hot-spot spatial density.

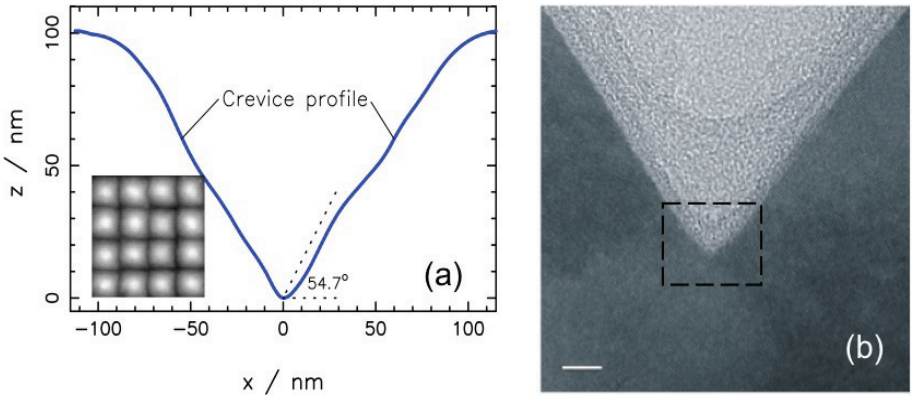

Figure 4.9 High-resolution microscopy images of crevice region (a) tapping mode AFM profile of a typical nanogap profile (b) HR-TEM image of crevice region (dash line) Scale bar: 5 nm.

Figure 4.9a shows a typical nanogap profile from a two-dimensional surface image

of the NPy array recorded with tapping mode AFM. Figure 4.9b shows a HR-TEM image of a silicon nanogap with base spacing in the ~1 nm range.

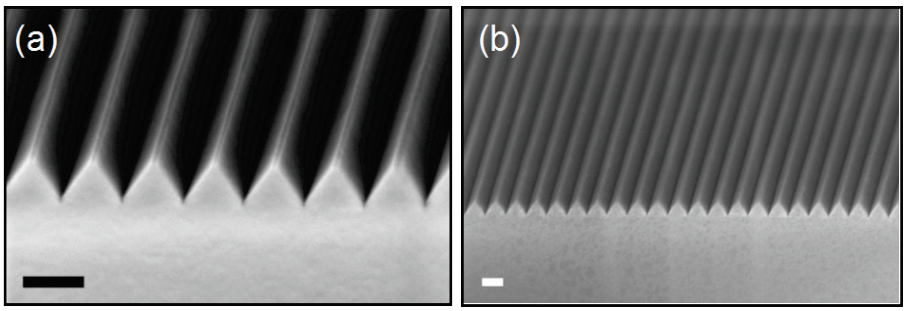

Figure 4.10 High-resolution scanning electron microscopy images of subwavelength nanotextured silicon surfaces. (a)-(b) one dimensional grating surfaces All scale bars: 200 nm.

One-dimensional NG surfaces, fabricated with a similar method,[41] have been realized and HR-SEM images are shown in Figure 4.10. Following anisotropic etching, the *Cr* nanodisk mask layer is removed (*Cr* Etchant, Technic France, 60 s), and the surfaces are thermally oxidized with a 10 nm SiO_2 layer on the exposed *Si* (111) facets. A 70 nm thick *Au* layer is subsequently deposited directly on the silicon NPy and NG surfaces. An optically thick metal film prevents radiation damping in the substrate supporting the metal film. Figure 4.11a shows an AFM image of the NPy surface following metal deposition and Figure 4.11b shows an HR-SEM image of the NPy surface after the metal deposition. The surface roughness of the *Au* layer is evident and can alter the nanogap shape. We are currently studying the effects of varying degrees of surface roughness with respect to electromagnetic field enhancements. Methods currently exist to reduce the *Au* surface roughness, such as epitaxial smooth metal deposition, flame annealing, and more recently chemical metal polishing.[42]

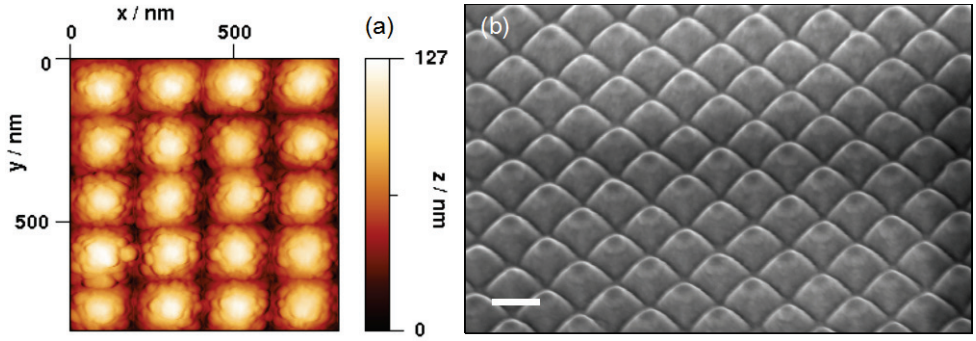

Figure 4.11 Imaging of *Au* (70 nm) coated NPy surfaces (a) HR-AFM image following (b) HR-SEM image. Scale bar: 200 nm.

4.4 LIL patterned surfaces

Interference phenomenon was discovered more than 200 years ago and occurs when two coherent light beams meet during propagation in a common medium. Nowadays, this phenomenon is used to make 1D, 2D and 3D periodic patterns in photoresist layers and is commonly referred to as laser interference lithography (LIL). Our setup is based on the Lloyd's mirror LIL system[43]. Figure 4.12 shows the basic components of the LIL instrumentation and setup. The setup uses a corner cube arrangement with 90°C geometry where the left and right halves of the beam are folded onto each other. Expanding the beam allows a large area overlap- especially when the angle of incidence is near 45°C and the beam sizes incident on the sample and the mirror are equal. The incident angle can be tuned by rotating the mirror.[44] The exposure area *EA* is limited by size of the mirror M_x (10 cm), and M_y (10 cm) and angle θ and can be estimated as $EA=M_xM_y\tan\theta$, where θ is the angle at the intersection of mirror and substrate. In order to make a periodic pattern with λ_g=200 nm pitch, the angle θ can be calculated using the equation $\lambda_g=\lambda_{LIL}(2\sin\theta)^{-1}$, where λ is the laser wavelength, (λ_{LIL}=266 nm in our case), [43] and $\theta\approx$41.7 degree. Using these parameters, the exposure area is $EA\approx$89 cm^2 (note: the surface area of a

100 mm diameter wafer is 79 cm^2). By tuning the angle θ, patterns with different pitch can be made with different exposure area.

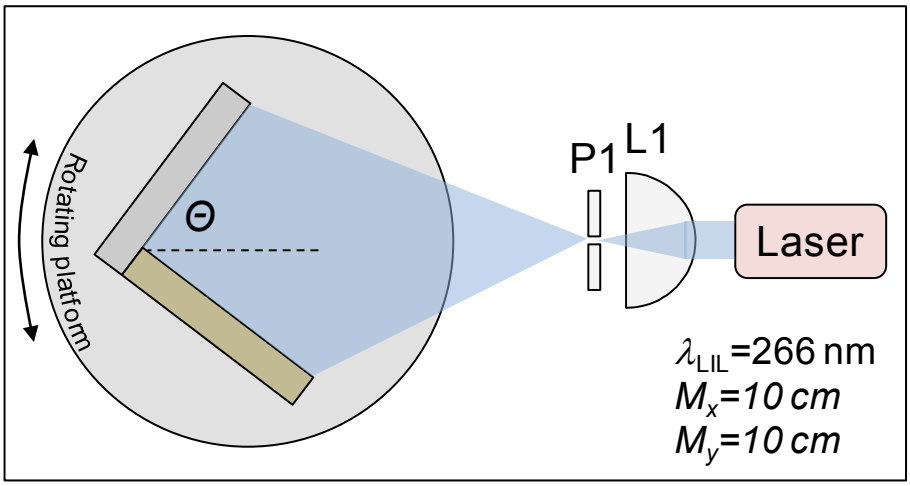

Figure 4.12 Lloyd's mirror set up for LIL[43].

For example, for λ_g=500 nm the exposure area will be $EA \approx 27$ cm^2. The fabrication procedure used to create the NPy surfaces with EBL has been modified to accommodate the LIL patterning procedure. First, the *Cr* nanodisk mask layer is replaced with a SiO_2 nanodisk etch mask layer. The SiO_2 nanodisks are created by patterning a nanohole array in a thin silicon nitride layer deposited on the silicon surface. The nanoholes in the nitride layer expose the silicon surface, which are thermally oxidized to form the SiO_2 nanodisks. The nitride etch mask is then removed and the remaining surface is exposed to the anisotropic etchant and the NPy surface geometry is spontaneously formed until only (111) silicon surfaces remain on the surface. The SiO_2 is then removed. Figure 4.13 shows a brief fabrication process.

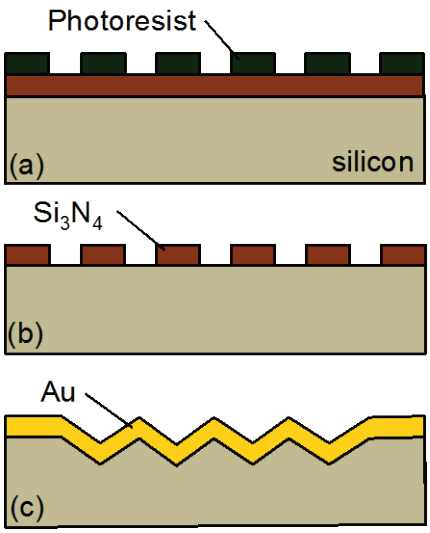

Figure 4.13 Nanotextured surface fabrication process using LIL and anisotropic etching.

The silicon nitride (Si_3N_4) layer is first deposited on the silicon surface using low-pressure chemical vapor deposition with a nominal thickness of 50 nm. The nitride layer serves two purposes: *i.* an anti-reflection layer for the LIL exposure, and *ii.* a template to form the SiO_2 nanodisk arrays. A photoresist layer (100 nm thick) was then spin cast on the nitride layer. The photoresist layer is then exposed with LIL and developed to form an RIE etch mask that is used to transfer the nanohole pattern to the nitride layer. Following the RIE step, the photoresist layer is removed revealing the nitride nanohole mask. The substrate is then thermally oxidized and a 15 nm silicon dioxide layer is formed on the silicon surface in the nanoholes and does not form on the nitride layer. The nitride layer is then removed with a hot phosphoric acid solution (180^{o}C, 15 mins.). After the removal of the nitride layer, the substrate is placed in the anisotropic wet etchant and the NPy surfaces are formed over the entire wafer surface. Figure 4.14 shows HR-SEM images of a LIL patterned wafer at different stages of the process.

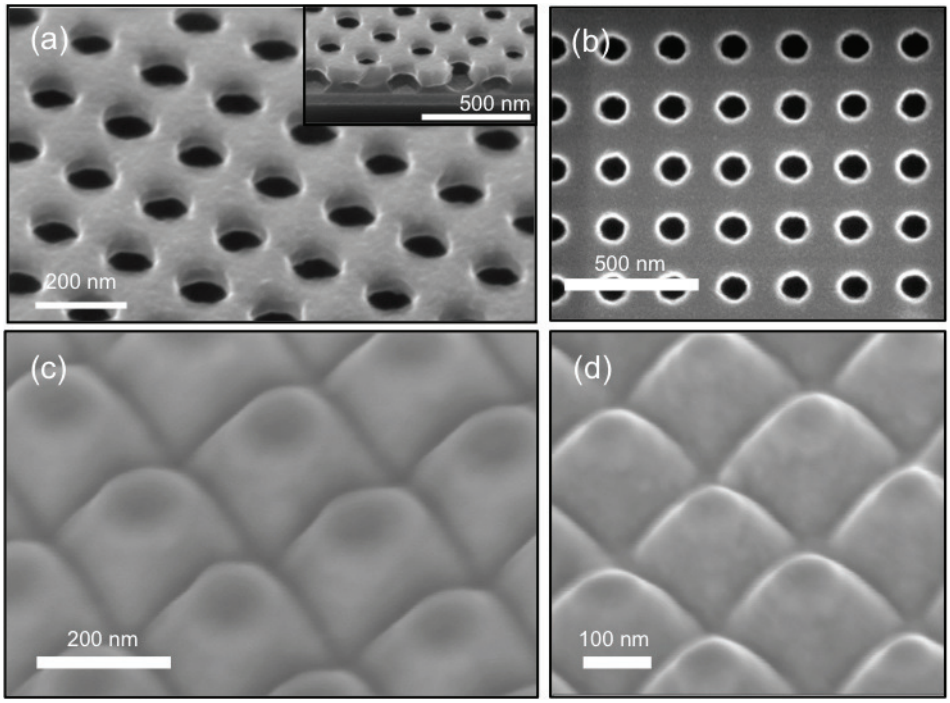

Figure 4.14 HR-SEM images of LIL NPy fabrication steps. (a) nanohole photoresist layer (b) nanohole silicon nitride layer (c) silicon NPy arrays (d) *Au* covered NPy arrays.

Figure 4.14a shows the photoresist layer following LIL exposure and development. The nanoholes in the photoresist are nominally 80 nm in diameter. Figure 4.14b shows the nanohole pattern transferred to the silicon nitride layer using RIE. Figure 4.14c shows the silicon NPy after wet anisotropic etching and nitride removal. Finally, Figure 4.14d shows the NPy surface after the deposition of the 70 nm thick *Au* layer. Figure 4.15 shows examples of large area realization of the NPy surfaces. Figure 4.15a shows a HR-SEM image of a ~225 μm^2 region of a wafer-scale (100 mm diameter) size NPy surface coated with a 70 nm thick *Au* layer. The NPy surfaces are very uniform with nearly identical pitch and alignment. Figure 4.15b shows an example of the NPy surface uniformity of the LIL patterned samples over

a surface area of a 100 mm diameter silicon wafer (~7900 mm^2). The LIL patterned surface is immersed in water that has a larger refractive index (n_d≈1.33) than air (n_d≈1.0), which results in increased optical absorption and the uniform red color across the surface. It should be noted that the 100 mm diameter NPy surface sample contains a total nanogap length of ~ 79 km. The inset in Figure 4.15b shows how the optical absorption red-shifts as the refractive index increases in the range $1.3 \leq nd \leq 1.7$.

4.5 Conclusion

We presented a new fabrication technology to realize silicon NPy and NG templates using EBL and anisotropic wet etching of the silicon surface. NPy samples with tunable pitches in the range 150 nm$\leq \lambda_g \leq$500 nm have been demonstrated. The fabricated NPy and NG substrates have been characterized by HR-SEM, HR-TEM and HR-AFM. The nanogap between adjacent NPy and NG have been measured using TEM and AFM and determined to be less than 5 nm before and after coating thin (70 nm) *Au* layer. The fabrication technology has been extended using LIL and very uniform large area (~7800 mm^2) NPy substrates have been demonstrated with high nanogap density (~1 km cm^{-2}).

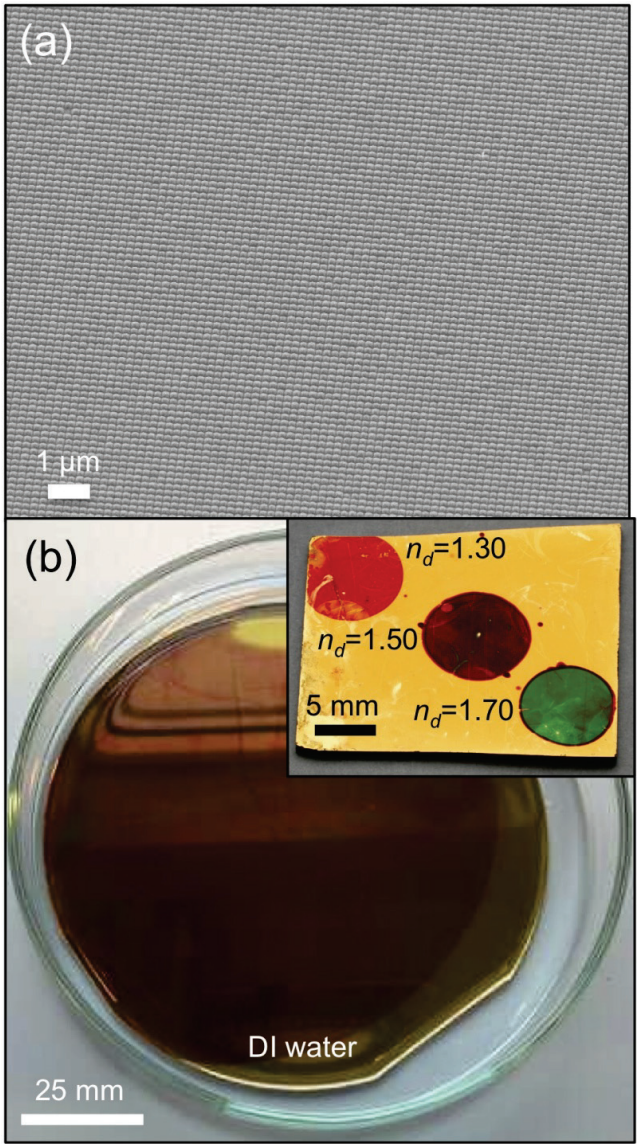

Figure 4.15 Large area images of LIL patterned NPy surfaces. (a) HR-SEM image (b) LIL patterned wafer with 70 nm *Au* layer immersed in water shows the uniform red color on the NPy surface indicating optical absorption due to localized surface plasmon resonance in the densely packed nanogaps located between adjacent NPy. Inset: large area sample (3 cm^2) and optical absorption with different dielectric materials with refractive index over the range $1.3 \leq n_d \leq 1.7$. The color shifts indicate a red-shift in the optical absorption wavelength as n_d increases.

References

1. Moskovitz, M. *J. Raman Spectrosc.* 2005, 36, 485.
2. Link, S.; El-Sayed, M.A. *J. Phys. Chem. B* 1999, *103*, 8410.
3. Wang, H.; Brandl, D.W.; Le, F.; Nordlander, P.; Halas, N.J. *Nano Lett.* 2006, 6, 827.
4. Lu, Y.; Liu, G.L.; Kim, J.; Mejia, Y.X.; Lee, L.P. *Nano Lett.* 2005, 5, 119.
5. McLellan, J.M.; Li, Z.Y.; Siekkinen, A.R.; Xia, Y. N. *Nano Lett.* 2007, 7, 1013.
6. Rodríguez-Lorenzo, L.; Álvarez-Puebla, R.A.; Pastoriza-Santos, I.; Mazzucco, S.; Stéphan, O.; Kociak, M.; Liz-Marzán, L.M.; García de Abajo, F.J. *J. Am. Chem. Soc.* 2009, 131, 4616.
7. Jackson, J.B.; Halas, N.J. *P. Natl. Acad. Sci.* 2004, 101, 17930.
8. Nie, S.; Emory, S.R. *Science* 1997, 275, 1102.
9. Kneipp, K.; Wang, Y.; Kneipp, H.; Perelman, L.T.; Itzkan, I.; Dasari, R.; Feld, M.S. *Phys. Rev. Lett.* 1997, 78, 1667.
10. Michaels, A.M.; Nirmal, M.; Brus, L.E. *J. Am. Chem. Soc.* 1999, 121, 9932.
11. Dieringer, J.A.; Wustholz, K.L.; Masiello, D.J.; Camden, J.P.; Kleinman, S.L.; Schatz, G.C.; Van Duyne, R.P. *J. Am. Chem. Soc.* 2009, 131, 849.
12. Inoue, M.; Ohtaka, K. *J. Phys. Soc. Jpn.* 1983, 52, 3853.
13. Coyle, S.; Netti, C.M.; Baumberg, J.J.; Ghanem, M.A.; Birkin, P.R.; Bartlett, P.N.; Whittaker, D.M. *Phys. Rev. Lett.* 2001, 87, 176801.
14. Shanmukh, S.; Jones, L.; Driskell, J.; Zhao, Y.; Dluhy, R.; Tripp, R.A. *Nano Lett.* 2006, 6, 2630.
15. Masuda, H.; Fukuda, K. *Science* 1995, 268, 1466.
16. Choi, D.; Choi, Y.; Hong, S.; Kang, T.; Lee, L.P. *Small* 2010, 6, 1741.
17. Hulteen, J.C.; Van Duyne, R.P. *J. Vacuum Sci. Tech. A* 1995, 13, 1553.
18. Wu, L.Y.; Ross, B.M.; Lee, L.P. *Nano Lett.* 2009, 9, 1956.
19. Bartlett, P.N.; Birkin, P.R.; Ghanem, M.A. *J. Chem. Soc. Chem. Commun.* 2000, 17, 1671.
20. Kitson, S.C.; Barnes, W.L.; Sambles, J.R. *Phys. Rev. Lett.* 1996, 77, 2670.
21. Gunnarsson, L.; Bjerneld, E.J.; Xu, H.; Petronis, S.; Kasemo, B.; Käll, M. *Appl. Phys. Lett.* 2001, 78, 802.
22. Li, Z.; Tong, W.M.; Stickle, W.F.; Neiman, D.L.; Williams, R.S. *Langmuir* 2007, 23, 5135.
23. Abu Hatab, N.A.; Oran, J.M.; Sepaniak, M.J. *ACS Nano* 2008, 2, 377.
24. Brolo, A.G.; Arctander, E.; Gordon, R.; Leathem, B.; Kavanagh, K.L. *Nano Lett.* 2004, 4, 2015.
25. Fromm, D.P.; Sundaramurthy, A.; Schuck, P.J.; Kino, G.; Moerner, W.E. *Nano Lett.* 2004 4, 957.
26. Porto, J.A.; Garcia-Vidal, F.J.; Pendry, J.B. *Phys. Rev. Lett.* 1999, 83, 2845.

27. Perney, N.M.B.; Baumberg, J.J.; Zoorob, M.E.; Charlton, M.D.B.; Mahnkopf, S.; Netti, C.M. *Opt. Express* 2006, 14, 847.
28. Gao, H.; Henzie, J.; Lee, M.H.; Odom, T.W. *P. Natl. Acad. Sci.* 2008, 105, 20146.
29. Lin, T.-H.; Linn, N.C.; Tarajano, L.; Jiang, B.; Jiang, P. *J. Phys. Chem. C* 2009, 113*,* 1367.
30. Wood, R.W. *Phil. Mag.* 1902, 4, 396.
31. Tsang, J.C.; Kirtley, J.R.; Bradley, J.A. *Phys. Rev. Lett.* 1979, 43, 772.
32. Girlando, A.; Philpott, M.R.; Heitmann, D.; Swalen, J.D.; Santo, R. *J. Chem. Phys.* 1980, 72, 5187.
33. Weber, M.; Mills, D.L. *Phys. Rev. B* 1983, 27, 2698.
34. Raether, H. Surface Plasmons on Smooth and Rough Surfaces and on Gratings; Springer: Berlin, Germany 1988.
35. Baltog, I.; Primeau, N.; Reinisch, R. *Appl. Phys. Lett.* 1995, 66, 1187.
36. García-Vidal, F.J.; Pendry, J.B. *Phys. Rev. Lett.* 1996, 77, 1163.
37. Sobnack, M.B.; Tan, W.C.; Wanstall, N.P.; Preist, T.W.; Sambles, J.R. *Phys. Rev. Lett.* 1998, 80, 5667.
38. Vernon, K.C.; Davis, T.J.; Scholes, F.H.; Gómez, D.E.; Lau, D. *J. Raman Spectrosc.* 2010, 41, 1106.
39. Barnes, W.L.; Dereux, A.; and Ebbesen, T.W. *Nature* 2003, 424, 824.
40. Xuegong, D.; Braun, G.B.; Liu, S.; Sciortino Jr., P.F.; Koefer, B.; Tombler, T.; Moskovits, M. *Nano Lett.* 2010, 10, 1780.
41. Chen, S.; Bomer, J.G.; van der Wiel, W.G.; Carlen, E.T.; van den Berg, A. *ACS Nano* 2009, 3, 3485.
42. Nowicka, A.M.; Hasse, U.; Hermes, M.; Schoz, F. *Angew Chem. Int. Edit.*, 2010, 49, 1061.
43. Van Wolferen, H.; Abelmann, L. Laser Interference Lithography, in Lithography: Principles, Processes and Materials, Ed. T.C. Hennessey, Nova Science Publishers, Inc. 2011.
44. Van Soest, F.J.; Van Wolferen, H.A.G.M.; Hoekstra, H.J.W.M.; De Ridder, R.M.; Worhoff, K.; Lambeck, P.V. *Jpn. J. Appl. Phys. 1*, 2005, 44, 6568.

Chapter 5

SERS substrate characterization using reflectance spectroscopy

Reflection spectroscopy is used to investigate the generation of local surface plasmon resonance in narrow gaps between adjacent *Au* nanogrooves (NG) and *Au* nanopyramid (NPy) surfaces. Plasmonic coupling of a p-polarized white light source normally incident on the surface is investigated as a function of surface pitch (150 nm$\leq\lambda_g\leq$500 nm), alignment of polarization with surface structures ($0°\leq\theta\leq180°$), and different dielectric materials consisting of air, deionized water and calibrated refractive index liquids ($1.3000\leq n_d\leq1.7200$). Angle resolved reflectivity measurements were conducted on the *Au* NPy surfaces (λ_g=200 nm) coated with a thin polymer layer ($n_d\approx1.5$) as a function of incidence angle and excitation wavelength using spectroscopic ellipsometry.[4]

[4] Spectroscopic ellipsometry measurements performed in cooperation with dr. Herbert Wormeester, Physics of Interfaces and Nanomaterials Group, University of Twente, the Netherlands.

5.1 Introduction

The surface enhanced Raman scattering (SERS) effect is primarily dependent on large electromagnetic fields that accompany a local surface plasmon resonance located in metal nanogaps present on the surface of the substrate. For nanotextured surfaces having well-controlled nanogap dimensions, the local surface plasmon resonance will occur at a certain wavelength (or energy) and the electromagnetic field enhancement in the nanogap region will be maximum at the resonance wavelength, and therefore, the electromagnetic SERS enhancement factor will also be maximum[1]. Therefore, it is very important to understand the local surface plasmon resonance characteristics of a new SERS substrate. The most popular methods to study the local surface plasmon resonance are dark-field transmission spectroscopy and reflection spectroscopy[2-9]. For colloidal nanoparticle solutions, dark-field transmission spectroscopy is very convenient since the colloid solution is transparent[10]. Transmission spectroscopy can also be applied to transparent substrates, such as glass[1]. For opaque substrates, reflection is the most commonly employed method, which compares the intensity of incident light with reflected light and scattered light[11]. In our case, the silicon base substrate is opaque in the visible spectrum, and therefore, we use normal incidence reflection spectroscopy to characterize the *Au* NG and *Au* NPy surfaces.

5.2 Optical properties of real metals

One of the most important technological characteristic optical features of metals is that they strongly reflect light and appear shiny. The shiny appearance is due to their very high reflection coefficients, which is caused by the interaction of the light with the free electrons present in the metal. For metals, there is strong reflection for all frequencies below a characteristic cut-off frequency called the

plasma frequency ω_p, as was discussed in Chapter 3. From Chapter 3, we described that qualitatively the optical response of metals can be described by the Drude model for a free-electron gas, where the metal dielectric function is defined as $\varepsilon(\omega) = 1 - \omega_p^2 / \omega^2 + i\gamma\omega$, and γ is a damping rate constant. Although the Drude model is useful to gain a qualitative understanding of the basic physical behavior of surface plasmon polariton and local surface plasmon resonance behaviors, it is not sufficient to make quantitative predictions. In real metals, inter-band transitions affect the optical response. For *Au*, the inter-band absorption has a strong effect on the optical properties due to the bandgap between the d-band and the Fermi level[12], which results in two inter-band transitions, $\lambda_{IB1} \approx 470$ nm and $\lambda_{IB2} \approx 320$ nm, which need to be included in the dielectric function. The optical properties of *Au* have been modeled with a partially empirical dielectric function[13]

$$\varepsilon(\lambda) = \varepsilon_\infty - \frac{1}{\lambda_p^2\left(\lambda^{-2} + i\mu_p^{-1}\lambda^{-1}\right)} + \sum_{n=1,2} \frac{A_n}{\lambda_n}\left[e^{i\phi_n}\left(\lambda_n^{-1} - \lambda^{-1} - i\mu_n^{-1}\right)^{-1} + e^{-i\phi_n}\left(\lambda_n^{-1} + \lambda^{-1} + i\mu_n^{-1}\right)^{-1}\right] \quad (5.1)$$

where ε_∞=1.54, λ_p=177.5 nm, μ_p=14500 nm, A_1=1.27, ϕ_1=-π/4, λ_1=470 nm, μ_1=1900 nm, A_2=1.10, ϕ_2=-π/4, λ_2=325 nm, μ_2=1060 nm. In this case λ_p no longer has a direct physical meaning since plasma oscillations are affected by inter-band transitions. Since the dielectric function is complex then it can be expressed as $\varepsilon(\lambda) = \varepsilon_1 + i\varepsilon_2$, where ε_1 is the real part of the dielectric function (Re[$\varepsilon(\lambda)$]) and ε_2 is the imaginary part of the dielectric function (Im[$\varepsilon(\lambda)$]). Figure 5.1a shows the real and imaginary parts of $\varepsilon(\lambda)$ plotted as a function of wavelength over the visible spectrum, where the dielectric function from equation 5.1 (solid lines) is compared to the experimental data from Johnson and Christy[14]. The index of refraction is also complex function of wavelength (or frequency) and is defined as

$$\tilde{N}(\lambda) = n - iK \tag{5.2}$$

where n is the real part of the refraction index and K is the imaginary part, sometimes referred to as the extinction coefficient. The complex refractive index is related to the complex dielectric function $\tilde{N} = \sqrt{\varepsilon}$, which results in $\varepsilon_1 = n^2 - K^2$ and $\varepsilon_2 = 2nK$, or $n^2 = \varepsilon_1/2 + \sqrt{\varepsilon_1^2 + \varepsilon_2^2}/2$ and $K = \varepsilon_2/2n$. Figure 5.1b shows the functional relationship of the real and imaginary parts of $\tilde{N}$ and wavelength. The reflectivity R normally incident to a plane surface can be described by the Fresnel equation

$$R = \frac{(n - n_d)^2 + K^2}{(n + n_d)^2 + K^2} \tag{5.3}$$

where n_d is the refractive index of the material in direction contact with the reflecting surface (e.g. n_d=1 for air). At angles other than normal, the reflectivity is a function of the polarization direction of the incidence beam.

Reflection spectroscopy is a non-destructive and non-contact technique that involves the measurement of light reflected from a sample with a non-patterned surface, and the corresponding spectrum is recorded. This technique is particularly useful for film thickness and refractive index measurements, as well as recording spectra of thin metal films. Figure 5.1d shows the reflectivity (dashed line: calculated with equation 5.3 and optical constants n and K from Figure 5.1b; solid line: measured) of a 70 nm thick polycrystalline *Au* layer deposited on a silicon substrate. For wavelengths above about 600 nm the reflectivity is very close to 100% and drops sharply for wavelengths in the ultraviolet, beginning at about 500 nm.

Since the inter-band transition near 500 nm will affect the plasmonic activity of the *Au* surface then we need to work with excitation laser wavelengths above about 600 nm. In later chapters where we use the NPy and NG *Au* surfaces for SERS and Raman spectroscopy we use laser excitation wavelengths of 632.8 nm (HeNe) and 785 nm (diode).

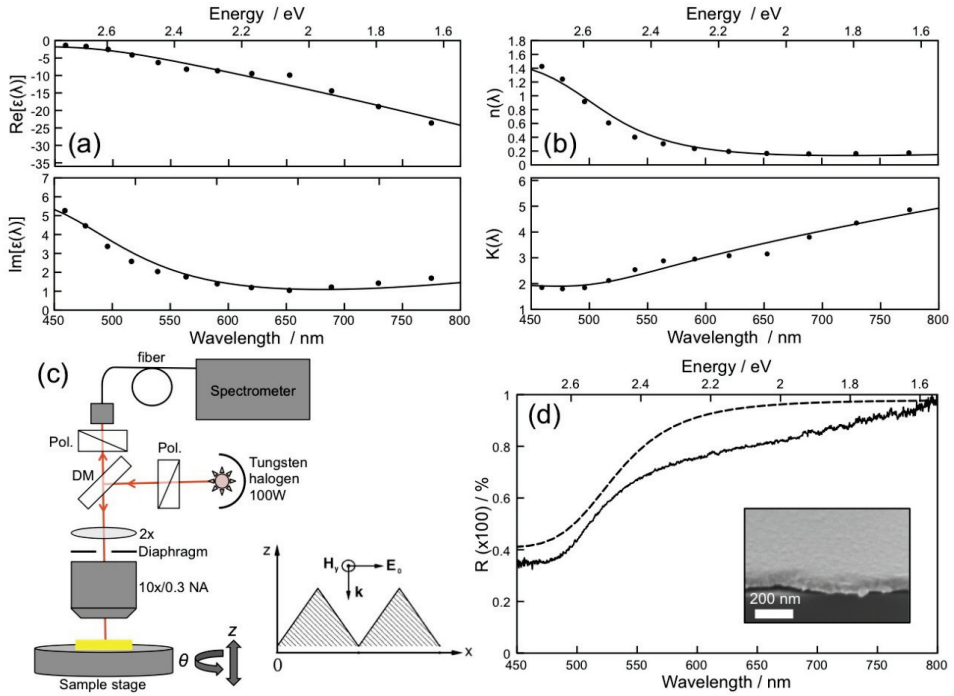

Figure 5.1 Optical properties of thin polycrystalline *Au* films used for all experiments. (a) Real and imaginary dielectric function $\varepsilon(\lambda)$ (solid line: calculated with equation 5.3; dotted line: experimental data from[14]) (b) Real and imaginary refractive index $\tilde{N}(\lambda)$(solid line: calculated with equation 5.3; dotted line: experimental data from[14]) (c) p-polarized white light reflection measurement setup with manual height z and rotation angle θ adjustment (inset: polarization alignment θ=90°) (d) Measured (solid line) and calculated (dashed line) reflectivity from a *Au* surface.

5.3 Optical properties of patterned metal surfaces

Surface plasmon polaritons (SPP) are electromagnetic waves confined to the interface between a metal-dielectric interface since the SPP propagation constant k_{spp} is greater than the wave vector in the dielectric. The dispersion relation of the SPP traveling waves at a flat interface between a metal and a dielectric can be expressed as

$$k_{spp} = k_0 \left(\frac{\varepsilon(\omega)\varepsilon_d}{\varepsilon(\omega) + \varepsilon_d} \right) \tag{5.4}$$

where $\varepsilon(\omega)$ is the dielectric function of the metal, and ε_d is the dielectric constant of the upper dielectric material, typically air ($\varepsilon_{air}\approx1$) or water ($\varepsilon_{water}\approx1.77$) for biosensing applications. As was described in Chapter 3, the SPP dispersion curve lies to the right of the light line of the dielectric ($\omega=ck$, where ω is frequency, c is the speed of light and k is the wave vector), and excitation of the SPP is not possible without providing phase-matching of the in-plane wave vector in the dielectric and the SPP wave vector k_{spp}. The most common phase-matching technique is with the use of prism coupling, which is commonly employed for commercial biosensing systems, such as the SPR Imager II (GWC Technologies, USA.). Another well-known technique is grating coupling, where the pitch of a periodically patterned surface provides the required phase-matching to generate the SPP due to scattering. Figure 5.2 shows that the in-plane component of the incident photons wave vector and a periodic grating structure with pitch λ_g can be combined to provide the required phase-matching such that $k_{spp} = k\sin\theta \pm \eta\Lambda$, where η is an integer and $\Lambda=2\pi/\lambda_g$. For gratings that have a small pitch to depth ratio, SPP excitation on metallic gratings can be described by perturbation theory and much

experimental evidence for these electromagnetic resonances has been reported[15]. It is well known that SPP excitation on shallow metallic grating structures can only be achieved in a small corner of the dispersion curve in the zero-order diffraction region[16]. The reason for this is that even with the added momentum due to scattering from the grating given to the incident radiation, the momentum of the SPP on such a structure is still close to the grazing photon momentum and it is thus excited just beyond the diffraction edge[16].

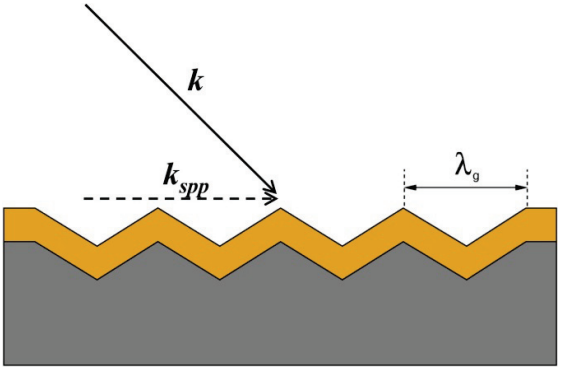

Figure 5.2 Phase-matching of incoming electromagnetic field wave vector with SPP propagation constant k_{spp} using periodic metal grating [15].

However, for high aspect ratio metallic monogratings the SPP dispersion curve may be so severely modified that resonant absorption of light due to SPP excitation may occur well within the zero-order region of the spectrum. It has been shown that such structures can display very strong optical features[17]. Subwavelength periodic patterned surfaces with Gaussian profiles have been shown to form standing wave SPP in narrow crevices with large localized electromagnetic field enhancements near the base of the crevice[18, 19]. More recently, Deng et al[20] reported subwavelength gratings where the nanogap is formed by refilling the grating trench. In all reported subwavelength grating or patterned surfaces, large localized electromagnetic field enhancements were reported near the base of the nanogaps

due to strong coupling between surface charges from the opposing sides of the nearest-neighbor structures. Other reports[21, 22] calculated the dispersion of SPPs for short-pitch deep metal gratings and found that very flat SPP bands are formed in the zero-order region of the spectrum. These flat-banded resonances are very different to the SPPs excited on shallow gratings, and have been explained as being due to hybrid waveguide-SPP resonances.

5.4 Experimental methods

Reflection spectroscopy is used to investigate the optical properties of the subwavelength *Au* NG and NPy surfaces as a function of the p-polarized white light excitation source wavelength. We expect the reflectivity to decrease to a minimum value at a certain wavelength that generates a local surface plasmon resonance in the narrow gap region between adjacent NG and NPy structures. We use the *Au* NG and NPy surfaces fabricated using the methods described in Chapter 4. The *Au* layers are all 70 nm thick and deposited using conventional sputter coating. All measurements were conducted immediately following the deposition of the top *Au* layer. Figure 5.3 shows examples of the *Au* NG and NPy surfaces in scanning electron micrograph (SEM) images. The surface pitch λ_g is defined in both figures. The inset in both surface types shows the silicon template prior to *Au* sputter coating. The samples are aligned with the polarization of the white light source of the measurement system (Figure 5.1c). In cases where the reflectivity of the flat *Au* and nanopatterned *Au* surfaces are compared the spectrometer was first calibrated with an *Al* reflectivity standard (STAN-SSS, Ocean Optics). The reflection measurement system uses a p-polarized (LPVISB100, Applied Laser Technology) white light source (100W tungsten halogen lamp) focused on the surface with a microscope objective (10×/NA 0.3, Leica) at normal incidence. A diaphragm is used to reduce the measurement area in the case where the surface pattern area is small. The reflected beam is collected by the same objective and

passed through an analyzer (p-polarizer) through a multimode fiber (QP450-1-XSR, Ocean Optics) to the spectrometer with integrated detector (HR4000, Ocean Optics).

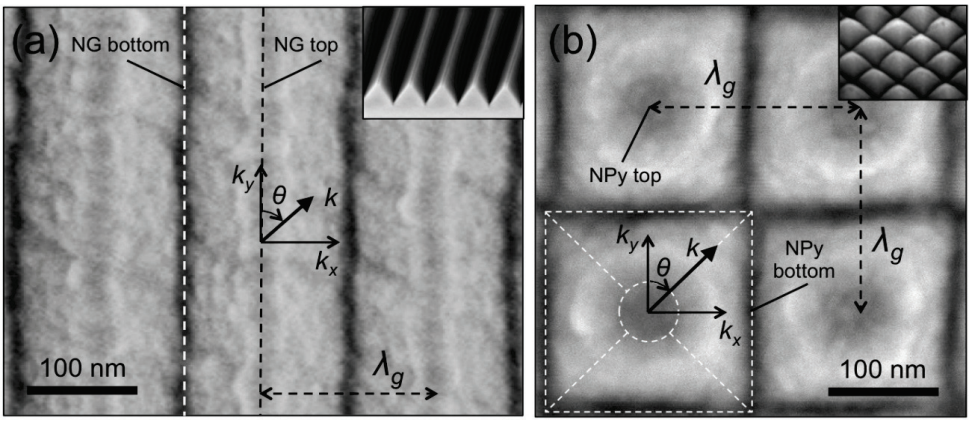

Figure 5.3 Scanning electron micrograph images of *Au* nanotextured surfaces characterized in this chapter (a) NG surface (b) NPy surface. The inset images show the silicon surfaces prior to *Au* deposition.

For all measurements a flat metal surface is used as a reference. The reflectivity behavior of the *Au* NG surfaces has been investigated in terms of polarization alignment between the excitation source and the surface structures and different dielectric materials. The in-plane component of the wave vector due to the excitation is defined here as $k = ik_x + jk_y$, where $k_x = k_0 \sin\theta$, $k_y = k_0 \cos\theta$, and i and j refer to spatial coordinates x and y, respectively. The rotation angle of the sample stage (Figure 5.1c) is varied from $0° \leq \theta \leq 180°$. For *Au* NG surfaces we expect the incoming electromagnetic field to excite the local surface plasmon resonance at θ=90° and no excitation at θ=0° and θ=180°. For *Au* NPy surfaces we expect that there will be have some level of plasmonic coupling of the incoming radiation. For θ=0° there will be plasmonic coupling to the nanogap perpendicular to the y-axis

and for θ=90° there will be coupling to the nanogap perpendicular to the x-axis. For θ=45° we expect coupling to both orthogonal nanogaps on the NPy surface. Measurements have been done with different dielectric materials using calibrated refractive index liquids: n_d=1.3000, 1.5000, and 1.7050 (all from Cargille Laboratories, USA). By varying the rotation angle θ of the sample stage we measured the reflectivity change the sample orientation with the fixed light polarization.

5.5 Results and discussion

The reflectivity of *Au* NG and NPy surfaces (λ_g=150 nm and 200 nm) substrate is first measured in air and water, and two rotation angles θ=0° and θ=90° in the case of NG surfaces, with fixed source polarization position. For all measurements shown in Figure 5.4 the spectrometer was first calibrated with an *Al* reflectivity standard in order to compare the flat *Au* and nanotextured *Au* surfaces. Figure 5.4a shows the measured reflectivity of a flat *Au* surface in air and *Au* NPy surface with λ_g=150 nm in air and water. A clear reflectivity minimum, or local surface plasmon resonance, at λ_{res}≈520 nm emerges due to a red-shift of the reflectivity minimum when the refractive index of the upper surface in increased in water. Figure 5.4b shows the measured reflectivity of a flat *Au* surface in air and *Au* NG surface with λ_g=150 nm in air and water and for θ=0° and θ=90°. A reflectivity minimum appears at 550 nm for θ=90° and n_d=1.33 for the *Au* NG surface. Figures 5.4c and 5.4d show reflectivity measurements for *Au* NPy and *Au* NG surfaces with λ_g=200 nm, respectively. The larger pitch surfaces show similar behavior with reflectivity minima in water at 535 nm and 625 nm, for *Au* NPy and *Au* NG surfaces, respectively. In all cases the reflectivity minima are very broad, which is most

likely due to inhomogeneously broadened average characteristics caused to a range of nanogap widths.

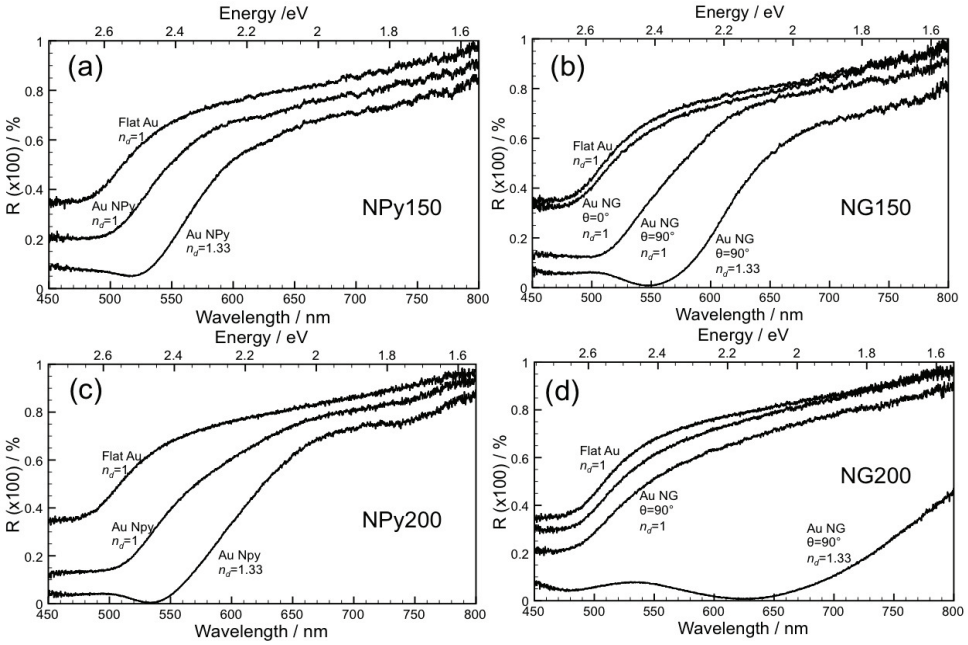

Figure 5.4 Reflectivity measurements on *Au* NG and NPy substrates in air (n_d=1) and deionized water (n_d=1.33). (a) *Au* NPy surface with λ_g=150 nm in air and water, and as-deposited flat *Au* surface in air (b) *Au* NG surface with λ_g=150 nm in air and water and different polarization, and flat *Au* surface in air (c) *Au* NPy surface with λ_g=200 nm in air and water, and as-deposited flat *Au* surface in air (d) *Au* NG surface with λ_g=200 nm in air and water and different polarization, and flat *Au* surface in air.

The excitation polarization dependence is demonstrated in the NG surfaces as coupling occurs only for p-polarized excitation (θ=90°) and not for s-polarization (θ=0°). Finally, all measurements shown in Figure 5.4 demonstrate that when the local surface plasmon resonance is near to the first *Au* inter-band transition then the plasmon coupling is reduced. From Figure 5.4, the reflectivity minimum is very

near the first *Au* inter-band transition wavelength. In order to visualize the excitation wavelength that resonantly excites the local surface plasmon clearly, the refractive index of the dielectric material was increased from n_d=1.0 (air) to n_d=1.33 (water).

The plasmonic coupling behavior as a function of the NG structure alignment with the polarization of the excitation source is shown in reflectivity measurements in Figure 5.5 in both air and water. A flat *Au* surface (70 nm thick deposited on a silicon sample) is used as a reference measurement in both dielectric medium measurements. The excitation polarization is fixed and the sample is rotated from θ=0°, where the electric field polarization (s-polarized or TE: transverse electrical) of the source excitation is parallel to the length of the NG to θ=90° where the electric field polarization (p-polarized or TM: transverse magnetic) of the source excitation is perpendicular to the length of the NG.

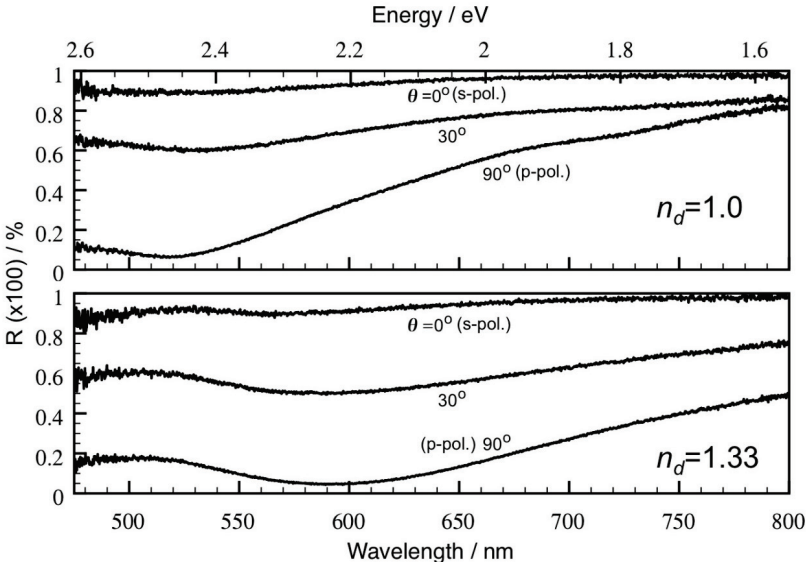

Figure 5.5 Reflectivity measurements on *Au* NG surface (λ_g=200 nm) in air (n_d=1) and deionized water (n_d=1.33) and rotation angle θ.

From Figure 5.5, the plasmonic coupling dependency on polarization alignment is clearly demonstrated where a rotation θ=0° (s-pol.) results in almost no plasmonic coupling and the subwavelength structures appear as a smooth flat surface as the reference surface. As the sample is rotated from θ=30° and θ=90° (p-pol.) the plasmonic coupling increases as evidenced by the reduction in reflectivity at the same resonant wavelength. Additionally, as described previously, an increase in the refractive index of the dielectric material produces a red-shift in the resonant wavelength. The reason for this strong polarization alignment dependency can be explained with the use of Figure 5.3a. The *Au* NG surfaces have nanogap structures that extend in only one direction, and therefore, since we require the TM polarization of the excitation radiation to be aligned perpendicular to the nanogap in order to excite the local surface plasmon resonance, therefore, alignment is critical.

In the case of *Au* NPy surfaces, reflectivity measurements do not indicate a polarization dependency, most likely due to the low extinction ratio of the polarizer. However, in Chapter 6, a polarization dependency is shown using Raman spectroscopy measurements, which further supports the argument involving the splitting of the in-plane wave vector k into components k_x and k_y, which contributes to the plasmonic coupling into the orthogonal nanogaps of the NPy surfaces. Figure 5.6 shows reflectivity measurements from *Au* NPy surfaces (λ_g=200nm) using four different dielectric materials (calibrated refractive index liquids n_d=1.300, n_d=1.500, and n_d=1.705). A flat *Au* surface with the appropriate dielectric material was used for a reference for each measurement. In air (ε_d=1.0), the reflectivity minimum occurs near λ_{res}≈505 nm, which is very close to the first *Au* inter-band transition (λ_{IB1}), and therefore, the surface plasmon resonance is weakly represented. The inset image shows an image of the *Au* NPy surface (area: 3 cm^2) in air. The addition of the refractive index liquid with n_d=1.3 (ε_d=1.7) results in a clear red-

shifted resonance minimum in the reflectivity with a wavelength of λ_{res}≈526 nm. The inset image shows a bright red color change for Δn_d=0.3. The surface is cleaned with acetone and isopropyl alcohol and dried with pure N_2. After cleaning, the index liquid with n_d=1.5 (ε_d=2.25) was added to the surface resulting in a further red-shifted resonance minimum in the reflectivity with a wavelength of λ_{res}≈558 nm ($\Delta\lambda_{res}$≈32 nm).

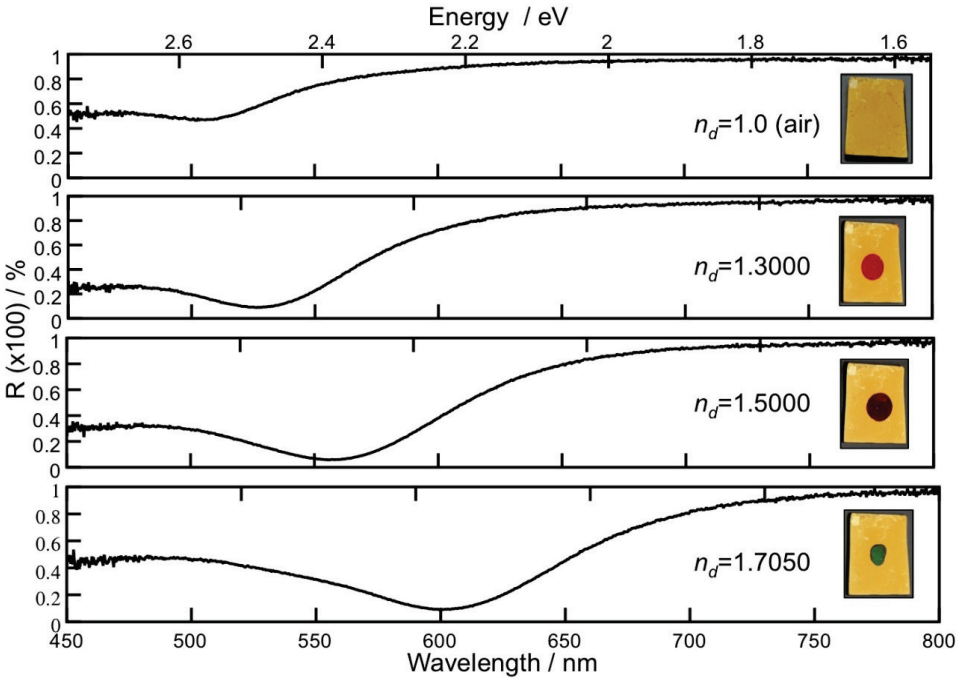

Figure 5.6 Reflectivity measurements of *Au* NPy surfaces (λ_g=200 nm) in air (n_d=1) and three different refractive index liquids (n_d=1.3000, n_d=1.5000, and n_d=1.7050). The inset images show the reflected color change associated with the index liquid. Note that the reflected color is complementary to the color associated with the resonance wavelength.

The inset image shows a purple color for Δn_d=0.3. After cleaning and drying the final index liquid with n_d=1.7050 (ε_d=2.91) resulted in a further red-shifted

resonance minimum in the reflectivity with a wavelength λ_{res}≈603 nm ($\Delta\lambda_{res}$≈42 nm). The inset image shows a green color change for Δn_d=0.205. The reflected color change associated with the refractive index liquid is complementary to the color associated with the resonance wavelength. The red-shift of the resonance wavelength can be compared to the local surface plasmon resonance properties of small spheres, which have been computed with an analytical model of the *Au* dielectric function[23].

Figure 5.7 shows a comparison of the local surface plasmon resonance wavelength shift with increasing refractive index of the top dielectric layer between the *Au* NPy (λ_g=200 nm) surfaces (dotted line) and small *Au* nanoparticles (dashed line). Using the simplified Drude model of the metal dielectric function, the resonant wavelength of small metal nanospheres is $\lambda_{res} \approx \lambda_p \left(2\varepsilon_d + 1\right)^{1/2}$, where λ_p is the wavelength of the metal plasmon.

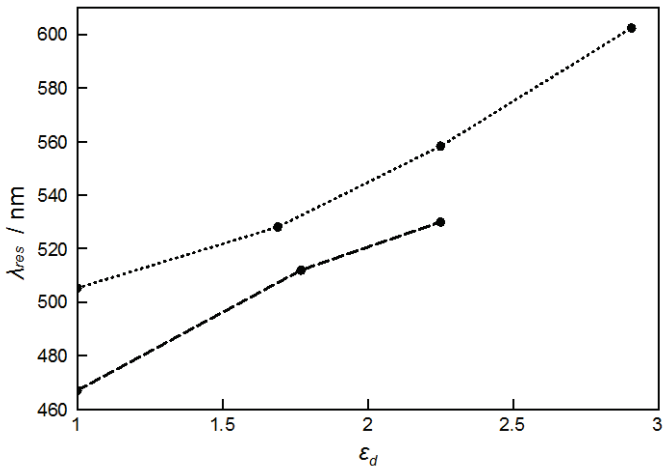

Figure 5.7 Local surface plasmon resonance shift as a function of the top surface dielectric constant ε_d ($\varepsilon_d = n_d^2$) measured for the *Au* NPy (λ_g=200 nm) surface (dotted line) and calculated for a small *Au* nanosphere (dashed line)[23].

These results indicate that a laser wavelength of 532 nm in air and water is preferred and will produce the largest electromagnetic field enhancements for SERS. However, In reality, using the 532 nm laser for the SERS measurement will not generate large field enhancements as most of the excitation energy is apparently lost due to the close proximity with the first *Au* inter-band transition. One way to overcome this problem is to increase the pitch dimensions of the NPy surfaces, which results in a red-shift of the resonance wavelength as was shown by increasing the diameter of nanoparticles[24]. By using NPy with λ_g=500 nm the resonance wavelength red-shifts λ_{res}≈550 nm in air and red-shifts further to 600 nm in water. The 500 nm pitch NPy surfaces also did not demonstrate a polarization dependence. These optical characterization results have aided in understanding the NG and NPy local surface plasmon resonance, and also greatly helped us to precisely design SERS surfaces with the largest enhancement factors.

In addition to the normal incidence reflectivity measurements, angle resolved reflectivity measurements using a conventional spectroscopic ellipsometer (VASE Ellipsometer, J.A. Woollam, Inc.) have been conducted. Since conventional measurement instruments use excitation sources that have large spot diameters (~1 mm), then this type measurement is only possible with nanotextured surfaces with very uniform and well controlled nanostructures over large surface areas, as in the case of the NPy surfaces patterned using laser interference lithography, as presented in Chapter 4. Figure 5.8 shows the measured p-polarized reflectivity R_p and s-polarized reflectivity R_s. The *Au* NPy surfaces are coated with a thin layer of polymethylmethacrylate (PMMA) with a refractive index n_d≈1.5. Figure 5.8a shows the reflectivity R_p as a function of incidence angle θ and excitation energy. The R_p minimum at θ=15 degrees and n_d≈1.5 corresponds to the normal incidence reflectivity measurements (Figure 5.6, n_d=1.5000). As the incidence angle is increased the reflectivity minimum wavelength red-shifts. The minimum

reflectivity $R_p \approx 1\%$ occurs at an incidence angle of $\theta \approx 55$ degrees. Figure 5.8b shows the reflectivity R_s as a function of incidence angle θ and excitation energy.

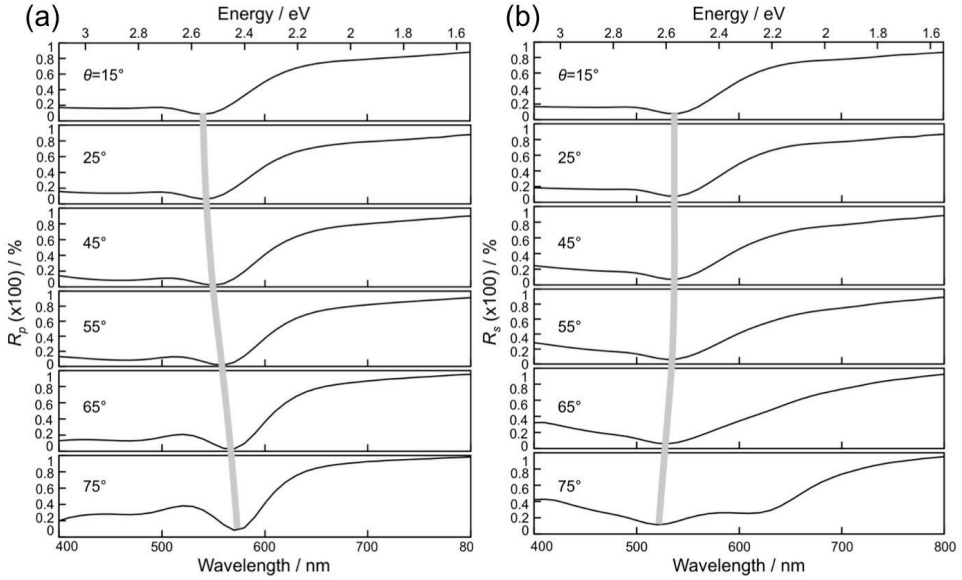

Figure 5.8 Angle resolved reflectivity as a function of the incident angle θ and excitation energy. Incidence angle is varied from $15º \leq \theta \leq 75º$, where $\theta = 0º$ is normal incidence. (a) p-polarized reflectivity R_p (b) s-polarized reflectivity R_s Since the *Au* NPy surfaces with $\lambda_g = 200$ nm, a 100 nm-thick layer of spin cast PMMA with a refractive index $n_d \approx 1.5$.

The R_s minimum also occurs at $\theta = 15$ degrees and $n_d \approx 1.5$ corresponds to the normal incidence reflectivity measurements (Figure 5.6, $n_d = 1.5000$). As the incidence angle is increased the reflectivity minimum wavelength blue-shifts. An additional reflectivity R_s dip occurs for $\theta = 75$ degrees at a wavelength near 620 nm. We are currently developing a theoretical model to explain the incidence angle dependent reflectivity behavior, however, it is evident that the local surface plasmon resonance is strongly dependent on the azimuthal angle alignment of excitation

polarization and the *Au* NPy geometry as well the alignment with the incidence angle.

5.6 Conclusion

Using reflectance spectroscopy we have studied the plasmonic coupling behavior of both NG and NPy. The wavelength (or energy) where the minimum reflectivity occurs is considered to be the resonant local surface plasmon wavelength and was found to be very close to the first *Au* inter-band transition with an air dielectric medium. Using dielectric medium with an increased refractive index caused a red-shift in the resonant wavelength and the reflectivity minimum could be clearly resolved. From the measurements presented in this chapter, we conclude that for *Au* NPy surfaces sample orientation, with respect to the excitation source polarization, does not severely affect the plasmonic coupling to the nanogap structures. However, sample orientation of the *Au* NG surfaces is very important in order to facilitate plasmonic coupling since the nanogaps are patterned in one direction (in the case of NPy surface nanogaps exist two directions perpendicular to each other and extend the length of the sample). Understanding the local surface plasmon resonance coupling with the excitation source aids us in the design of the SERS measurements by using an appropriate laser wavelength and dielectric medium in order to achieve the highest and most uniform enhancement factors.

References

1. Yu, Q.M.; Guan, P.; Qin, D.; Golden, G.; Wallace, P.M. *Nano Lett.* 2008, 8, 1923.
2. Ye, J.; Van Dorpe, P.; Van Roy, W.; Lodewijks, K.; De Vlaminck, I.; Maes, G.; Borghs, G.; *J. Phys. Chem. C* 2009, 113, 3110.
3. Hicks, E.M.; Lyandres, O.; Hall, W.P.; Zou, S.L.; Glucksberg, M.R.; VanDuyne, R.P. *J. Phys. Chem. C* 2007, 111, 4116.

4. Zhao, J.; Dieringer, J. A.; Zhang, X.Y.; Schatz, G.C.; VanDuyne, R. P. *J. Phys. Chem. C* 2008, 112, 19302.
5. Takimoto, B.; Nabika, H.; Murakoshi, K. *J. Phys. Chem. C* 2009, 113, 11751.
6. Muniz-Miranda, M.; Gellini, C.; Giorgetti, E. *J. Phys. Chem. C* 2011, 115, 5021.
7. Masson, J.F.; Gibson, K.F.; Provencher-Girard, A. *J. Phys. Chem. C* 2010, 114, 22406.
8. McFarland, A.D.; Young, M. A.; Dieringer, J.A.; VanDuyne, R. P. *J. Phys. Chem. B* 2005, 109, 11279.
9. Haynes, C.L.; Van Duyne, R.P. *J. Phys. Chem. B* 2003, 107, 7426.
10. Shuford, K.L.; Lee, J.; Odom, T.W; Schatz, G.C. *J. Phys. Chem. C* 2008, 114, 6662.
11. Lust, M.; Pucci, A.; Otto, A. *J. Raman Spectrosc.* 2006, 37, 166.
12. Fox, M. *Optical properties of solids* Oxford University Press: 2010.
13. Le Ru, E.C.; Etchegoin, P.G.; Meyer, M. *J. Chem. Phys.* 2006, 125, 204701.
14. Johnson, P.B.; Christy, R.W.; *Phys. Rev. B* 1972, 6, 4370.
15. Maier, S. *Plasmonics Fundamentals and Applications*. 2010: Springer.
16. Sambles, J.R.; Preist, T.W.; Tan, W.-C.; Wanstall, N.P. Chapter 22: Surface plasmons and zero order metal gratings, in *Proc. IUTAM Symp. On Mechanical and Electromagnetic Waves in Structured Media*, R.C. McPhedran et al. (Eds.), 2001, 285.
17. Chen, Z.; Hooper, I.R.; Sambles, J.R. *J. Mod. Optics* 2006,53, 1569.
18. Sobnack, M.B.; Tan, W.C.; Wanstall, N.P.; Preist, T.W.; Sambles, J.R. *Phys. Rev. Lett.* 1998, 80, 5667.
19. Raether, H. *Surface Plasmons on Smooth and Rough Surfaces and on Gratings*, Springer-Verlag, 1986.
20. Deng, X.G.; Braun, G.B.; Liu, S.; Sciortino Jr., P.F.; Koefer, B.; Tombler, T.; Moskovits, M. *Nano Lett.* 2010, 10, 1780.
21. Hooper, I.R.; Sambles, J.R. *Phys. Rev. B* 2002, 65, 165432.
22. Tan, W.C.; Preist, T. W.; Sambles, J. R.; Wanstall, N. P. *Phys. Rev. B* 1999, 59, 12661.
23. Le Ru, E.C.; Etchegoin, P. *Principles of Surface Enhanced Raman Spectroscopy and Related Plasmonic Effects*, Elsevier, 2009.
24. Garcia-Vidal, F.J.; Pendry, J.B. *Phys. Rev. Lett.* 1996, 77, 1163.

Chapter 6

SERS substrate characterization using Raman spectroscopy

The SERS substrates are characterized with Raman spectroscopy using well-known probe molecules to assess the performance of the substrates in terms of the magnitude and spatial uniformity of the non-resonant enhancement factor (*EF*). First, we use the probe molecule rhodamine-6G (R6G) in an aqueous solution and assess the enhancement capability of the substrate by reducing the solution concentration and estimate the number of molecules in single point measurements. The magnitude and spatial uniformity of the *EF* factor of the SERS substrate are assessed using a monolayer of benzene-thiol (BT) chemisorbed directly on the *Au* surface. The EF distribution, and associated mean and standard deviation, are assessed over large surface areas with about 10,000 measured spectra.[5]

[5] Modified from: M. Jin, V.V. Pully, C. Otto, A. van den Berg, E.T. Carlen, High-Density Periodic Arrays of Self-Aligned Subwavelength Nanopyramids for Surface Enhanced Raman Spectroscopy, *J. Phys. Chem. C* 114, 21953, 2010.

6.1 Introduction

Since the discovery of SERS on noble metal surfaces[1-3], a new era for Raman spectroscopy has emerged for molecular identification in aqueous solutions at low sample concentrations, which provides a unique capability for the label-free detection and identification of a variety of different analytes. Since the first SERS report, Raman scattering enhancements spanning several orders of magnitude, compared to normal Raman scattering, down to the single-molecule level have been reported[4-8]. The mechanisms responsible for SERS on metal nanostructured surfaces include electromagnetic field enhancements, molecular resonances and charge-transfer transitions[9]; however, the electromagnetic enhancement is considered the dominant process[10]. The electromagnetic field enhancement is electrodynamically generated when surface plasmons of the metal nanostructures couple with incident excitation photons. Metal nanostructures with sharp points and rod-shaped nano-particles produce locally enhanced electromagnetic fields due to the lightning-rod effect; however, the largest electromagnetic enhancements arise from the plasmon interactions of at least two adjacent nanostructures (dimers) in the form of spatially localized surface plasmon resonances that lead to large electromagnetic field enhancements of the excitation field near the metal surface and enabled the detection of SERS from single molecule[4-8]. The small separation gaps between dimers are typically referred to as SERS *hot-spots* and have motivated the field of hot-spot engineering in an attempt to optimize the SERS figure of merit, which includes large enhancements with high spatial uniformity, dynamic range, and polarization independence.

6.1.1 Enhancement factor figure of merit

The quality of a SERS substrate is essentially related to its enhancement factor (*EF*), which is a measurement to quantify the amplification of inelastically

scattered photons from a molecule of interest in near proximity to a nanostructured metal surface compared to the intensity generated from the same molecule in solution or adsorbed to a non-amplifying surface. The SERS enhancement factor that we consider in this thesis is the non-resonant average *EF*, which is different than the maximum *EF*. In general, the magnitude of the average *EF* is lower than the maximum *EF*[11]. There are some requirements for calculating the SERS *EF*. First, the intensity of the Raman signal from a known number of analyte molecules needs to be determined. While maintaining the measurement environment constant we then determine the Raman intensity from the same number of analytes on the SERS substrate, where it is assumed that all molecules are attached to the substrate surface. Therefore, the average *EF* can be estimated as

$$EF = \frac{I_{SERS}}{I_{RS}} \tag{6.1}$$

where I_{SERS} [photons s^{-1}] is the intensity of the Raman signal from a specific number of analyte molecules on the SERS substrate and I_{RS} [photons s^{-1}] is the intensity of Raman signal from the same number of analyte molecules without the SERS substrate. Unfortunately, it is very difficult to have exactly the same number of analyte molecules for the two measurements. If we assume that every molecule will equally contribute to the intensity of the Raman signal, then the SERS enhancement factor can be estimated as

$$EF = \frac{I_{SERS} / N_{SERS}}{I_{RS} / N_{RS}} \tag{6.2}$$

where N_{SERS} is the number of analyte molecules that contribute to the intensity of Raman signal from the SERS substrate and N_{RS} is the number of analyte molecules

that contribute to the intensity of the Raman signal without the SERS substrate. However, the exact number of molecules that contribute to measured intensities is difficult to obtain and we need to estimate the required parameters. Since the I_{SERS} originates from molecules very near the surface then $N_{SERS} \approx 2D_{SERS}H_{enh}L_{enh}$ where D_{SERS} [molecules nm^{-2}] is the density of the analyte molecules on the surface, $2H_{enh}$ [nm] is the height of the two surfaces in the nanogap enhancement region that contains the attached probe molecules, and L_{enh} [nm] is the length of the enhancement region (dependent on the laser spot size at beam waist). The Raman signal from the solution measurement depends on the characteristics of the optical collection volume and must be estimated separately to determine the number of analyte molecules. Since many SERS measurements are done in aqueous solution, a practical method is to use the concentration of the analyte. In aqueous solution, we assume everywhere the number of molecules is the same and all the molecules in the detection volume contribute equally to the Raman measurement. We define $[C_{RS}]$ as the concentration [molecules nm^{-3}] of the same analyte without the SERS substrate. The number of analyte molecules in the optical detection volume can be estimated as $N_{RS} \approx [C_{RS}]A_S H_{eff}$, where A_S [nm^2] is the beam waist area of the excitation laser source and H_{eff} [nm] is the effective height of the optical detection volume and will be discussed further later in this section. Therefore, the average enhancement factor can be estimated as

$$EF = \frac{I_{SERS}/N_{SERS}}{I_{RS}/N_{RS}} = \frac{I_{SERS}[C_{RS}]A_S H_{eff}}{2I_{RS}D_{SERS}H_{enh}L_{enh}} \tag{6.3}$$

This modified expression is especially effective when self-assembled monolayers of Raman active molecules are chemisorbed onto the *Au* surfaces using a thiol (*-SH*) *Au* reaction and provide a reasonably accurate estimation of the number of surface molecules. The parameters introduced in this section will be estimated in the

characterization methods section of the chapter. It should be noted that the approach used to estimate the number of molecules that contribute to the scattered intensity approximately eliminates the requirement to consider the differences between the excitation laser spot area A_s and the detection area A_d, which depends on the optical path (e.g. fibers and lenses) and spectrometer configuration (e.g. transmission and aperture ratio (f/#)) because we use a ratio of two measurements performed on the same instrument with identical configuration.

6.1.2 Polarization dependence

It is well known that the localized surface plasmon located between adjacent nanostructures is sensitive to the polarization of the excitation signal change, which directly affects the electromagnetic field distribution in the hot-spot regions[12]. Since the magnitude of the electromagnetic field directly affects the SERS enhancement, then optimizing the polarization characteristics of coupling the excitation signal to the localized surface plasmon will also maximize the SERS signal[12]. For many SERS substrates, aligning the excitation polarization with the geometry of the nanostructures is very important to maximize the SERS enhancement. The polarization alignment in this thesis was done by manual rotation of excitation laser beam using a λ/2 manual rotator plate

6.2 Characterization methods

The performance of the new SERS substrates is evaluated by assessing the average non-resonant *EF* using two different types of probe molecules and evaluation methods. In the first method, physically adsorbed R6G molecules in DI water are introduced to the SERS substrate in a small sample volume (10^{-5} L) and allowed to incubate for a fixed amount of time (15 min.). The sample concentration is then

reduced it is no longer possible in a reasonable amount of time to detect the probe molecules. The single-point measurement average *EF* is then estimated using the techniques described in this chapter. In the second method, a chemisorbed monolayer of BT molecules are uniformly chemisorbed to the *Au* surfaces. The BT monolayer covered NPy *Au* surfaces are then measured and large areas (~10^4 μm^2) of the substrate are imaged, which contains 2500 full spectra per measurement image. The *EF* of specific vibration modes are estimated and statistical distributions are estimated using histograms.

6.2.1 Physical adsorption in aqueous environment

Raman spectra of physically adsorbed R6G in aqueous DI water solutions on flat and patterned NPy surfaces coated with *Au* have been measured. Although SERS studies of R6G on *Ag* surfaces have been previously reported[4,6,7,13], we used *Au* surfaces due to its chemical stability. All samples of varying concentrations were diluted from a stock solution of 10^{-2} M R6G (9-[2-(ethoxycarbonylphenyl]-3,6-bis(ethylamino)-2,7-dimethylxanthylium chloride, Aldrich, R4127) that was prepared by dissolving 4.8 mg of R6G in DI water. A 10^{-5} L aliquot of each solution was placed in the center of the NPy surface and immediately covered with a glass slide. Each sample was incubated for 15 minutes at room temperature prior to a measurement. The sample was then placed under the objective of the previously described confocal Raman microscope and horizontal nanogaps were aligned perpendicular to the excitation polarization. Raman measurements were done with both measurement systems using laser sources 632.8 nm, 647.1 nm, and 785 nm. All data were smoothed with an FFT smoothing algorithm with n=3 data points.

6.2.2 Chemisorbed monolayers in dry environment

Raman spectra of chemisorbed BT on flat and patterned NPy surfaces coated with *Au* have been measured in an air environment. The BT monolayers provide a more accurate estimation of the average enhancement factor and have been widely used for characterization of SERS substrates[14-17]. The BT monolayers were prepared by placing clean *Au* (70 nm thickness) coated NPy surfaces into a 4 mM BT ethanol solution over night in order to form a densely packed monolayer on the patterned NPy surface especially in the nanogap regions between adjacent NPy. The substrate was gently rinsed with dehydrated ethanol a few times and dried with pure N_2 gas. Raman spectra of BT were excited with He-Ne laser (632.8 nm) with two different objectives, and two different sets of data were collected with each objective: 100×/NA 0.9 objective with 2mW laser power (measured at the entrance of the microscope objective) and a 20×/NA 0.4 objective with 5 mW laser power. The BT spectra were recorded with measurement system 2. The integration time for all Raman spectra is 100 ms.

6.2.3 Measurement instrumentation

Two confocal Raman microscopy systems have been used for measurements for all measurements presented in this chapter. The first Raman measurement system (measurement system 1) records spectral information from 646 to 849 nm in 1600 pixels on a TE-cooled electron-multiplied charged coupled device (Newton DU-970N, Andor Technology, Belfast, Northern Ireland). A cw krypton ion laser (Coherent, Innova 90K, Santa Clara, CA; λ_o= 647.1 nm) was used as a single excitation source with a power of 135 μW. A Nikon M-Plan 40×/NA 0.4 SLWD bright field objective (WD: 14.9 mm) was used to focus (diffraction limited with approximately 400 nm diameter[18]) the laser on the nanostructured surface at normal incidence and to collect the Raman scattered light from the sample surface.

Measurement system 2 is a confocal Raman measurement system (alpha300R, Witech GmbH) with a NIR UHTS300 spectrometer (f/4 300 mm FL; grating: 600 L mm^{-1}) combined with a TE-cooled electron-multiplied charged coupled device detector (Newton DU970P-BV, Andor Technology, Belfast, Northern Ireland), diode laser (Topica Photonics XTRA single frequency diode laser; 500 mW; λ_o=785 nm), Helium-Neon laser (Research Electro-optics, Model 32413, λ_o=632.8 nm, 35 mW), both connected to a 3 m single-mode fiber, and focusing was done with a Zeiss EC EPiPlan 20×/0.4 NA objective (WD: 3.1 mm), a Nikon CFI Achromat oil immersion 100×/1.25 NA objective (CGC; WD: 0.23 mm) and, Olympus MPLFLN 100×/0.9 NA objective (WD: 1 mm, F.N. 26.5)

6.2.4 Enhancement factor parameter estimation

The estimation of the average *EF* requires the determination of the number of molecules excited for the respective measurement. For the normal Raman measurement I_{RS}, the number of molecules excited and measured with the optical system $N_{RS} \approx [C_{RS}]A_S H_{eff}$ requires the determination of the area of the laser beam waist A_s and the effective height of the optical collection system. The measurement systems used for measurements in this thesis use a confocal detection arrangement. Therefore, H_{eff} is the effective confocal depth using the beam waist as a constant width. We use an empirical method to estimate the effective confocal depth using the same measurement system configuration used for a particular measurement, i.e. objective lens, laser source, polarization. A flat surface of a polished silicon wafer is placed in the path of the laser beam of the measurement system and the intensity of the 521 cm^{-1} Raman line of the silicon sample (Figure 6.1a) is monitored as the silicon sample is moved throughout the confocal volume of the measurement system (Figure 6.1b, inset). In Figure 6.1b, the measured intensity profile is shown as the sample is scanned throughout the confocal volume and each measurement

point represents the magnitude of the 521 cm^{-1} peak using the 20×/NA 0.4 objective of measurement system 2.

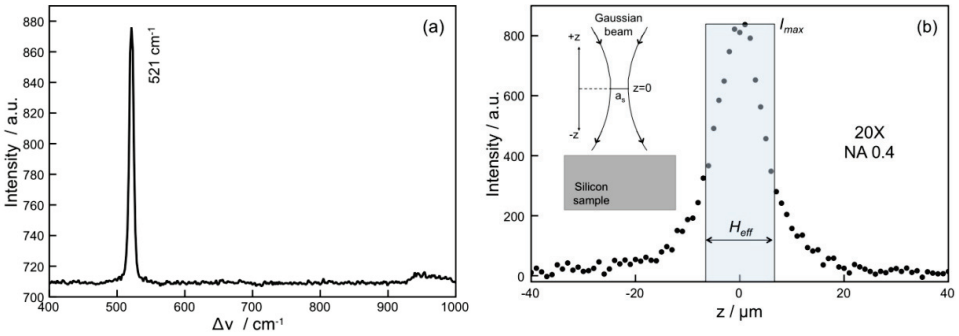

Figure 6.1 Estimation of the effective confocal height H_{eff} of measurement system 2 with a 20×/0.4 NA objective lens. (a) Typical measured spectrum of silicon sample (b) Measured intensity profile as sample is scanned throughout the confocal volume (-40 μm≤z≤40 μm).

From the measured intensity profile as a function of scan height z, the maximum intensity I_{max} represents the measurement at z=0, which is the beam waist. Equating the area under the intensity profile with the area shown in the highlighted region of Figure 6.1b results in the effective confocal height estimation calibrated to the beam waist.

$$I_{\max} H_{eff} = \int_{-\infty}^{+\infty} I(z)\,dz$$
$$H_{eff} = \frac{\int_{-\infty}^{+\infty} I(z)\,dz}{I_{\max}} \tag{6.4}$$

In should be noted that when this method is used to estimate H_{eff} then the measurements used for EF estimation should be done at sample position z=0 where a calibration intensity peak is maximum. For the 20×/0.4 NA objective H_{eff}≈14.8

μm. Similar measurements were performed with other microscope objectives, i.e. a 100×/0.9 NA lens with H_{eff}≈1.9 μm. The estimation of the area of the laser beam waist A_s is done using conventional theory of the Gaussian diffraction limited spot size.

For the SERS measurement the number of molecules on the surface N_{SERS}≈$D_{SERS}H_{enh}L_{enh}$ that produce the measured intensity I_{SERS} requires the estimation of D_{SERS}, H_{enh} and L_{enh}. The molecular surface density of the chemisorbed thiolated molecules on an *Au* surface is based on previous reports, D_{SERS}≈5 molecules nm^{-2} [19]. The estimation of the enhancement height and length requires knowledge of the electromagnetic field in the nanogap, which is a function the surface pitch, depth, geometry and metal dielectric properties. We have used a two-dimensional finite difference time domain (FDTD) numerical solution of Maxwell's equations of the crevice profile using the appropriate dielectric function of the deposited *Au* layer. Figure 6.2 shows examples of numerical simulation results of the electric field distribution in the nanogap between adjacent NPy structures. Figure 6.2a shows the 2D profile of a nanogap that was measured from a typical sample using tapping mode atomic force microscope (AFM) with super sharp tips (average diameter 2 nm). The AFM data was imported into the commercial FDTD solver (Fullwave, RSoft, Inc). The total electric-field magnitude $\left|\vec{E}_{tot}(x,z)\right|$ is shown in Figure 6.2b and the magnitude of the magnetic field $\left|\vec{H}_{y}(x,z)\right|$ is shown in the inset. Figure 6.2c shows high resolution scanning electron microscopy (HR-SEM) images of the metal-coated NPy surfaces. Figure 6.2d shows the distribution of the $\left|\vec{E}_{tot}(x,z)\right|$ as a function of distance z at the center of the nanogap x=0. From Figure 6.2d we estimate the height of the enhancement region H_{enh}≈7 nm for all measured results presented in this thesis. It should be noted that the *Au* deposition method results in surfaces that are relatively rough,

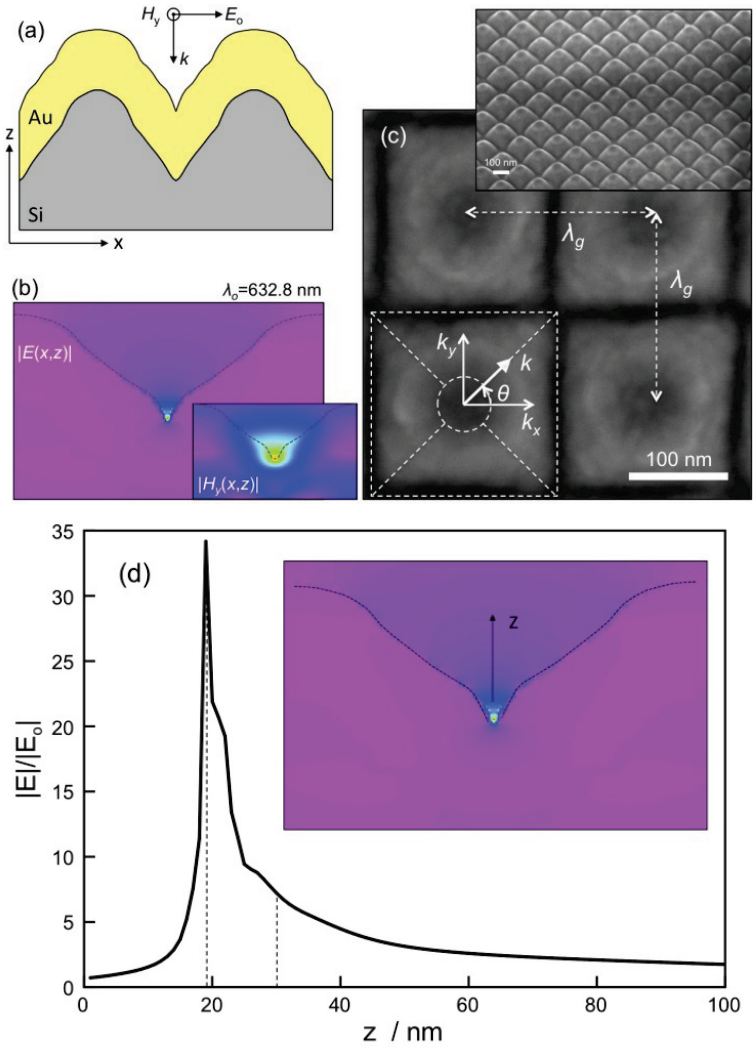

Figure 6.2 NPy gap-plasmon resonators. (a) High-resolution atomic force microscopy NPy cross-section profile converted to 2D simulation model, (b) 2D FDTD simulation results showing the spatial dependence of the total electric field magnitude $\left|\vec{E}_{tot}(x,z)\right|$ and magnetic field magnitude $\left|\vec{H}_y(x,z)\right|$ at the base of the nanogap region, (c) High-resolution scanning electron microscopy image of a section of a NPy surface with λ_g=200 nm, (d) distribution of the $\left|\vec{E}_{tot}(x,z)\right|$ as a function of distance z at the center of the nanogap x=0.

which affects the geometry of the nanogap profile. Therefore, we expect that the electric field profile and magnitude will vary and accordingly will contribute to the overall *EF* spatial variation. The length of the enhancement region L_{enh} depends area of the excitation beam on the surface and the polarization alignment of the laser source and the surface. For all measurements presented in this thesis, the laser source polarization was aligned perpendicular to one of the directions on the NPy surface. For the 20×/0.4 NA objective L_{enh}≈4 μm, and for the 100×/0.9 NA objective L_{enh}≈0.4 μm.

6.3 Results and discussion

The Raman spectrum consists of scattered intensity plotted against frequency shift Δν. Each peak corresponds to a given Raman shift from the incident excitation wavelength. If the molecule is excited to a vibrational state when an incident photon is scattered, the photon may lose energy when scattered, leading to Stokes Raman scattering. The Stokes and anti-Stokes Raman peaks are symmetrically positioned about the Rayleigh peak, but their intensities are very different except for low vibrational energies. We record the Stokes Raman scattered intensity using an optical edge filter. As previously described, the SERS substrates are characterized using two different probe molecules to assess the performance of the substrates in terms in of the magnitude and spatial uniformity of the *EF*. First, R6G in aqueous solution is used to assess the enhancing capability of the substrate by reducing the solution concentration and estimate the number of molecules in single point measurements. In a second set of experiments, the magnitude and spatial uniformity of the *EF* factor of the SERS substrate are assessed using a monolayer of BT chemisorbed directly on the *Au* surface. The *EF* distribution, and associated mean and standard deviation, are assessed over large surface areas with about 10,000 measured spectra over relatively large areas ~10^4 μm^2.

6.3.1 Physically adsorbed R6G measurements

The first characterization studies were conducted with R6G, which is a commonly used molecule for demonstration of the SERS effect and for single molecule studies based on surface enhanced resonant Raman scattering (SERRS). The reason for the ubiquity of R6G for SERS studies is due to its relatively large differential scattering cross-section $d\sigma/d\Omega \sim 10^{-27}$ cm^2/sr,[11] and therefore, results in relatively large signal intensities. One drawback of using R6G, a fluorescent laser dye, is that its optical absorption maximum occurs at about 535 nm, and therefore, the measured signals can contain a combination of inelastically scattered photons and photons due to the excitation of fluorescence of the molecule. Fluorescence is not a scattering process, and fluorescence emission from most liquids and solids does not have vibrational structure. Even weak fluorescence can be much stronger than Raman scattering, easily overwhelming the Raman signal. In order to avoid this situation the laser excitation wavelength is chosen far from the absorption wavelength.

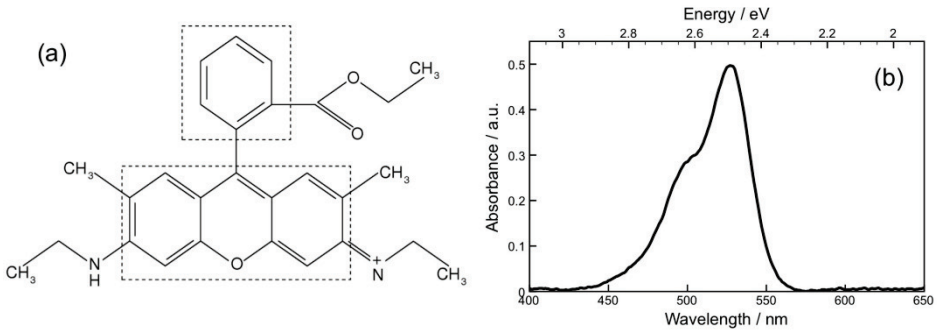

Figure 6.3 R6G molecular details. (a) schematic diagram of the molecular structure showing the xanthene ring in the lower outlined region of the molecule and upper phenyl ring, (b) UV/Vis absorption spectrum.

The drawback to this approach is that excitation with wavelengths toward the near infrared result in lower scattered intensity due the ν^{-4} dependency. Figure 6.3 shows a schematic diagram of R6G and measured UV/Vis spectra from R6G in DI water. The measured absorption spectrum shows a very small amount of absorption for wavelengths above about 600 nm and all measurements of R6G are down with 632.8 nm, 647.1 nm, and 785 nm laser wavelengths.

Figure 6.4 shows representative measurements of 5×10^{-6} M R6G in deionized water on flat (dashed line) and NPy *Au* surfaces (solid line) excited at λ_o=647 nm (measurement setup 1). The lower trace shows the measured sample response from a flat *Au* surface, which consists of the deposited *Au* film on a flat SiO_2/Si surface using identical measurement conditions.

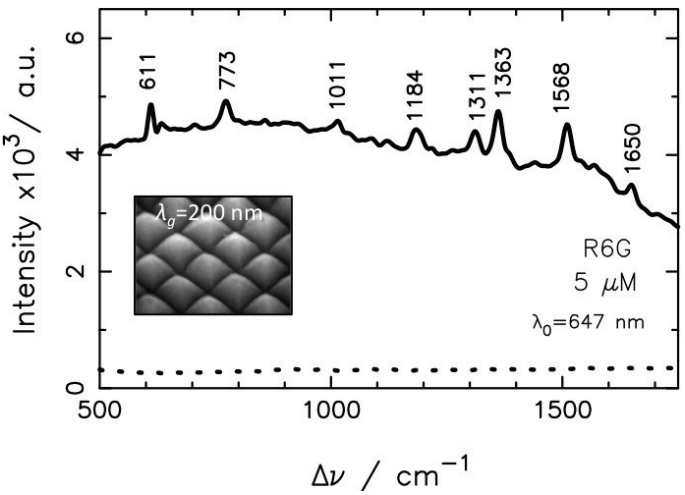

Figure 6.4 Raman measurements of R6G adsorbed on flat (dotted) and NP (solid) surfaces. λ_g=200 nm and solution concentration $[C_{SERS}]=5\times10^{-6}$ M.

The measured spectral characteristics of R6G on the NPy surfaces include 611, 773, 1011, 1184, 1311, 1363, 1568, and 1650 cm^{-1}. The 611, 773, and 1184 cm^{-1} modes are associated with *C–C–C* ring in-plane, out-of-plane bending, and *C–C* stretching vibrations, respectively, and the 1363, 1568, and 1650 cm^{-1} modes are associated

with aromatic *C–C* stretching vibrations,[4] however, the 1650 cm^{-1} mode is reported to have contributions from *C-H* bending modes of the xanthene ring and the 1011 cm^{-1} mode is associated with the phenyl ring and $COOC_2H_5$ side groups.[20] The measured vibrational spectra compare well with previous reports with the exception of the 1011 cm^{-1} mode[4,21]. It should be noted that most previous studies were conducted under surface enhanced resonance Raman conditions with an excitation wavelength near the peak absorption wavelength of R6G (~532 nm). Figure 6.5 shows measured Raman spectra for the 10^{-7} M R6G concentration in DI water, which includes the 934, 1011, 1124, 1266, 1312, 1382, 1525, 1599, and 1636 cm^{-1} modes, where all modes have been previously reported[4,7,21].

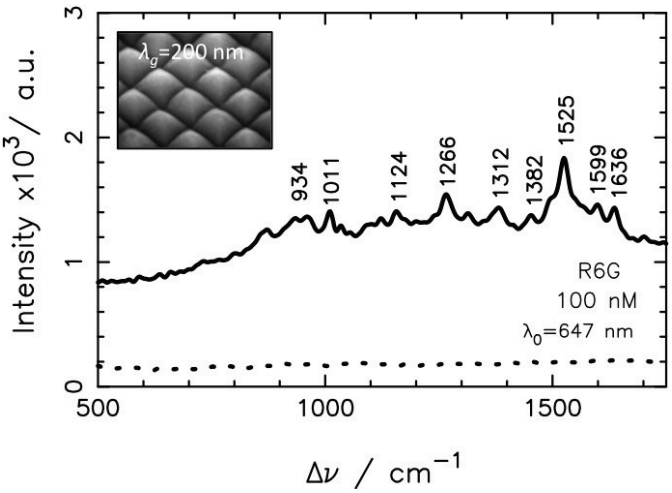

Figure 6.5 Raman measurements of R6G adsorbed on flat (dotted) and NP (solid) surfaces. λ_g=200 nm and solution concentration $[C_{SERS}]=10^{-7}$ M.

The 1011 cm^{-1} and 1525 cm^{-1} modes have not been previously reported; the 1525 cm^{-1} mode has not been previously reported under SERS or resonant SERS conditions and is associated with vibration of the xanthene ring and NHC_2H_5 end groups.[20] The 1636 cm^{-1} mode has not been previously assigned and is likely

related to the 1650 cm^{-1} xanthene ring mode. All measurements are accompanied by a broadband *white* continuum under the Raman lines as previously reported, which has been explained as continuous scattering from the underlying metal[21, 22]; however, the flat metal surfaces do not exhibit this behavior. More recently, a model describing a combination of plasmonic and charge transfer between the molecule and metal surface effects has been reported to explain the well known SERS background.

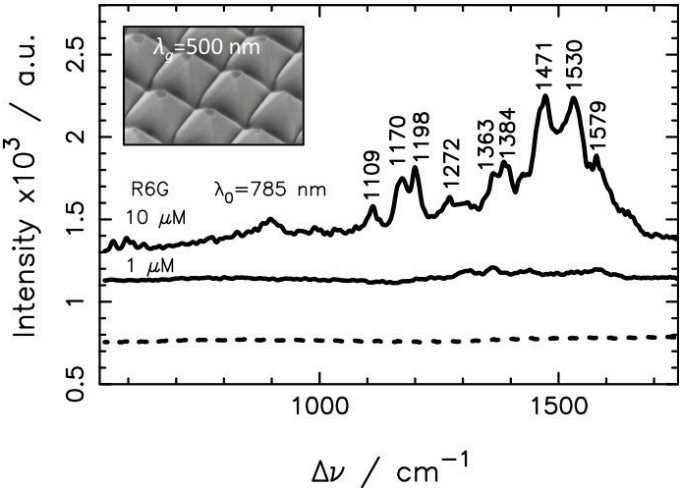

Figure 6.6 Raman measurements of R6G adsorbed on flat (dotted) and NP (solid) surfaces. λ_g=500 nm and solution concentration [C_{SERS}]=10^{-6} M and 10×10^{-6} M. Since R6G adsorbs strongly to glass surfaces, we estimate that half of the available

Since each measurement was performed with a known sample volume, we estimate an upper limit of ~760 R6G molecules adsorbed on the NPy surface in the confocal imaging area, which is estimated by considering that the 10^{-5} L volume of sample spreads over the entire substrate surface (area: 50 mm^2) when covered with the glass slide (25×25 mm^2, Menzel-Glaser), and therefore, the sample approximately conforms to an area of 50 mm^2 and 0.2 mm height. R6G molecules are available to adsorb to the *Au* surface. The 10^{-7} M sample with 10^{-5} L volume results in $0.5\times(10^{-7}$

mol L^{-1})×(10^{-5} L)×(6.02×10^{23} mol^{-1})≈3×10^{11} molecules. As an upper limit estimation of the number of R6G molecules adsorbed on the surface, we assume that all molecules in the half-space adsorb uniformly onto the entire *Au* surface, thus resulting in a surface coverage density of (3×10^{11} molecules)/(50×10^{-6} m^2)≈6×10^{15} molecules m^{-2}. Assuming a circular 400 nm diameter diffraction limited spot size of the confocal microscope results in an upper limit of (1.3×10^{-13} m^2)×(6×10^{15} molecules m^{-2})≈756 molecules in the excitation region, which is reasonable since the lateral dimensions are much larger than the vertical dimension (>20×).

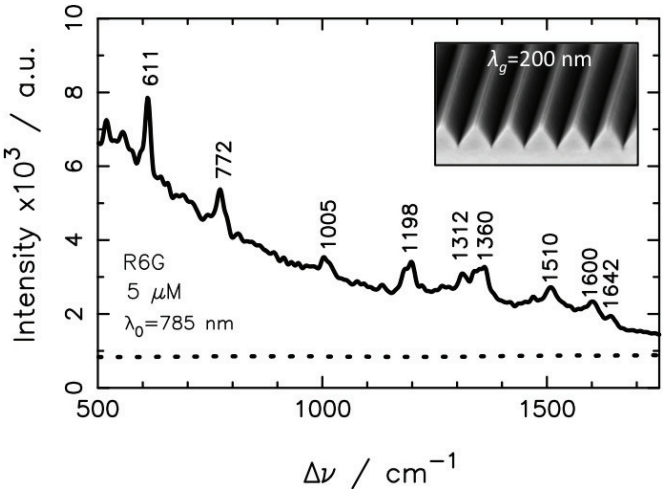

Figure 6.7 Raman measurements of R6G adsorbed on flat (dotted) and NG surfaces with λ_g=200 nm and R6G concentration [C_{SERS}]=5×10^{-6} M.

Considering R6G molecules adsorbed only in the polarization direction of the hot-spot regions results in an upper limit of about 24 molecules in the excitation region. It should be noted that the electromagnetic enhancement occurs only for the field polarization perpendicular to the length of the cavity, and therefore, a much smaller region of the total excitation region provides the large electromagnetic enhancement, and therefore, the measured response is due to a small number of

molecules. A more precise assessment of the number of molecules represented in the 10^{-7} M measurement (Figure 6.5) is not possible with the current measurement system since the exact location of the active region of the crevice is not known, however, the measured spectra of the 10^{-7} M R6G concentration is associated with just a few R6G molecules in DI water. Figure 6.6 shows R6G spectra from a NPy surface with λ_g=500 nm and excitation λ_o=785 nm (experimental setup number two). The 500 nm pitch NPy arrays have lower enhancements at the excitation wavelengths used here as evidenced by the requirement for larger R6G concentrations (10^{-5} M), which is consistent with previous reports[23]. Figure 6.7 shows measured R6G spectra from a nanogroove array (and flat *Au* surface) at λ_o=785 nm. Although the background spectrum is different, nine of the major R6G modes are shown, which demonstrates Raman activity of the nanogroove surfaces with similar measured intensities.

For low sample concentrations (<10^{-6} M) the measurements are consistent with the population averaging effect.[4, 24] For R6G sample concentrations ranging from 10^{-6} M to 10^{-4} M (not all data shown), the measured spectra are very consistent and repeatable with respect to location and time. The enhancement factor has been estimated by comparing the peak heights of vibration spectra on the NPy array surfaces with peak heights from reference measurements in solution while maintaining the same laser power, optical microscope system, spectrometer configuration, and R6G sample. A larger R6G concentration is used for the normal Raman reference measurement. The resulting areal average enhancement factor was estimated in equation 6.2. Due to the pre-resonance activity of R6G and low required laser power, enhancement factors at all measured vibration modes was not possible, however, an average EF~10^6 has been measured for the $\Delta\nu$=1310 cm^{-1} mode and we consider this to be a lower bound for the Raman scattering enhancement.

6.3.2 Chemisorbed BT measurements

Further studies of the SERS substrates have been conducted by attaching a monolayer of BT to the *Au* surface. Benzene and its derivatives, such as pyridine and pyrazine, are popular Raman probe molecules as they have reasonably large differential scattering cross-sections $d\sigma/d\Omega \sim 10^{-29}$ cm^2/sr[25], well-characterized and relatively small number of Raman active modes. Figure 6.8 shows some details of BT that are relevant for the use as a probe molecule to characterize the SERS substrates.

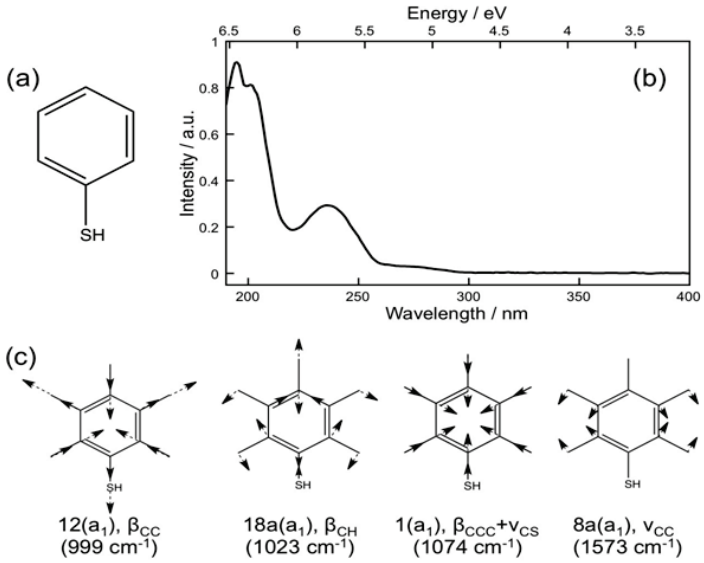

Figure 6.8 BT molecular details. (a) schematic diagram of molecular structure (b) UV/Vis absorption spectrum (c) dominant Raman vibration modes.

There is no optical absorption above about 300 nm for BT in a DI water solution, and therefore, offers good optical properties to evaluate the SERS substrate figure of merit. The dominant vibration modes of the BT chemisorbed on a *Au* surface are shown in Figure 6.8c. There are two interesting aspects that we use to evaluate the performance of the SERS substrate using a single monolayer of BT molecules. The first is the enhancement factor and the second is the excitation polarization

dependence. In the previous section, we have introduced the enhancement factor calculation method and introduced the average enhancement factor calculated by using R6G solutions as the characterization molecule. In this section, the substrate is covered with a monolayer of BT molecules, which enables the estimation of the average enhancement factor more precisely than physical adsorption from a low concentration of molecules.

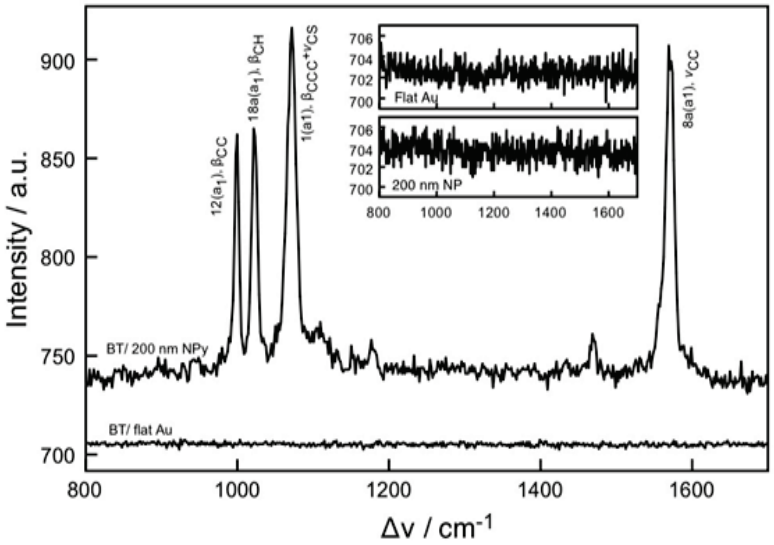

Figure 6.9 Measure spectra of chemisorbed BT on 200 nm pitch NPy surface.

It is also interesting to know the uniformity of the substrate by measuring the SERS of BT monolayer molecules and combined with Raman spatial imaging. The surface coverage characteristics and uniformity of the enhancement factors of the measured Raman spectra have been evaluated on *Au* NPy surfaces using BT monolayers. For these measurements the ambient medium is air. In Figure 6.9, a representative Raman spectrum is shown with the different vibrational mode of BT molecules. Every vibration mode is directly related to BT and has been reported[19]. Note that the 917 cm^{-1} vibration mode, associated with the *S-H* bond, that occurs

for BT in free solution does not appear in the chemisorbed BT to *Au* and is a good indicator of the monolayer formation[19,25]. The measured spectrum of BT on a flat *Au* layer is also shown in Figure 6.9, and does not contain any detectable vibration peaks. The measured spectrum of clean NPy and flat *Au* coated surface are shown in the inset of the Figure 6.9, which show no vibrational information and establishes the background noise floor of the measurement. Also note that the broad

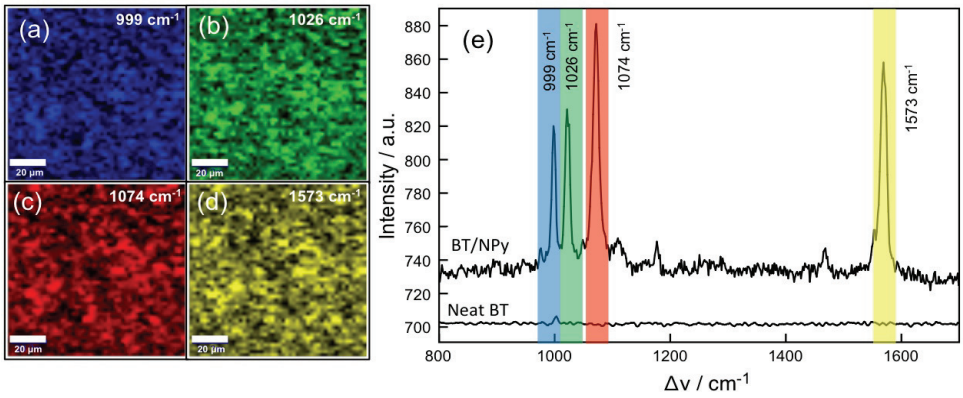

Figure 6.10 Raman scan of the 200 nm NPy substrate and Raman spectra used to mapping the substrate surface. (a)-(d) show the Raman map of different vibration mode of BT (998 cm^{-1}, 1022 cm^{-1}, 1076 cm^{-1} and 1575 cm^{-1}). (e) BT SERS spectra. The excitation wavelength is 633 nm and a 20×/0.4 NA objective lens was used. Raman spectra of BT from neat material and on the NPy substrate. The excitation laser is 632.8 nm with a 100 ms integration time and 5 mW laser power measured at the entrance of the objective.

background signal is not present in the BT chemisorbed to the flat *Au* surface (Figure 6.9) or the neat BT solution (Figure 6.10) measurements.

Figures 6.10a-d show the Raman image maps of different vibrational modes (999 cm^{-1}, 1026 cm^{-1}, 1074 cm^{-1} and 1573 cm^{-1}) of BT chemisorbed on *Au* consisting of 2500 full spectra over an area of 10^4 μm^2. The 999 cm^{-1} mode is due

to the *C-H* waging mode. The 1025 cm^{-1} is from the *C-C* symmetric stretch. 1074 cm^{-1} mode indicates the *C-C* asymmetric stretch and is strongly affected by the C-S bond. The last strong peak is the 1573 cm^{-1} mode, which represents the *C-C* symmetric stretch[19]. From these Raman image maps, we can see the high spatial uniformity of the NPy substrate covered with a monolayer of BT. The measurements were performed on measurement system 2 with a 20×/0.4 NA objective lens, 632.8 nm excitation laser (5 mW power measured at the entrance of the objective) and 100 ms integration time. Figure 6.10e shows a representative SERS spectrum of a monolayer of BT on the *Au* NPy surface (upper spectra) and from a thin layer of neat BT solution (lower spectra). The SERS average *EF* is estimated, as described previously, with $EF=I_{SERS}N_{NEAT}/I_{NEAT}N_{SERS}$, where I_{NEAT} and I_{SERS} represent the intensity of the conventional Raman signal from the neat bulk solution and the SERS signal from the NPy surface, respectively, and N_{NEAT} and N_{SERS} represent the molecular density (molecules m^{-2}) of BT molecules contributing to I_{NEAT} and I_{SERS}, respectively. The BT density is 1.077 g ml^{-1}, and the density of the monolayer on the *Au* surface is 0.544 nM cm^{-2}.[25]

The 2500 measured spectra were then further processed to assess the spatial distribution of the average *EF* on the surface. The 1073 cm^{-1} and 1575 cm^{-1} modes have been studied as they provided the most stable signal across the SERS substrate. The 2500 spectra were filtered by choosing only the spectra that contained a detectable peak at the two vibration frequencies. The criteria for a spectra is based on determining a threshold intensity at the two vibration locations and evaluating if there is sufficient activity that is considered a vibration peak $I_{SERS}>I_t$, where $I_t=\mu+4\sigma$, μ is the baseline background noise signal and σ is the standard deviation of the Gaussian distributed background noise signal over a frequency range near the vibration mode of interest. When $I_{SERS}>I_t$, then the spectra is processed and the *EF* is estimated. Figure 6.11 shows histograms of the

estimated *EF* for the two vibration modes. Both distributions can be modeled with a lognormal[6] distribution. For the $\Delta\upsilon$=1073 cm^{-1} mode, 80% of the spectra were retained with $EF=(0.64\pm0.32)\times10^6$ and maximum EF=0.6×10^7, and the $\Delta\upsilon$=1573 cm^{-1} mode, 60% of the spectra were retained with $EF=(0.58\pm0.33)\times10^6$ and maximum $EF=0.4\times10^7$. For these measurements we did not detect any damage to the BT monolayer, in the form of a broad peak near the 1500 cm^{-1} region of the spectrum, during imaging and subsequent data processing.

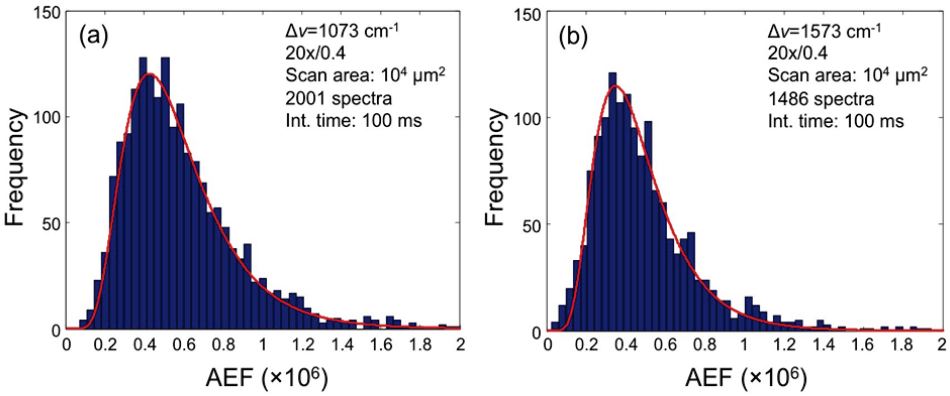

Figure 6.11 Spatial distribution of the average *EF* of λ_g=200 nm NPy surfaces using 20x/0.4 objective imaged over a 10^4 μm^2 area.

Similar measurements were done with a higher magnification and NA objective (100×/0.9 NA), which reduces the excitation laser spot and subsequently the number of molecules measured for each of the 2500 measurements. Figure 6.12a shows representative Raman spectra from the BT monolayer attached to the *Au* NPy surface (upper spectra) and a thin neat solution of BT (lower spectra). Figure 6.12b shows the *EF* distribution of 2500 measured spectra imaged over an area of

[6] In a lognormal distribution, the mean μ and standard deviation σ are calculated from the estimated expectation $E[X]=exp(\mu+\sigma^2/2)$ and variance $V[X]=(exp(\sigma^2)-1)exp(2\mu+\sigma^2)$, and subsequently $\mu=ln(E[X])-0.5ln(1+V[X]E[X]^{-2})$ and $\sigma^2=ln(1+V[X]E[X]^{-2})$, respectively.

1600 μm^2. The EF distribution also follows a lognormal distribution with EF =(0.13±0.12)×10^7 with a maximum EF=0.5×10^8.

Similar Raman measurements of BT monolayers on *Au* NPy surfaces with larger pitch λ_g=500 nm and 100×/0.9 NA objective lens. Based on reflectance measurements shown in Chapter 5, where the local surface plasmon resonance was significantly red-shifted in the water dielectric medium, which better matches with the 632.8 nm He-Ne laser source and higher average enhancements are expected. Following the formation of the BT monolayers on the *Au* NPy substrate, a 10^{-5} L volume of DI water was placed on the substrate and sandwiched with a glass slide and imaged with an oil immersion objective, similarly as was done in the R6G solution measurements.

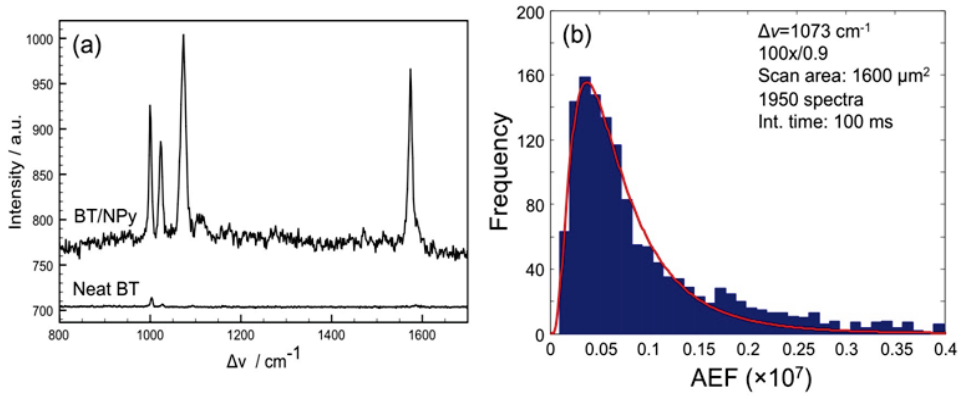

Figure 6.12 Spatial distribution of the average EF of λ_g=200 nm NPy surfaces using 100x/0.9 objective imaged over a 1600 μm^2 area.

Figure 6.13 shows the EF distributions of 2500 measured spectra (for each measurement) imaged over an area of 10^4 μm^2 using λ_g=500 nm pitch *Au* NPy surfaces in air (Figure 6.13a) and in water (Figure 6.13b). Both EF distributions follow a lognormal distribution with 83% area coverage and EF =(0.46±0.01)×10^6 with a maximum EF=0.13×10^7 for the air measurement. The water measurements

show 99.9% area coverage and $EF=(0.32\pm0.01)\times10^7$ with a maximum $EF>10^8$. These results show that the average *EF* distribution increased 2-3 times, which is due to the local surface plasmon resonance that is better matched to the laser excitation source. The 500 nm pitch *Au* NPy structures yielded measurable spectra from 99.9% of the 2500 measurements with a standard deviation that is 10× less than the 200 nm pitch structures.

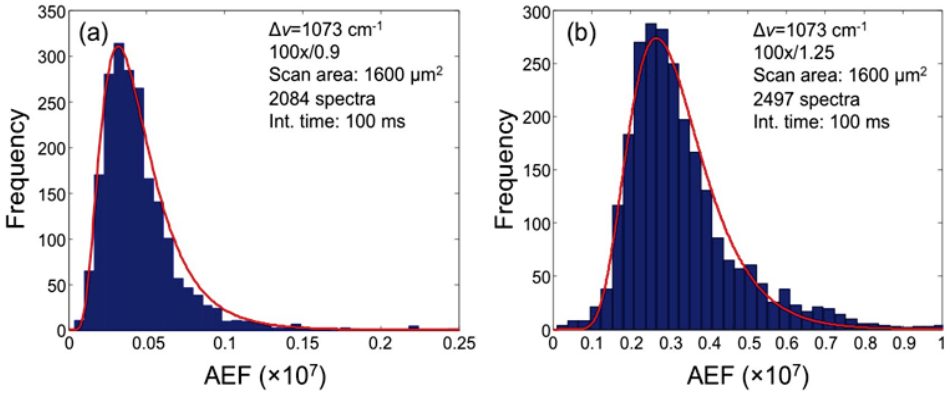

Figure 6.13 Spatial distribution of the average *EF* of λ_g=500 nm NPy surfaces imaged over a 10^4 μm^2 area. (a) air measurement using 100×/0.9 NA objective (b) water measurement using 100x/1.25 NA oil immersion objective.

The *Au* NPy (λ_g=500 nm) surfaces are now compared to commercially available inverted pyramidal pit array SERS substrates (Klarite 302, Renishaw Diagnostics, Ltd.). A BT monolayer was chemisorbed on each substrate surface using the previously described preparation method. Figure 6.14 shows the measurement results of the Klarite 302 substrates with chemisorbed BT. The Klarite 302 substrate (Figure 6.14a) with chemisorbed BT was measured in air using a He-Ne laser (λ_o=632.8 nm) with 2 mW power measured at the entrance of the microscope objective. A 100x/0.9 NA objective was used to record 10^4 spectra over an area of 1600 μm^2 (Figure 6.14b). An example BT spectrum from the Klarite substrates is

shown in Figure 6.14c. The image shown in Figure 6.14b represents the measured CCD counts over the spectral range from 1060 cm^{-1} to 1090 cm^{-1}. Finally, Figure 6.14d shows a histogram of the integrated CCD count distribution.

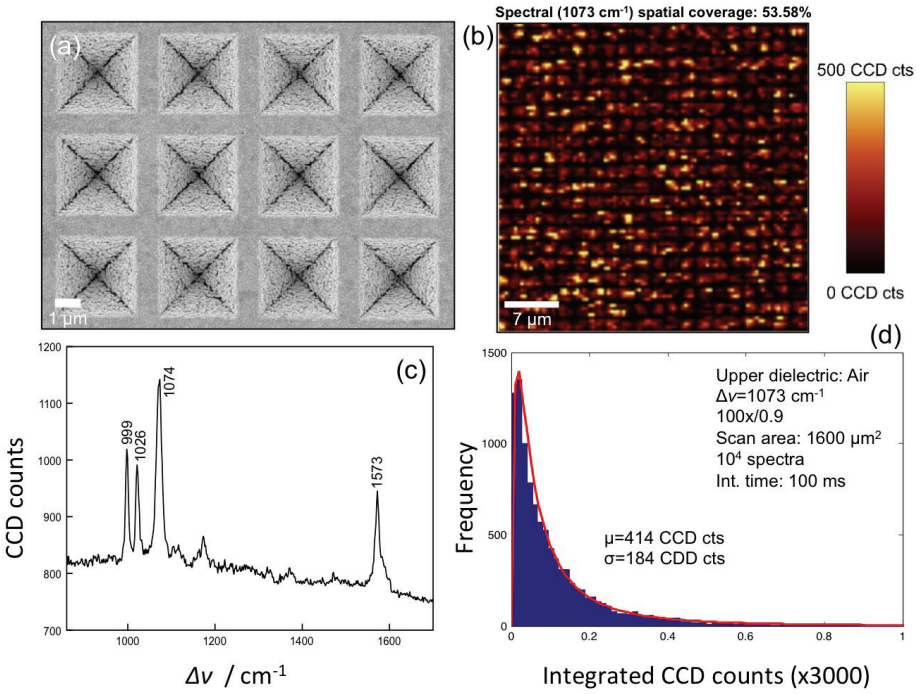

Figure 6.14 Klarite 302 SERS substrate measurements. (a) Scanning electron microscopy image (b) Spatial image (40×40 µm^2) from Raman measurement of integrated CCD counts of 1073 cm^{-1} vibrational mode of BT from 10^4 spectra (c) Example spectrum of the chemisorbed BT (d) Histogram of integrated CCD counts.

Figure 6.15 shows the measurement results of the *Au* NPy substrates with chemisorbed BT. The *Au* NPy substrates (Figure 6.15a) with chemisorbed BT was measured in Di water using a He-Ne laser (λ_o=632.8 nm) with 2 mW power measured at the entrance of the microscope objective. A 100x/1.25 NA objective was used to record 10^4 spectra over an area of 1600 µm^2 (Figure 6.15b). An example BT spectrum from the *Au* NPy substrates is shown in Figure 6.15c. The image shown in Figure 6.15b represents the measured CCD counts over the

spectral range from 1060 cm^{-1} to 1090 cm^{-1}. Figure 6.15d shows a histogram of the integrated CCD count distribution.

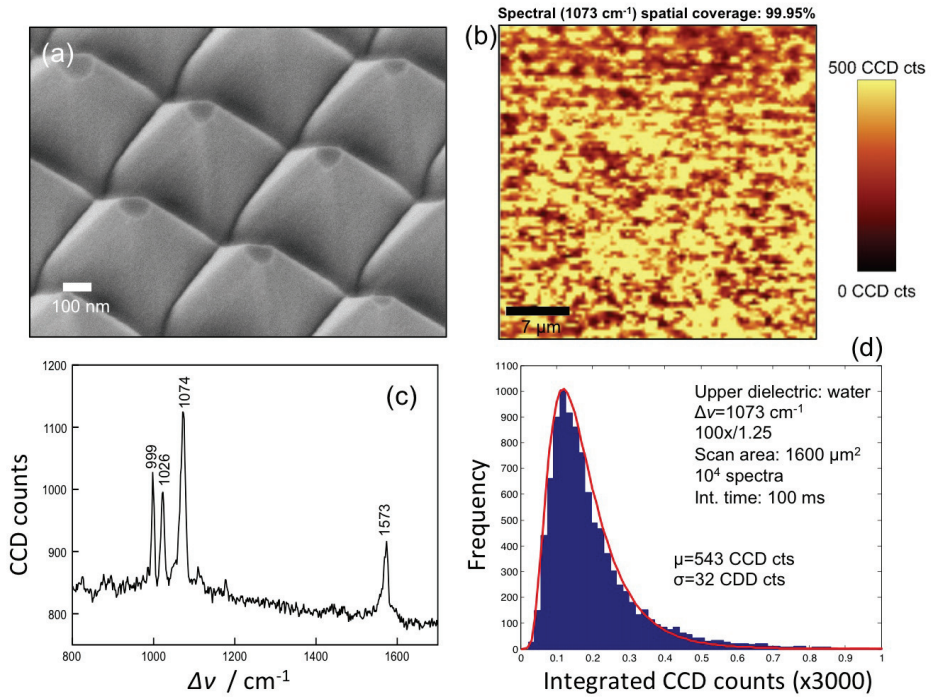

Figure 6.15 *Au* NPy (λ_g=500 nm) substrate measurements. (a) Scanning electron microscopy image (b) Spatial image (40×40 µm^2) from Raman measurement of integrated CCD counts of 1073 cm^{-1} vibrational mode of BT from 10^4 spectra (c) Example spectrum of the chemisorbed BT (d) Histogram of integrated CCD counts.

From the measurements shown in Figure 6.14 and Figure 6.15, the Klarite 302 substrate has a mean of μ=414 CCD counts and standard deviation σ=184 CCD counts. The *Au* NPy substrates has a mean μ=543 CCD counts and standard deviation σ=32 CCD counts. The *Au* NPy substrates have a higher average CCD count with lower variance and a much greater maximum CCD count for the measurement conditions. The most striking difference between the two substrates is the Raman surface coverage, which is defined as the percentage of the surface

that produces a SERS effect. The *Au* NPy substrate produced a 99.95% surface coverage compared to 53.58% surface coverage of the Klarite 302 substrate.

6.4 Polarization effect

As was previously discussed, the generation of the localized surface plasmon located between adjacent nanostructures is sensitive to the polarization of the excitation signal change, which can directly affect the electromagnetic field in the hot-spot regions, and can affect the SERS enhancement. This phenomenon is well known for asymmetrical structures, such as metal rods and dimer nanoparticle pairs, as was described in Chapter 3. We have measured the polarization dependency of the *Au* NPy surfaces by monitoring the peak intensity of the four dominant Raman peaks of BT chemisorbed on the *Au* NPy surfaces as the excitation polarization alignment with the *Au* NPy surface is changed from 0 degrees (horizontal alignment) to 180 degrees (vertical alignment), in increments of the 15 degrees, by manual rotation of polarization using a $\lambda/2$ rotator plate. As illustrated in Figure 6.16, as the laser polarization is rotated $0 \leq \theta \leq 180$ degrees the measured intensities vary from maximum at 0 degrees to maximum at 90 degrees and then back to maximum at 180 degrees. The measured intensities are minimum at θ=45 degrees and θ=135 degrees. We attribute this polarization dependence to the generation of the surface plasmon polariton by scattering from the *Au* NPy surfaces (Figure 6.2c). For θ=0 degrees and 180 degrees then the vertical cavity is responsible for the local surface plasmon resonance (generated by k_x) and for θ=90 degrees the horizontal cavity is responsible (generated by k_y). For θ=45 degrees and 135 degrees then the scattering is shared between the cavities and the overall enhancement is lower. More research is required to determine the exact cause of this dependency. The dashed-line plots shown in the upper graph of Figure 6.16 show that the intensity

measurement of the system 2 varies a very small amount as the λ/2 rotator plate is rotated $0 \leq \theta \leq 180$ degrees in increments of 15 degrees and the measured polarization dependence is due to the *Au* NPy surface geometry.

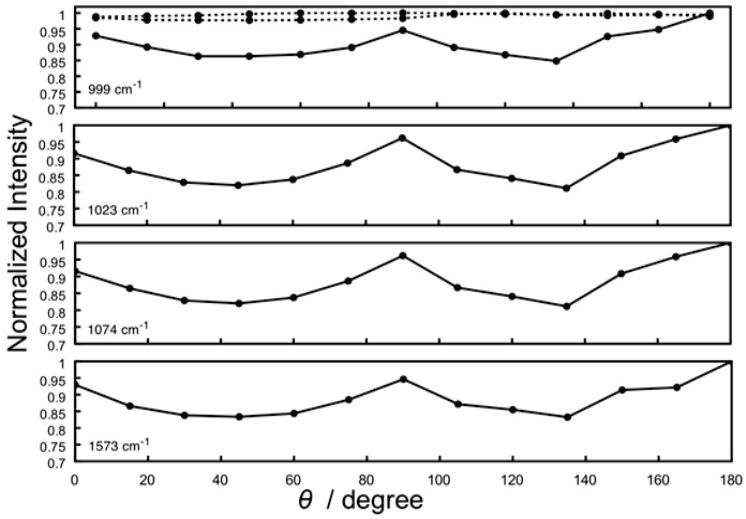

Figure 6.16 Raman intensity dependence on the excitation polarization alignment to the *Au* NPy (λ_g=200 nm) substrate. All spectra measured with 632.8 nm He-Ne laser (2 mW measured at the objective entrance), and 100 ms integration time. The dashed lines in the upper graph plot the polarization variation from the instrument.

Figure 6.17 shows similar measurements using a 500 nm pitch *Au* NPy substrate where the intensity of the four dominant vibrational modes are monitored as the laser excitation polarization alignment with the substrate is rotated $0 \leq \theta \leq 180$ degrees in increments of 15 degrees. Interestingly, the 500 nm pitch *Au* NPy surface does not show a strong polarization dependence. All of the monitored intensities remain approximately constant (within the variation of the instrument) as the polarization is rotated. It is clear that the only difference between the two

samples is the pitch of the NPy structures. It has been recently reported that the enhancement mechanism of inverted pyramid structures, with dimensions in the μm-scale, is due to diffraction and not only from a local surface plasmon resonance effect.[26] This could be an explanation for the results presented here. Further investigation is required to resolve these interesting phenomena.

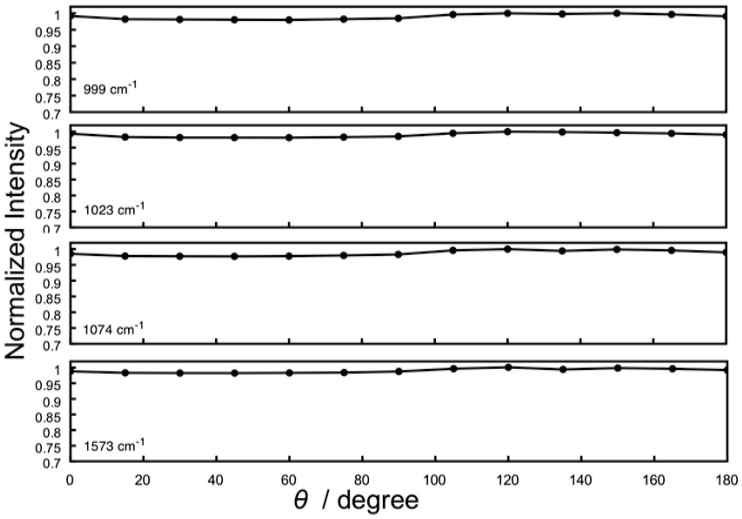

Figure 6.17 Raman intensity dependence on the excitation polarization alignment to the *Au* NPy (λ_g=500 nm) substrate. All spectra measured with 632.8 nm He-Ne laser (2 mW measured at the objective entrance), and 100 ms integration time. The dashed lines in the upper graph plot the polarization variation from the instrument.

6.5 Conclusion

In summary, varying pitch NPy and NG surfaces were characterized in different environments and using different probe molecules, such as R6G in DI water solution, BT in both air and DI water environments. The average *EF* was ~10^6 averaged over 2500 spectra (using BT) and the maximum EF~10^8. Polarization effects have been studied by monitoring the peak intensity of the four dominant

vibration peaks of BT and it has been shown that small pitch (λ_g=200 nm) NPy surface are polarization dependent with intensity reductions about 80% for alignment angles θ=45 degrees and θ=135 degrees, which suggest that both the horizontal and vertical grooves are excited. The larger pitch (λ_g=500 nm) *Au* NPy surfaces do not show polarization dependence. The results presented here are encouraging for the future application of the new *Au* NPy surfaces for analytical applications of surface adsorbed molecular identification.

References

1. Fleischmann, M.; Hendra, P.J.; McQuillan, A.J. *Chem. Phys. Lett.* 1974, *26*, 163.
2. Jeanmaire, D.L.; VanDuyne, R.P. *J. Electroanal. Chem.* 1977, 84, 1.
3. Moskovits, M. *J. Chem. Phys.* 1978, 69, 4159.
4. Hildebrandt, P.; Stockburger, M. *J. Phys. Chem.* 1984, 88, 5935.
5. Kneipp, K.; Wang, Y.; Kneipp, H.; Perelman, L.T.; Itzkan, I.; Dasari, R.; Feld, M. S. *Phys. Rev. Lett.* 1997, 78, 1667.
6. Nie, S.M.; Emory, S.R. *Science* 1997, 275, 1102.
7. Michaels, A.M.; Nirmal, M.; Brus, L. E. *J. Am. Chem. Soc.* 1999, 121, 9932.
8. Dieringer, J.A.; Wustholz, K.L.; Masiello, D.J.; Camden, J.P.; Kleinman, S.L.; Schatz, G.C.; Van Duyne, R.P. *J. Am. Chem. Soc.* 2009, 131, 849.
9. Otto, A. *Top. in Appl. Phys.* 1984, 54, 289.
10. Moskovits, M. *J. Raman Spectrosc.* 2005, 36, 485.
11. Le Ru, E.C.; Blackie, E.; Meyer, M.; Etchegoin, P.G. *J. Phys. Chem. C* 2007, 111, 13794.
12. Li, W.Y.; Camargo, P.H.C.; Lu, X.M.; Xia, Y.N. *Nano Lett.* 2009, 9, 485.
13. Haes, A.J.; Chang, L.; Klein, W.L.;VanDuyne, R.P. *J. Am. Chem. Soc.* 2005, 127, 2264.
14. Smythe, E.J.; Dickey, M.D.; Bao, J.M.; Whitesides, G.M.; Capasso, F. *Nano Lett.* 2009, 9, 1132.
15. Kim, Z.H.; Park, W.H. *Nano Lett.* 2010, 10, 4040.
16. Kim, N.H.; Lee, S.J.; Moskovits, M. *Nano Lett.* 2010, 10, 4181.
17. Fang, Y.; Seong, N.H.; Dlott, D.D. *Science* 2008, 321, 388.
18. Jin, M.L.; Pully, V.; Otto, C.; Van den Berg, A.; Carlen, E.T. *J. Phys. Chem. C* 2010, 114, 21953.

19. Caldwell, J.D.; Glembocki, O.; Bezares, F.J.; Bassim, N.D.; Rendell, R.W.; Feygelson, M.; Ukaegbu, M.; Kasica, R.; Shirey, L.; Hosten, C. *ACS Nano* 2011, 5, 4046.
20. Watanabe, H.; Hayazawa, N.; Inouye, Y.; Kawata, S. *J. Phys. Chem. B* 2005, 109, 5012.
21. Michaels, A.M.; Jiang, J.; Brus, L. *J. Phys. Chem. B* 2000, 104, 11965.
22. Jiang, J.; Bosnick, K.; Maillard, M.; Brus, L. *J. Phys. Chem. B* 2003, 107, 9964.
23. Garcia-Vidal, F.J.; Pendry, J.B. *Phys. Rev. Lett.* 1996, *77*, 1163.
24. Baranska, M.; Podsiadly, R.; Klodowski, J.; Proniewicz, L.M.; Duda, A.; Kozlowski, H.; Sanchez-Cortes, S.; Garcia-Ramos, J.V. *Spectroscopy of Biological Molecules: Modern. Trends.* 1997, 409.
25. Aggarwal, R.L.; Farrar, L.W.; Diebold, E.D.; Polla, D.L. *J. Raman Spectrosc.* 2009, 40, 1331.
26. Vernon, K.C.; Davis, T.J.; Scholes, F.H.; Gomez, D.E.; Lau, D. *J. Raman Spectrosc.* 2010, 41, 1106.

Chapter 7

Towards non-resonant single molecule SERS

An introduction to single molecule (SM) Raman spectroscopy using surface enhanced Raman scattering/spectroscopy (SERS) is described and the importance of extending the single molecule measurements to non-resonant molecules is discussed. The bi-analyte analysis method is described phenomenologically as a tool to validate single molecule measurements as an alternative to ultra-low concentration measurements only. Although these measurements are ongoing, the most current results using 22,500 measured spectra from mixtures of pyridine (Py) and pyrazine (Pz) as a bi-analyte pair on *Au* nanopyramid (NPy) surface with λ_g=200 nm pitch and λ_o=632.8 nm excitation laser are presented.

7.1 Single molecule SERS

The measurement of a single molecule is a common dream among chemists and widely pursued in the analytical chemistry field. With the development of highly sensitive electron multiplying charge coupled device imagers, avalanche photodiodes, and photomultiplier tubes, the measurement of single fluorophores has become more common place over the past 20 years[1-3]. However, single molecule fluorescent spectroscopy requires the chemical attachment (labeling) of the fluorophore to the analyte of interest. Label-free single molecule detection is now being widely pursued using a variety of approaches and techniques[3-5]. Raman spectroscopy is a label-free detection method that provides information about the chemical bonds of a molecule and can be used for molecular identification. However, conventional Raman spectroscopy suffers from very weak scattered intensities, typically ~10^{-6} photons s^{-1} $molecule^{-1}$, and in many cases cannot be used due the extremely small signals, which rendered Raman spectroscopy impractical for many applications and impossible to measure inelastic scattering from a single molecule since its discovery 100 years ago.

However, following the discovery of SERS, single molecule (SM) SERS was demonstrated about fifteen years ago by two separate groups Nie, *et al.*[6] and Kneipp, *et al.*[7]. Nie demonstrated the SM measurement rhodamine 6G (R6G; $C_{28}H_{31}N_2O_3Cl$) physically adsorbed on *Ag* nanoparticle colloid clusters with an excitation laser wavelength near the resonance absorption wavelength of R6G. Interestingly, thirteen years earlier Hildebrandt and Stockburger[8] demonstrated the measurement of R6G Raman spectra from ultra-low concentration samples, which can also be considered a demonstration of SM SERS detection. Kneipp demonstrated the SM SERS measurement of a crystal-violet molecule ($C_{25}H_{30}ClN_3$). These reports were a breakthrough in the SERS field and since that time many more SM SERS measurements have been reported[9-14], which is not a

comprehensive citation list. Up to now, researchers have tried to explore the SM SERS effect by using all kinds of substrates manufactured with different methods. Currently, the majority of the SM SERS measurements have exploited the surface enhanced resonance Raman scattering (SERRS) where the resonance contribution to the enhancement factor is increased several orders of magnitude compared to non-resonant SERS enhancement factors[15]. In SM SERRS, *Ag* nanoparticle colloid solutions or plated aggregated *Ag* nanoparticles on the flat surface have been used for the SM SERS detection[6, 7, 16]. The SM SERRS has provided a significant amount of new information about the Raman scattering processes such as[17] laser power effects[18] and integration time effects.[19]

After more than 10 years of SM SERS research, SM SERS has not been widely adopted by the research community due to limitations in the following areas: *i.* Lack of complete knowledge of the SM SERS processes (which includes resonant and non-resonant Raman enhancement factors), *ii.* Materials, *iii.* Analysis procedures, *iv.* Difficulty in proving a SM SERS measurement using conventional methods. Very recently, a few non-resonant SM SERS detections have been reported for non-resonant molecules, such as adenine[16, 19-21]. The non-resonant SM SERS field is more challenging and interesting because the Raman scattering cross-section at non-resonant wavelengths is significantly smaller than the resonant-based SM SERS measurements, which simply means that better SERS substrates are required to enhance Raman scattered signal. Most of the current SM SERS studies have to scan a huge number of spectra and followed by extensive post-processing analysis. This is not only due to the inhomogeneous distribution of single molecule on the particle surface, but also due to the large variation of the SERS hot-spot geometry and dimensions. In order to overcome these problems, researchers carefully isolate and localize a single molecule into the hot-spot and then find it back afterwards using a SERS measurement[22-24]. This approach is

useful for demonstrating the ability to measure SM SERS signals. However, it is not an ideal detection approach. This method is very similar to conventional SM fluorescence spectroscopy; however, SM fluorescence spectroscopy requires labeling of the fluorophore and does not have the capability to provide a unique vibrational 'fingerprint' of the molecule.

A very important analytical method was introduced about five years ago called the bi-analyte SM SERS technique[9]. Using this approach, two analyte molecules, A and B, with very similar Raman vibrational spectra (not exact) are mixed in varying ratios and concentrations, and are incubated on the SERS surface. Raman spectra are recorded as the analyte concentrations are reduced until no signals can be detected. The Raman spectra are analyzed and spectra containing single events of A, single events of B and events containing spectra from both analytes A and B are counted. For high concentrations of A and B, then single events will occur much less often then the mixed A+B events. As the analyte concentrations are reduced the number of single events increases and the number of mixed events decreases. In general, this method can be performed with higher analyte concentrations compared to the conventional SM SERS measurements, which requires concentrations $<10^{-10}$ M. This method shows statistically the occurrence of single molecule events and reduces the problems associated with ultra-low concentration solutions and estimating the number of adsorbed molecules. This method appears to improve the problem of inhomogeneous molecule distribution. The most popular SM SERS substrate is *Ag* or *Au* nanoparticle aggregations. The inhomogeneous distribution of hot-spots can be solved by using high-density periodic arrays of nanostructures that can be aligned with the excitation laser polarization, or better yet does not have a polarization dependence. Because only this type of substrate can provide a uniformly patterned surface, which make data processing and analysis easier after collecting a Raman image of the surface, since

the surface has uniform hot-spots that are the same, which can minimize fluctuation of the Raman signals based on the hot-spot inhomogeneity. In conclusion, the SM SERS is a very challenging field with many problems. Among these problems, the most important are the detection method and a *good* SERS substrate. The bi-analyte method is convenient for the measurement and simple for data process. This method is drawing more and more attention to SM SERS.

7.2 Bi-analyte analysis

7.2.1 Introduction to bi-analyte analysis

The bi-analyte SM SERS method, first introduced by Le Ru *et al.*[19], is a contrast analysis method that provides a statistical evaluation of vibrational events of one molecule against the background of another. The big advantage of this method is the SM events can be detected at 'higher' concentrations, compared to conventional SM SERS methods that typically reduce concentration ~10^{-10} M [6] to ensure a small number of molecules in the measurement volume. The working strategy of the bi-analyte method is that a mixture of two analytes, A and B, are randomly placed on the SERS substrate in the vicinity of the Raman enhancement hot-spots. With varying the analyte concentrations, the probability of detecting a single analyte will increase as the analyte concentration is reduced while the probability of detecting both analyte molecules decreases. In the data processing step, specific vibration peaks are monitored, which can effectively differentiate between analyte A and analyte B. The collection of a large data set enables a more rigorous validation of SM SERS events. Some experiments have been reported using R6G and Nile blue (NB) under resonance excitation measurement conditions[18, 19]. Since the Raman cross section of these two analytes is quite different results were not conclusive. Most recently, the d_4 labeled isotope of

crystal violet was studied using the bi-analyte analysis method[27]. Both of these measurements were performed under resonance conditions. As previously described, SM SERS measurements of non-resonant molecules is very challenging and an important step forward if this technique is to gain wider acceptance as a single molecule detection technique since the laser excitation source does not have to match the molecule of interest but is rather tuned the resonance behavior of the SERS substrate. Some SM SERS of non-resonant molecules have been reported using the bi-analyte analysis technique. Blackie et. al [13] reported SM SERS using the non-resonant bi-analyte pair: 1,2-di-(4-pyridyl)-ethylene and benzotriazole derivative, which have a similar Raman scattering cross-section. The N^{15} labeled adenine isotope combined with normal adenine as a bi-analyte pair was also tested with poor results, since the Raman scattering cross-section is small very low and below the enhancement factor provided by the SERS substrate[13].

7.2.2 Bi-analyte pair selection

Before we applied the bi-analyte SERS measurement, there are some key factors that must be considered[28]. The first one is the type of bi-analyte pair to be measured. The ideal requirements for the two analytes are that they have similar Raman scattering cross-sections while having at least one distinct vibration peak that can be used for discriminative counting. In earlier measurements, such as R6G and NB, the Raman scattering cross-sections of the analytes was very different[19, 29]. Isotopically edited bi-analyte pairs is a very promising approach and is being used by several research groups since molecular structure between the two analytes is unchanged with the exception of one, or more, of the end groups. However, in most cases, the isotopic molecule did not show an obviously unique Raman spectra compared with the unedited molecule since only *H* atoms have been replaced with deuterium atoms. These measurements require a high resolution grating that can

resolve the small vibration mode differences between these two almost identical molecules.

7.2.3 Bi-analyte experimental methods

We first explore the use of pyridine (Py) and pyrazine (Pz) as a bi-analyte pair. Benzene derivatives, Py and Pz, are chosen because they are very similar from the Raman spectroscopy point of view because they have similar molecular structures, approximately similar scattering cross-sections[19], and based on our investigations can be easily differentiated spectroscopically in the Raman shift range 800 $cm^{-1} \leq \Delta\nu \leq 1400$ cm^{-1}. The measurements were performed in an aqueous environment. The *Au* NPy substrate was first fixed on a glass cover slide and then 10^{-5} L of bi-analyte solution was deposited on the *Au* NPy surface. Another thin glass cover slide was gently placed above the aliquoted sample and mounted in the measurement system. Raman spectra of Py and Pz were recorded with a confocal Raman microscope (alpha300R, Witech GmbH). A Helium-Neon laser (Research Electro-optics, Model 32413, λ_o=632.8 nm) with 2mW power (calibrated at the entrance of the focusing objective) was focused onto the *Au* NPy surface with a Nikon CFI Achromat oil immersion 100×/1.25 NA objective (CGC; WD: 0.23 mm). An integration time of 100 ms was used for all measurements. In total, 22,500 Raman spectra were recorded over a scan area of 2025 μm^2. Since Pz and Pd molecules have similar structure, their Raman shifts are similar, and therefore, a high resolution grating spectrometer (f/4 300 mm FL; grating: 1800 lines mm^{-1}, NIR UHTS300, WiTech, GmbH) is required to resolve spectral peaks with similar resonance frequencies.

7.3 Results: Pyridine and pyrazine

The Py (partner A) and Pz (partner B) molecules have similar molecular structure with a difference in only one atom different where the C atom at the para-position of *N* in pyridine is replaced by an additional *N* atom in Pz molecule (Figure 7.1, inset). Figure 7.1 shows the UV-Vis absorption spectrum of Py and Pz, which shows that the resonant optical absorption is well below 400 nm in both cases.

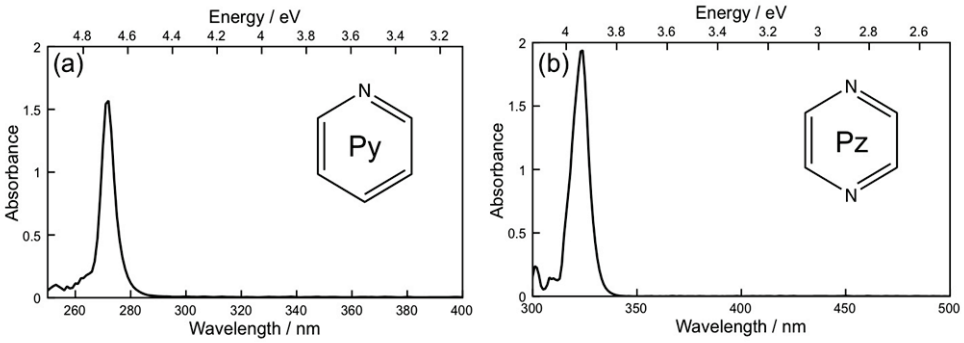

Figure 7.1 Absorption (UV-Vis) spectra of (a) Py and (b) Pz used for the non-resonant SM SERS measurements.

The addition of the *N* atom in the Py molecule results in a Raman spectrum that allows the Py molecule to be distinguished from the Pz molecule. Figure 7.2 shows representative measured Raman spectra from Py (Figure 7.2a) and Pz (Figure 7.2b) physically adsorbed on a *Au* NPy surface. The ring-stretching mode (1216 cm^{-1}) of the *C* and *N* atoms at the para-positions of the Pz molecule is used to discriminate the Py and Pz from the bi-analyte analysis procedure. If Py is randomly absorbed on the *Au* surface, 1216 cm^{-1} mode is weak and rarely encountered even in high concentration[30]. However, if an electrical potential was applied to the *Au* surface, which has been reported to align the Py molecular orientation on the *Au* surface

with *N* atom bonding with *Au* atom the 1216 cm^{-1} mode can be strongly enhanced[25,26,31,32]. By using the Raman shift at 1216 cm^{-1}, we can determine how many measurement events belong to A, B or A+B. Three Raman peaks are evident from Py (1010 cm^{-1}, 1036 cm^{-1}, 1545 cm^{-1}) and shown in Figure 7.2a. The 1000 cm^{-1} mode represents a ring-breathing mode (ν_1), 1036 cm^{-1} is the ring stretching vibration mode (ν_{12}), and 1545 cm^{-1} is a ring vibration mode. We have observed the 1216 cm^{-1} mode of Py from less than 1% of the measurements for the high concentration (10 mM) evaluation measurement, and we expect the occurrence of the 1216 cm^{-1} mode of Py to further decrease. Three Raman spectra of Pz are shown in Figure 7.2b where 1010 cm^{-1} is a ring breathing mode and 1600 cm^{-1} is a ring-stretching mode. The very strong band at 1216 cm^{-1} is from ring stretching between the two *N* atoms. This mode is a very stable mode and does not appear to be affected by the adsorption orientation. For this reason, we chose this mode for single molecule event counting. The measurement was performed at different concentrations of a Py and Pz mixture solution.

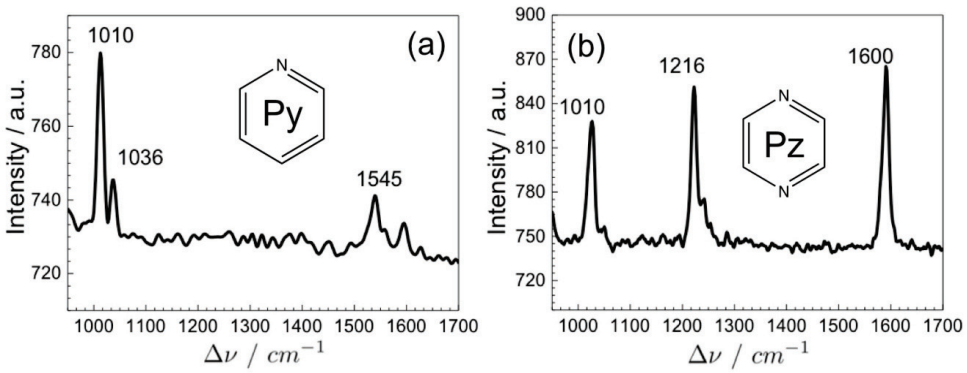

Figure 7.2 Raman spectra of Py and Pz (each 10 mM) physically adsorbed on the *Au* NPy surfaces.

The Py and Pz molecules were mixed in a 50:50 ratio and three different concentration solutions were measured: 10^{-7} M, 10^{-9} M and 0.5×10^{-9} M. For each sample concentration, an area of 2025 μm^2 was scanned and Raman spectra collected for each measurement resulting in a total of 22,500 measured spectra. An algorithm was developed to filter the measured data and retain only the spectra that contained suitable vibrational spectra. In the first phase, the 1010 cm^{-1} ring-breathing mode was used to collect all usable spectra since this mode is strong and stable in both molecules. For each spectrum, the signal 800 $cm^{-1} \leq \Delta\nu \leq 950$ cm^{-1} was extracted. It was found that the background signal followed a Gaussian distribution and a mean μ and standard deviation σ variance were calculated over the specified range.

The measured intensity I_{SERS}^{m} over the frequency region from 1005 cm^{-1} to 1015 cm^{-1} was compared to a threshold value of $I_t = \mu + 4\sigma$. If $I_{SERS}^{m} > I_t$, then the spectrum is retained for further analysis. The retained spectra were then analyzed using a similar technique to determine if a measurable peak in the frequency range 1210 $cm^{-1} \leq \Delta\nu \leq 1220$ cm^{-1} was present. If the spectrum contains a peak in this specified range then the 1036 cm^{-1} mode region is searched using a similar procedure. If the 1216 cm^{-1} and 1036 cm^{-1} modes occur then the spectrum is counted as mixed event (A+B). If the 1216 cm^{-1} is present and not the 1036 cm^{-1} mode then the spectrum is counted as a Pz only (B) measurement. If the 1216 cm^{-1} is not present and the 1036 cm^{-1} mode is present then the spectrum is counted as a Py only (A) measurement. Figure 7.3 shows representative measurements for each analysis condition. Representative measured spectra of single Py and Pz events from a mixture solution (10^{-9} M) are shown in Figures 7.3a and 7.3b. The spectrum from a mixed event measurement is shown in Figure 7.3c. By using this method, we performed a statistical analysis to count the number of molecules for each

analyte concentration. We applied different concentrations (0.5×10^{-9} M, 10^{-9} M, and 10^{-7} M) of Py and Pz mixtures. With higher analyte concentrations, the number of single analyte events decreased dramatically. The histogram from the counting

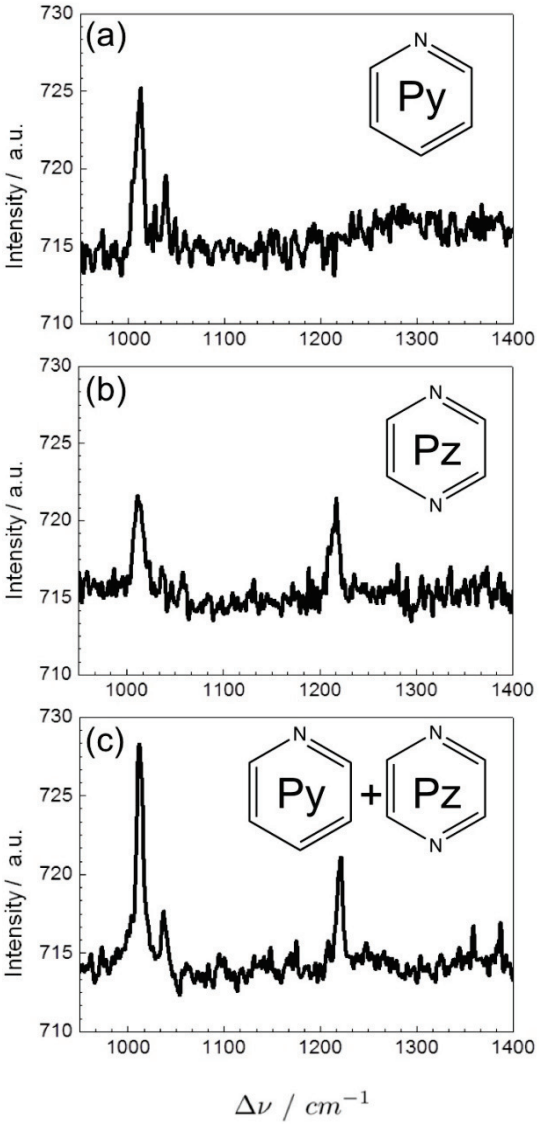

Figure 7.3 Raman spectra from Py and Pz mixture solution. The concentration of Py and Pz are both 10^{-9} M.

analysis is shown in Figure 7.4, which indicates that we are approaching a non-resonant SM SERS measurement. Figure 7.4a shows the results from $[C_{A+B}]=0.5\times10^{-9}$ M concentration solution. With such low concentrations, we clearly see that the single analyte events (A and B) occur more often than the mixed event (A+B). With increased analyte concentrations $[C_{A+B}]=10^{-9}$ M and $[C_{A+B}]=10^{-7}$ M show that the single analyte events decrease dramatically compared with lower concentration. The number of analyte A (Py) events is higher than analyte B (Pz), which can be explained by the scattering properties of the molecules. Although the molecules have the similar structure, the Raman scattering cross-section of Py is higher than Pz[33, 34].

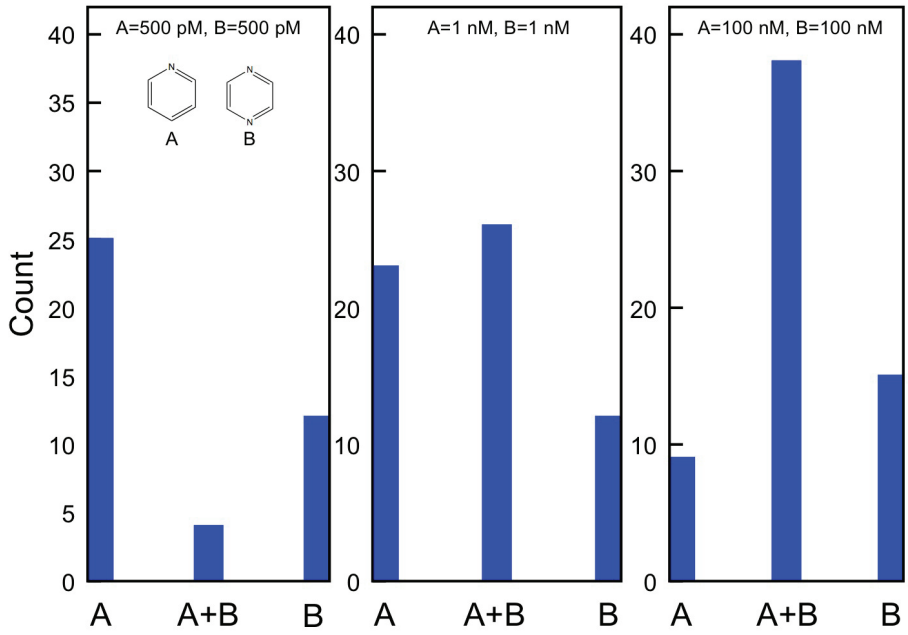

Figure 7.4 Histograms from counting analysis of Py-Pz mixture solutions at concentrations ranges 0.5×10^{-9} M$\leq[C_{A+B}]\leq10^{-7}$ M.

In order to have identical molecules for single molecules detection, the adenine and isotope adenine will be good candidates for bi-analyte SM SERS[13]. We are currently working to improve these results and measuring adenine and N^{15} adenine.

7.4 Conclusion

In this chapter, the *Au* NPy surfaces have been applied to a SM SERS experiment using Py (analyte A) and Pz (analyte B) as a bi-analyte pair. The total concentration of analyte mixtures (50:50) were varied from 10^{-7} M to 0.5×10^{-9} M. A total of 22,500 Raman spectra were recorded for each analyte mixture over an area of 45×45 μm^2 for each analyte concentration. An algorithm was developed to differentiate the spectra containing only analyte A, only analyte B and both analytes A+B and to count each spectrum that passed a minimum intensity threshold. We have shown that for analyte concentrations of 10^{-7} M the majority of the measurements were from both analytes A+B, and for the lowest concentration 0.5×10^{-9} M, the majority of the measurements events occurred from single analytes A and B. These preliminary results show the general trends associated with the bi-analyte analyte as SM SERS behavior. The difference of Raman cross-section of Py and Pz caused some problems with the final results. The only way to over come this drawback is using a molecule and its isotope to form a better bi-analytes system. The adenine and N^{15} isotope adenine are currently being studied.

References

1. Xie, X.S.; Dunn, R.C. *Science* 1994, 265, 361.
2. Weiss, S. *Science* 1999, 283, 1676.
3. Zhuang, X.W.; Bartley, L.E.; Babcock, H.P.; Russell, R.; Ha, T.J.; Herschlag, D.; Chu, S. *Science* 2000, 288, 2048.
4. Kneipp, K.; Kneipp, H. *Appl. Spectrosc.* 2006, 60, 322.

5. Zhang, W.H.; Yeo, B.S.; Schmid, T.; Zenobi, R. *J. Phys. Chem. C* 2007, 111, 1733.
6. Nie, S.M.; Emory, S.R. *Science* 1997, 275, 1102.
7. Kneipp, K.; Wang, Y.; Kneipp, H.; Perelman, L.T.; Itzkan, I.; Dasari, R.; Feld, M.S. *Phys. Rev. Lett.* 1997, 78, 1667.
8. Hildebrandt, P.; Stockburger, M. *J. Phys. Chem.* 1984, 88, 5935.
9. Michaels, A.M.; Jiang, J.; Brus, L. *J. Phys. Chem. B* 2000, 104, 11965.
10. Goulet, P.J.G.; Aroca, R.F. *Anal. Chem.* 2007, 79, 2728.
11. Blackie, E.; Le Ru, E.C.; Meyer, M.; Timmer, M.; Burkett, B.; Northcote, P.; Etchegoin, P.G. *Phys. Chem. Chem. Phys.* 2008, 10, 4147.
12. Fang, Y.; Seong, N.H.; Dlott, D.D. *Science* 2008, 321, 388.
13. Blackie, E.J.; Le Ru, E.C.; Etchegoin, P.G. *J. Am. Chem. Soc.* 2009, 131, 14466.
14. Kleinman, S.L.; Ringe, E.; Valley, N.; Wustholz, K.L.; Phillips, E.; Scheidt, K.A.; Schatz, G.C.; VanDuyne, R.P. *J. Am. Chem. Soc.* 2011, 133, 4115.
15. Le Ru, E.C.; Blackie, E.; Meyer, M.; Etchegoin, P.G. *J. Phys. Chem. C* 2007, 111, 13794.
16. Futamata, M. *Faraday. Discuss.* 2006, 132, 45.
17. Maher, R.C.; Dalley, M.; Le Ru, E.C.; Cohen, L.F.; Etchegoin, P.G.; Hartigan, H.; Brown, R.J.C.; Milton, M.J.T. *J. Chem. Phys.* 2004, 121, 8901.
18. Etchegoin, P.G.; Lacharmoise, P.D.; Le Ru, E.C. *Anal. Chem.* 2009, 81, 682.
19. Le Ru, E.C.; Etchegoin, P.G.; Meyer, M. *J. Chem. Phys.* 2006, 125, 204701.
20. Zhao, K.; Xu, H.X.; Gu, B.H.; Zhang, Z.Y. *J. Chem. Phys.* 2006, 125, 081102.
21. Zhang, Z.L.; Yin, Y.F.; Jiang, J.W.; Mo, Y.J. *J. Mol. Struct.* 2009, 920, 297.
22. Moskovits, M.; Tay, L.L.; Yang, J.; Haslett, T. *Optical Properties of Nanostructured Random Media* 2002, 82, 215.
23. Futamata, M.; Yamaguchi, Y.; Maruyama, Y.; Ishikawa, M. *J. Korean. Phys. Soc.* 2005, 47, 256.
24. Bizzarri, A.R.; Cannistraro, S. *Phys. Chem. Chem. Phys.* 2007, 9, 5315.
25. Brolo, A.G.; Irish, D.E.; Lipkowski, J. *J. Phys. Chem. B* 1997, 101, 3906.
26. Iannelli, A.; Brolo, A.G.; Irish, D.E.; Lipkowski, J. *Can. J. Chem.* 1997, 75, 1694.
27. Dieringer, J.A.; Wustholz, K.L.; Masiello, D.J.; Camden, J.P.; Kleinman, S. L.; Schatz, G.C.; VanDuyne, R.P. *J. Am. Chem. Soc.* 2009, 131, 849.
28. Pieczonka, N.P.W.; Aroca, R.F. *Chem. Soc. Rev.* 2008, 37, 946.
29. Etchegoin, P.G.; Meyer, M.; Le Ru, E.C. *Phys. Chem. Chem. Phys.* 2007, 9, 3006.
30. Wang, C.H.; Sun, D.C.; Xia, X.H. *Nanotechnology* 2006, 17, 651.
31. Aikens, C.M.; Schatz, G.C. *J. Phys. Chem. A* 2006, 110, 13317.

32. Zhao, X.H.; Liu, S.S.; Li, Y.Z.; Chen, M.D. *Spectrochim. Acta A* 2010, 75, 794.
33. Udagawa, M.; Chou, C.C.; Hemminger, J.C.; Ushioda, S. *Phys. Rev. B* 1981, 23, 6843.
34. Zhao, L.L.; Jensen, L.; Schatz, G.C. *Nano Lett.* 2006, 6, 1229.

Chapter 8

Conclusions and recommendations

8.1 Conclusions

In this thesis we introduced surface enhanced Raman scattering/spectroscopy (SERS) and its dependence and relation to plasmonics and introduced the basic requirements for making a *good* SERS substrate. We presented a new SERS substrate based on high density and periodic arrays of nanopyramids (NPy) and nanogrooves (NG). Electron-beam lithography was first used to demonstrate the feasibility over small surface areas (10×10 μm^2) using the anisotropic etching property of single crystalline silicon to form highly uniform 2 nm nanogaps using lithographic patterns with dimensions of 100 nm. The concept was then scaled up to larger surface areas using laser interference lithography (large scale pattern) where an entire 100 mm diameter silicon wafer can be patterned in a single lithography step (maskless) and two etching steps. After the anisotropic etching highly uniform and large are NPy and NG surface were presented. We have realized NPy surfaces with pitch dimensions in range: 150 nm$\leq\lambda_g\leq$500 nm. The silicon NPy and NG surfaces are coated with a thin *Au* layer (~70 nm) for local surface plasmon resonance generation and to form the SERS substrate. At the

intersection between two adjacent *Au* NPy or *Au* NG structure is a nanogap that forms a standing wave gap-plasmon resonance at the *Au*/dielectric interface with the proper laser excitation wavelength.

Reflection spectroscopy is used to investigate the optical properties of the subwavelength *Au* NPy and NG surfaces as a function of the p-polarized white light excitation source. The *Au* NPy and NG surface with different pitches 150 nm$\leq\lambda_g\leq$500 nm have been studied. The local surface plasmon resonance wavelength is red-shifted and the refractive index in increased in the range: $1.3\leq n_d\leq 1.7$ Since the local plasmon resonance of the *Au* NPy surfaces in air was near 500 nm, which is very near to the first *Au* inter-band transition, increasing the refractive index resulted in a clear local surface plasmon resonance the strongly red-shifted in wavelength with increasing n_d, as has been demonstrated with *Au* nanoparticle assemblies. Using these optical characterizations, we tune the laser wavelength to match the *Au* NPy and NG surfaces. By using well know SERS characterization molecules (benzene-thiol and rhodamine 6G), we characterized the SERS properties of the *Au* NPy and *Au* NG surfaces. A similar SERS average enhancement factor was obtained ($\sim 10^6$) with 100% surface overage. The maximum enhancement factor is $0.5\text{x}10^8$. The SERS measurement is highly dependent on the incident light polarization. The NPy's substrate was also applied the SERS measurement with tuned light polarization. The measurement results showed that the *Au* NPy surface is weakly polarization dependent. Finally, we presented preliminary results from a bi-analyte single molecule SERS study using pyridine and pyrazine as a bi-analyte pair. We can clearly see the potential for single molecule SERS detection that is a dream for any curious chemist. And even better, it is label free single molecule detection. Combined with the SERS enhancement factor measurement, we conclude that the *Au* NPy SERS substrates

represent a highly uniform and stable platform, which can greatly enhance the Raman signal and easy to use.

8.2 Recommendations

The most important issue of SERS is to evaluate whether the SERS substrate is good or not. By now, there is no standard method to do this work since all the characterizations used different analytes, different working conditions (laser, integration time, objective lens, etc.), and different measurement environments (dry or aqueous). A standard method for characterization of SERS will greatly help researchers in this field to better characterize their SERS substrates. I believe that this is one of the most important issues for SERS. As it is well known that Raman spectroscopy is a very useful tool for molecular identification, especially since it can be applied to an aqueous environment, which makes it highly attractive for biological applications. However, it suffers that the Raman signal of the target is too weak to see the Raman signal. The viability of biological cells will be challenging with high laser powers, which can partially solve the problem of the weak Raman signal. The safe and efficient way to solve the problem is with the use of SERS. By applying exploiting metal nanostructures, the Raman signal can be easily enhanced $>10^6$.

There are a few fields that can directly benefit from SERS. The first is organic chemistry. In fact, Raman spectroscopy is already an important tool for the organic chemist. The second area is micro total analysis systems (μ-TAS) and sometimes referred to as lab-on-a-chip systems. The minimized detection technique is required. With general Raman spectroscopy, the analyte concentration will not be sufficient to give proper Raman signal. But with SERS, this is not a problem. By using simple fabrication techniques, SERS substrates can easily be integrated in a design

and positioned as a detector. The third area, biological application is getting more popular nowadays.

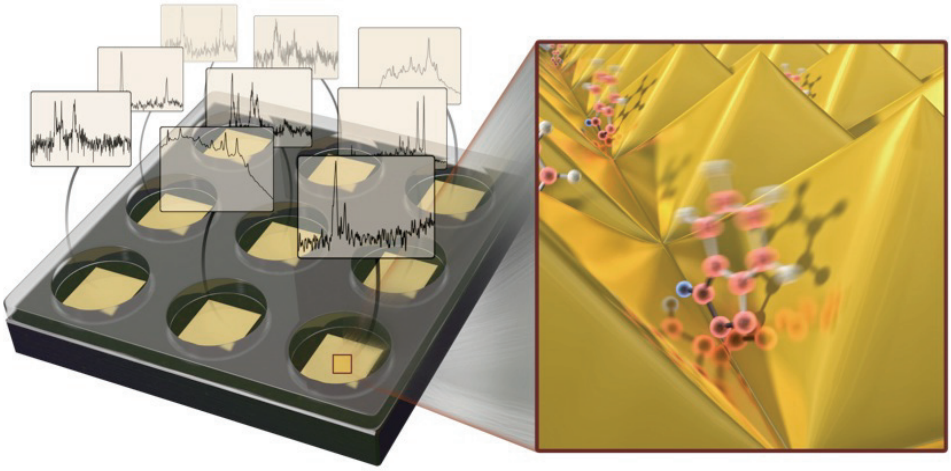

Figure 8.1 SERS microarray platform for drug screening and identification.

SERS could really help this area with its label free and molecular identification properties. However, proper data analysis and processing will most likely be even more import than acquiring signal itself since there are too many data to analysis after enhancing the Raman signal in a cell. This problem is also the real challenging part for SERS. The Raman database and computational calculation method might be great helpful. These will be very useful in the drugscreening direction. In Figure 8.1, we show the concept of SERS microarray platform for this type of application.

Acknowledgements

After the 4-year journey, it is time to have a rest and look back. After I obtained my master degree from medical science and electronic materials, I entered the interdisciplinary area with nanolithography, physics and chemistry. When I started to write these acknowledgements, I found there is numerous people helped me in the past and I will never achieve the success today without them. Therefore, I would like to write some words to thank all for their help in the past.

My deepest appreciation firstly goes to my daily supervisor Dr. Carlen who brought me to BIOS group - a brilliant group. Without your guidance on the scientific direction, it will be a mission impossible to finish my thesis at this level. You are my supervisor and also one of my best friends in the group. I always enjoy the conversation between us about not only science but also the food, life etc. I appreciate very much that you lead me on the right direction for doing research and leave me sufficient freedom to try my own ideas. It is my great pleasure to work with you and make a friend like you.

I would like to address my special thanks to Professor Albert van den Berg. Thank you very much for being my promoter. In my eyes, you are a great scientist and a perfect group leader. I benefit a lot from the meeting with you. Your sharp questions help me better understand what I am doing, your new ideas stimulate my research interests, and your suggestions help me to present my work in a proper way. BIOS workweek is the most fantastic activity I ever experienced in a research group. I tasted multi-disciplinary knowledge with happiness during the workweek. You are the person who could combine the science with happiness. Much fun and happiness in Nijverdal every year (biking, Ping-Pong, BBQ…), these good memories will accompany with me in the future.

I expected a hard time when I start my PhD study. However, there is one person who makes my life easier at the beginning. I would like to express my very special thanks to Hermine. You helped me a lot at very beginning for settling down in Enschede. Without your help, everything could not go so smoothly. In BIOS, we have a powerful technician team who makes everything possible. Daniel, thank you very much for help me at the beginning for EBL and Sputterke. You are not in BIOS now, but you did give me great help at my very beginning days in BIOS. Johan, you know everything in cleanroom since you never say no to me when I need your help for cleanroom work. Thank you for helping me about the cleanroom work and chemical lab work. Another key person to address my thanks to, he is Paul. I never try to image that I could finish all chemical lab work without you. Without you, I may not even have chemicals to measure. Thank you very much. Henk, you are a part time BIOS member but you are an important person for me since you helped to finish the LIL work and made many beautiful photos of my samples. These experiments are very valuable part of my thesis. I hope you can enjoy that part when you read it. Hans, Jan van Nieuwkasteele, and Lennart, thank you for the help for making special sample holders, PDMS mode tools and useful technical discussion for my research.

Séverine, I thank you very much for the help to Lingling and me both in life and science. Your greeting cards are one of our best memories from BIOS group. Jan (Jan Eijkel), I would like to use Lingling's words to express my thanks to you "The extraordinary and multidisciplinary knowledge you posses, together with honest, experience and kindness make you a person with whom work is nothing else but a pleasure". Thank you very much for your questions during my presentation in BIOS group. All of those questions helped me understand more about my research during finding answers. Eddy, you are so kind. Thank you very much for the AFM help and AT organization. I appreciate very much about what you helped me in the

past 4 years. Justyna, thanks for the discussion about SERS and wish you a good success in gas SERS measurement. BIOS soccer team members, Egbert, Kees, Edin and Wabe, it is a great experience to play soccer together, thank you very much for the happy time. Thanks to all BIOSers: Wouter O., Ad, Pavel, Jean-Philippe, Mathieu, Loes, Wouter, Floor, Andries, Zhengxia, Eveline, Yawar, Rerngchai, Allison, Arpita, Henriette, Lonneke, Natalia, Guillaume, Loan, Maarten, Masood, Trieu, Susan, Fleur, Rogier, Adithya, Verena, Floris and Bjorn…, as well.

I would like to give my special thanks to Mark and Rico for making beautiful HR-SEM and HR-TEM images and interesting conversations.

To DIOK, my badminton club, I would like to thank our coach Ron. You are the first and also the best trainer I met. My badminton has been improved a lot with you help. To other DIOK club mates, Niles, Harm, Marten, Martijn, Lisa, Andre…, thank all of you, and the happy time I played in the club will be one of the best memory of Enschede.

To Karin from UT international office and all other friends from different associations on the UT campus, I thank you all for the interesting discussion about the internationalization of UT. Some special thanks to Karin, you help me learn more about how to communicate with people coming from different culture and overcome the culture shock. I will benefit from that experience in the future.

I would like to say thanks to all my Dutch and Chinese friends in the Netherlands, without you my life here will be less fun and less colorful.

特别的感谢：给我的爸爸，妈妈，姐姐，玲玲，沁孝和我在荷兰的朋友们。

爸爸，妈妈，姐姐，对你们的感谢我永远无法用语言表达，行动或许也无以回报你们给我的关爱。我只想对你们说我每取得的任何一次成功都是你们对我关爱的结果。而我每次失败后。总能从你们的关爱中重新站起来。你们给了我信心，勇气和面对挫折的坚强。爸爸是儿子心中做人的榜样，妈妈是儿子背后信心的源泉。姐姐你是我背后永远的支持者，谢谢你们对我永远的关爱。

玲玲，你给我的爱是如此的特别，无人可以替代。在离开爸爸，妈妈，姐姐的日子里不知不觉中我已经将你视作我自己的一半。很难想像在没有你的情况下我将如何完成我的学业和生活，在和你的日子里我明白了携子之手与子偕老。谢谢你带给我的一切。

沁孝，你带给我的快乐和压力都是我自己无法想像到的。而这些快乐和压力的第一个成果就是我博士论文的快速完成。感谢你的到来，为我和玲玲增加了无穷的和未知的欢乐。

在荷兰四年多很难想像没有中国朋友的日子是怎样的。非常感谢在荷兰的这些好朋友们。小钟一家，和你们在一起聚餐，打球，陪优优，秀秀玩耍的快乐日子会让我不时的回想。小钟对打球的激情让我看到当年的自己，感谢你小钟，你是我最好的羽毛球搭档。 李琛一家，无论是我们第一次在球场见面，你请我喝一杯的情景，我和你一起打球的日子，我们在学联工作的过程中，还是我们 一起去捷克的旅行，所有的一切，都让我感到非常开心能在荷兰遇到你这样的朋友。李楠， 刘珺，Enschede 幸福的一对。和你们对生活的交谈，对兴趣的共通，都使我和玲玲的业余生活更加充实。我们多彩的生活来自多彩的你们一点都不为过。谢谢!

彦博 （小弟）， 我们对于学业和生活各个方面的讨论都非常有意思。所有的讨论都让我在各个方面有不同的收获，很高兴在过去的两年里与你同一个办公室。非常感谢你在过去的日子里的各种帮助。
一平，杨晶，拉拉，杨頔，康硕，婵娟，吴海宁，程未，孙超，张扬，张晓，常蓝天，刘欣，动动，胥利先，郑定，吴海铮无论打球还是聊天我们都应为兴趣相投在一起，很开心在荷兰认识你们，感谢你们带给我和玲玲的各种欢乐。

给全荷学生学者联合会的同事们丁宁，陈悦，嘉男，张鹏，谢郦，谢闻，夏萌，熊晖，很高兴能和你们一起为了共同的理想工作。和你们工作的过程所得使我获益匪浅。特别感谢中国驻荷兰大使馆教育处罗平参赞和张晓东老师，以及夏磊老师在我过去学联工作中的帮助。
最后我要感谢我在荷兰所有的中国朋友们，正是你们给我带来的欢乐，让我在荷兰的生活如此多姿多彩！

Publications

Published Journal articles:

1. Jin, M.L.; Pully, V.; Otto, C.; van den Berg, A.; Carlen, E.T. *"High-density periodic arrays of self-aligned subwavelength nanopyramids for surface-enhanced Raman spectroscopy"* Journal of Physical Chemistry C, 2010, 114 (50): 21953-21959.
2. Shui, L.L.; Bomer, J.G.; Jin, M.L.; Carlen, E.T.; van den Berg, A.*"Low-pressure on-chip DNA fragmentation using microfluidics",* Nanotechnology, 2011, 22, 494013-494020.

Manuscripts in preparation:

3. Large-area nanogap-plasmon resonator arrays for plasmonic applications.
4. Nanoline resonator arrays for surface enhanced Raman scattering/spectroscopy.

Conference proceedings:

5. Jin, M.L.; Shui, L.L.; Otto, L.L.; van den Berg, A.; Carlen, E.T. *"A lab-on-a-chip system integrated with subwavelength periodic patterned metal surfaces for SERS-based molecular identification biosensing"* In: Proceedings of the 14th International Conference on Miniaturized Systems for Chemistry and Life Sciences, μTAS 2010, 3-7 Oct 2010, Groningen. pp. 1250-1252. Chemical and Biological Microsystems Society. ISSN 1556-5904 ISBN 978-0-9798064-3-8.
6. Jin, M.L.; Bomer, J.G.; Carlen, E.T.; van den Berg, A. *"Subwavelength nanopyramids for surface enhanced Raman scattering"* In: 21st Micromechanics and Micro systems Europe Workshop, MME 2010, 26-29 Sept 2010, Enschede, The Netherlands. pp. 220-223. Twente University Press. ISBN 978-9081673716.
7. Shui, L.L.; Jin, M.L.; Bomer, J. G.; Carlen, E.T.; van den Berg, A. *"High-throughput On-chip DNA Fragmentation"* In: 21st Micromechanics and Micro systems Europe Workshop, MME 2010, 26-29 Sept 2010, Enschede, The Netherlands. pp. 124-127. Twente University Press. ISBN 978-9081673716.
8. Jin, M.L.; Pully, V.; Otto, C.; van den Berg, A.; Carlen, E.T. *"High-Density Periodic Arrays of Subwavelength Nanopyramids for Surface Enhanced Raman Scattering"*, AIP Conf. Proc. 2010 1267, pp. 960-961 XXII INTERNATIONAL CONFERENCE ON RAMAN SPECTROSCOPY; doi:10.1063/1.3482914.